

https://dspace.org/

Incipient motion of boulders in open channel flow

Stols, Kevin

2018

https://hdl.handle.net/10539/25739

Stols, Kevin (2018) Incipient motion of boulders in open channel flow, University of the Witwatersrand, Johannesburg, https://hdl.handle.net/10539/25739

Downloaded from a DSpace repository. https://dspace.org/

INCIPIENT MOTION OF BOULDERS IN OPEN CHANNEL FLOW

Kevin Stols

A research report submitted to the Faculty of Engineering and the Built Environment, University of the Witwatersrand, Johannesburg, in partial fulfilment of the requirements for the degree of Master of Science in Engineering.

Johannesburg, 2018

DECLARATION

I declare that this research report is my own unaided work. It is being submitted to the Degree of Master of Science to the University of the Witwatersrand, Johannesburg. It has not been submitted before for any degree or examination to any other University.

……

……day of.....year……

ABSTRACT

The use of boulders to create habitat heterogeneity is important for aquatic diversity, and being able to predict the stability of a boulder that is placed in a river will aid in sizing the boulder. Identifying ways to increase the stability could save costs associated with over design or replacement due to the boulder washing away. Existing research on incipient motion centres on determining threshold conditions for bed material or protruding elements within a bed surface with relation to, among others: shape of particle, size of particle, relative depth of particle to flow depth, and impact of channel slope. The existing research is limited to bed material that is of a similar size and there is no research on the conditions for incipient motion elements that are relatively large compared to the bed material it is resting on. An idealised flume study was performed to identify trends that several factors have on boulder stability, as well as to verify the results obtained from a pivoting analysis model prediction for a spherical boulder. An additional study was performed to obtain drag coefficients that were suitable for use on spherical boulders that were either embedded into the bed material or simply resting on top of the bed material. The results of the drag experiments were varied; only the results for the non-embedded were suitable to integrate into the model predictions while drag coefficients for the embedded boulders need to be taken from previously published results. The results of the flume study provided good confirmation of the model predictions with the average absolute experimental error being 4%. The trends identified in the flume study show that the most effective method in improving a boulder's stability is to embed it into the bed material with this being more effective than increasing the size of the boulder.

ACKNOWLEDGMENTS

I would like to thank Professor James for the incredible patience he has afforded me in the completion of this research report.

I would also like to thank Mr Wayne Costopoulos and his Laboratory Technician Steven for their assistance in preparing the flumes for use.

CONTENTS

Declaration i

Abstract ii

Acknowledgments iii

Contents iv

List of Figures viii

List of Tables xi

List of Symbols xii

1 Introduction 1

1.1 Research Objectives 4

2 Review of Literature 6

2.1 Practical Use of Boulders 6

2.2 Flow Resistance 7

2.3 Incipient Motion 9

2.3.1 Earliest work 9

2.3.2 Shields 9

2.3.3 Shape 11

2.3.4 Size Effect 12

2.3.5 Relative Depth 14

2.3.6 Slope 14

2.3.7 Effect of Relative Protrusion 15

2.3.8 Theoretical Approach- Pivoting Analysis 16

2.3.9 Drag Coefficient 19

2.3.10 Lift Force 21

2.3.11 Velocity vs Shear 22

2.4 Data Scatter 23
3 Experimental Investigation 25
3.1 Introduction 25
3.2 Boulder Incipient Motion Experiments 27
3.2.1 Apparatus 27
3.2.2 Flume and boulder setup 27
3.2.3 Test conditions 31
3.2.4 Research methodology 33
3.3 Drag Coefficient Calibration Experiments 36
3.3.1 Apparatus 36
3.3.2 Flume and boulder setup 36
3.3.3 Test conditions 40
3.3.4 Research methodology 42
3.3.4.1 Flow Measurement 42
3.3.4.2 Force Measurement 43
3.3.5 Calculating the Drag Coefficient 47
4 Model Analysis 48
4.1 Introduction 48
4.2 Developing the Model 48
4.2.1 Basis of model 48
4.2.2 Geometry of the model 49
4.2.3 Submerged Weight of Boulder 52
4.2.4 Drag and Lift Forces 53
4.2.5 Moment Lever Arm 55
4.2.6 Subject of Manipulation 57

4.2.7 Dimensionless Velocity Equation 58
4.3 Determining the Flow Depth and Appropriate Flow Velocity 59
5 Results 61
5.1 Drag Coefficient Calibration 61
5.1.1.1 Results 61
5.1.1.2 Discussion 62
5.1.1.3 Conclusion 64
5.2 Boulder Incipient Motion Experiments 65
5.2.1 Effect of Relative Size 65
5.2.1.1 Note on Boulder Density 65
5.2.1.2 Results 67
5.2.1.3 Discussion 68
5.2.1.4 Conclusion 70
5.2.2 Effect of Slope 71
5.2.2.1 Results 71
5.2.2.2 Discussion 73
5.2.2.3 Conclusion 76
5.2.3 Effect of Relative Density 77
5.2.3.1 Results 77
5.2.3.2 Discussion 78
5.2.3.3 Conclusion 80
5.2.4 Effect of Embedding 81
5.2.4.1 Results 81
5.2.4.2 Discussion 82
5.2.4.3 Conclusion 85

5.3 Application of Model 86
5.3.1 Moment Equilibrium- Equation 4-1 86
5.3.2 Critical Dimensionless Velocity – Equation 4-32 88
6 Conclusions and Recommendations 91
6.1 Drag Calibration Experiments 91
6.2 Boulder Incipient Motion Experiments 91
6.3 Model Analysis 92
6.4 Recommendations for Further Research 92
7 References 94

LIST OF FIGURES

Figure 2-1: (a) Typical cross section of rock chute with protruding boulders and (b) criteria used for water depth measurements (Pagliara and Chiavaccini 2006). 9

Figure 2-2: Shields Diagram for Incipient Motion (Vanoni 1975). 11

Figure 2-3: Parameters related to condition of incipient motion (symbols changed from Gögüs and Defne 2005). 12

Figure 2-4: Shape Factor Correction for τ_* versus d_* for different slopes (Gögüs and Defne 2005). 13

Figure 2-5: Shields stress as a function of R_b/d for different grain sizes (where R_b is the Hydraulic radius) (Shvidchenko and Pender 2000). 14

Figure 2-6: Shields stress as a function of slope corresponding to a $q_{s*} = 10^{-4}$ (Shvidchenko and Pender 2000). 15

Figure 2-7: Forces acting on a particle (James 1990). 16

Figure 2-8: Pivoting Geometry (James 1990). 19

Figure 2-9: Relationship for relative submergence and drag coefficient for hemispheres. (Flammer et al, 1970). 20

Figure 3-1: Tilting flume in the School of Civil and Environmental Engineering Hydraulics Laboratory. 25

Figure 3-2: Zero-slope flume in the School of Civil and Environmental Engineering Hydraulics Laboratory (Jackson 2016). 26

Figure 3-3: Section of Flume C with clear Perspex and measuring tape for measuring flow depths. 28

Figure 3-4: Flume C lined with bricks and pebbles to create artificially raised bed. 29

Figure 3-5: Lego brick used to alter the depth of the boulder; Triangular base of 3 spheres for boulders to rest on. 30

Figure 3-6: Schematic of boulder setup with hatched spheres representing the pivot spheres (a: no embedding, b: embedded a distance E). 31

Figure 3-7: Lego configuration for boulder being embedded. 35

Figure 3-8: Apparatus for drag coefficient experiments. 37

Figure 3-9: Schematic of set up taken from Jackson (2016). 38

Figure 3-10: Schematic of rod fixed to load cell where $F_t/4$ is the force acting through the plate. Dashed lines indicate plate in rest position and solid lines represent plate after a force is applied. 39

Figure 3-11: Screenshot of software used to record force measurements. 46

Figure 4-1: Forces acting on a particle (James 1990). 48

Figure 4-2: Pivoting geometry on bed material slope $\alpha=0°$. 50

Figure 4-3: Schematic of boulder position for volume and area calculations..... 52

Figure 4-4: Relationship for relative submergence and drag coefficient for hemispheres (Flammer et al. 1970). 54

Figure 4-5: Moment lever arms a, b and c, about the pivot point. 56

Figure 5-1: Relationship between relative flow depth and drag coefficient. 62

Figure 5-2: Reynolds Number versus Drag Coefficient. 63

Figure 5-3: Comparison of predicted dimensionless velocity using experimental drag coefficients and drag coefficients taken from Flammer et al. (1970). 64

Figure 5-4:Relationship between relative size and critical average velocity. 68

Figure 5-5: Relationship between relative size and critical dimensionless velocity. 69

Figure 5-6: Relationship between relative boulder size and relative flow depth at incipient movement. 70

Figure 5-7: Relationship between slope and critical dimensionless velocity. 73

Figure 5-8: Relationship between slope and critical Shields parameter. 75

Figure 5-9: Relationship between slope and relative flow depth at incipient movement. 75

Figure 5-10: Relationship between relative density and critical average velocity.79

Figure 5-11: Relationship between relative density and critical dimensionless velocity. 79

Figure 5-12: Relationship between relative embedment and critical dimensionless velocity. 82

Figure 5-13: Relationship between relative embedment and critical average velocity. 83

Figure 5-14: Relationship between relative embedment and relative flow depth at incipient movement. 85

Figure 5-15: Relationship between stabilizing and destabilizing moments based on Equation (4-1) for boulder incipient motion experiments..... 86

Figure 5-16: Comparison of experimental and predicted dimensionless velocities based on Equation 4-32. 88

LIST OF TABLES

Table 3-1: Experimental conditions with comparison to a control experiment for each incipient motion experiment. 32

Table 3-2: Experimental conditions with comparison to a control condition for each drag coefficient experiment. 42

Table 5-1: Results of Drag Coefficient Experiments. 61

Table 5-2: Boulder Densities. 66

Table 5-3: Experimental and predicted results for relative size experiments. 67

Table 5-4: Experimental and predicted results for slope experiments. 71

Table 5-5: Experimental and predicted results for relative density experiments.. 77

Table 5-6: Experimental and predicted results for embedding experiments..... 81

Table 5-7: Experimental and predicted results for all boulders that pivoted out of position. 89

LIST OF SYMBOLS

$\forall$	Represents a particle's relative volume with respect to a rectangular prism containing it
A	Height of the particle/boulder centroid above the theoretical bed
a	Perpendicular distance of particle/boulder centroid from pivot axis
a'	Perpendicular distance between boulder and bed particle centroid in flow direction
A_E	Area of boulder embedded below top of bed particles
A_n	Area of particle/boulder exposed normal to flow
A_p	Area of particle/boulder exposed perpendicular to flow
A_s	Area of a boulder segment not subject to flow
B	Distance of the theoretical bed below the top of the bed particles
b	Lever arm of drag force
c	Lever arm of lift force
C_D	Drag coefficient
CF	Tension sensor calibration factor
C_L	Lift coefficient
D	Diameter of a boulder
d	Diameter of a sediment
d_*	Dimensionless grain size
d_{50}	Grain size for which 50% of the grains are finer
d_i	Grain size for which i% of the grains are finer
d_n	Nominal diameter of sediment particle based on volume
E	Depth of embedment
F	Net hydrodynamic force on article/boulder
F_D	Drag force
F_L	Lift force
F_r	Frictional forces between particles
F_t	Force recorded on tension sensor
g	Gravitational acceleration
h	Height of boulder segment not exposed to flow
i	Slope
K	Characteristic dimension of supporting particles/bed material
k_1	Proportionality constant for particle volume
k_2	Proportionality constant for particle weight lever arm
k_3	Proportionality constant for drag force lever arm
k_4	Proportionality constant for lift force lever arm
k_5	Proportion of normally projected area exposed
k_6	Proportionality constant for normally projected area
k_7	Proportion of parallel projected area exposed
k_8	Proportionality constant for parallel projected area

k_9	Proportionality constant for velocity position
k_{10}	Multiple of bed particle size for grain roughness
L_1	Maximum width of grain perpendicular to flow direction and parallel to channel bottom
L_2	height of grain resting on channel bed
L_3	maximum length of grain in flow direction parallel to channel bottom;
n	Manning's roughness coefficient
P	Protrusion of entrained particle
q_{s*}	Einstein bed load parameter
Q	Flow rate
r	Radius of boulder
R	Reaction forces between particles
R_b	Hydraulic Radius
Re	Reynolds Number
$Re*$	Shear Reynolds number
S_0	Flume slope
s_E	Length of embedded segment chord
SF	Shape factor
s_s	Length of unsubmerged segment chord
Ss	Particle/boulder relative density
u_*	Shear or friction velocity
u_{*c}	Shear velocity at incipient motion
V	Average velocity
V_{disp}	Volume of water displaced
W	Submerged weight of particle/boulder
w	Width of flume
x	Einstein velocity profile correction factor
y	Flow depth above bed particles
α	Longitudinal angle of bed
β	Angle subtended by particle centroid and theoretical bed
γ	Specific weight of the fluid
γ_s	Specific weight of the sediment/boulder
Θ_E	Angle subtended by lines passing boulder centroid and embedded segment chord
Θ_s	Angle subtended by lines passing boulder centroid and unsubmerged segment chord
λ	Proportionality constant for the spacing of the supporting bed particles
μ	Proportionality constant for the particle centroid elevation above the bed material centroid
ν	Kinematic fluid viscosity
ρ	Fluid density
ρ_s	Particle/boulder density
ρ_w	Density of water

τ_* Shields shear stress

τ_* Entrainment function as per Gogus and Defne (2005)

τ_{*c} Critical shield stress

τ_{*c50} Critical Shields dimensionless shear stress for size d_{50}

τ_{*ci} Critical Shields dimensionless shear stress for size d_i

τ_o Critical shear stress

ϕ Pivot angle

1 INTRODUCTION

Throughout human history, the value of water is evident. The proximity of almost every major city in the world to a potable water supply serves as an obvious indication of this, and rivers have been a vital component to this. Apart from being the obvious source of hydration for humans and animals, rivers provide multiple services to society.

Rivers serve as a source of irrigation for crop generation, they act as transport networks, and they can have a recreational function. They feed our reservoirs and dams for purposes such as power generation, water supply, and recreation. They also serve as drainage channels during heavy rains to mitigate against potential flooding. With these benefits, there is often an associated economic and social value applied to rivers.

Unfortunately, because of this, the environmental value of rivers has often been over-looked. In most cases our activities impact the dynamic equilibrium of stream systems and sadly it is often in a negative way. The way the earth's population has exponentially grown in the last century has placed significant strain on the environment and specifically the demand for water has tested rivers' ability to perform functions in the same manner as if we were not imposing on them.

Environmental Impact Assessments have become a vital tool in determining the impact that intended activities could have on an ecosystem. They provide information as to what potential there is for damage and as such can provide insight about what can be done to limit, as much as is possible, the impact of such damage. Unfortunately, river systems are often not considered as a whole for various reasons. The size, complexity, and detail of the system requires too much time to understand and the specialists required to analyse the systems may be unavailable or simply be too expensive (Bernard and Tuttle 1998).

Dermisis and Papanicolaou (2008) suggest that the degradation of rivers due to human activities often results in straighter channels that are characterised by increased flow velocities which increases the potential for bed degradation. Bed degradation can lead to channels becoming highly incised which increases the risk of the banks failing. Both bank failure and bed degradation lead to increased sediment transportation in the flow. The result of this is a need for river rehabilitation, restoration, and/or protection.

Bernard and Tuttle (1998) state that proper restoration plans require more effort than simply protecting the banks of a channel. The larger ecosystem/watershed needs to be viewed because the stream and its characteristics are inseparable from the watershed drainage characteristics. The biological functions of a system are also closely linked to the ecosystem and any changes to a stream environment will influence the biodiversity and biological functions of that ecosystem.

In much of the literature, habitat heterogeneity seems to be accepted as an important feature that positively influences biodiversity, however the specific design considerations/parameters and assessment tools are lacking (Wheaton and Pasternack 2004). Despite the notion of habitat heterogeneity being engrained in the habitat restoration community (Pretty, et al. 2003), the lack of assessment tools means that achieving it in practice remains ambiguous.

Aquatic life is something that is greatly affected by the hydraulic characteristics of a river. The bed morphology and aquatic environment can be affected by the flow while oxygen content and potential food supply for aquatic life could be influenced as well. Having flow obstructions, such as boulders, could create important microhabitats for biota (Hamuy-Blanco 2013).

The importance of structural cover for aquatic fauna is established by Pretty et al. (2003). Merz (2001) and Hendry et al. (2003) describe the benefits to salmonids as, among others, protection from predation, resting, primary production, and water temperature regulation.

Boulders in rivers and river rehabilitation provide structural cover for aquatic fauna and create flow obstructions necessary to enhance habitat heterogeneity. The objective of this research is to gain a better understanding of the stability of boulders in rivers so that sound, economic engineering decisions can be made when designing river channels that require boulders as a cost-effective solution.

Vanoni (1966) suggested that the determination of threshold conditions for sediment motion is simplified if the sediment motion is viewed as a balance of the resisting forces of a resting particle and the forces of the fluid flowing over the particle. Helley (1969) deduced that this would be particularly true if the bed material were coarse because the physical properties can be measured more accurately than finer sized particles.

There have been several studies that research the effect that boulders have on improving the heterogeneity of the ecosystems as well as studies to determine the effect that the boulders have on the resistance to flow (Thorne and Zevenbergen 1985, Pagliara and Chiavaccini 2006, Dermisis and Papanicolaou 2008). While incipient motion and particle entrainment of bed material has been extensively studied (Shields 1936, Fenton and Abbott 1977, Shvidchenko and Pender 2000, Shvidchenko et al. 2001, Gögüs and Defne 2005), there are gaps in knowledge as far as boulders are concerned.

The majority of incipient motion studies involve determining the threshold conditions for bed material or protruding elements within the bed surface. There have been empirical approaches and variations as well as theoretical analyses. The studies have investigated the effects of, among others: shape of particle, size of particle, relative depth of particle to flow depth, and impact of channel slope. While the impact of size of particle on incipient motion has been researched, this has been limited to investigating bed material particle size variations.

There is no research on the conditions for incipient motion of relatively large elements (e.g. boulders) placed on smaller bed particles. Carling et al. (2002b) researched the incipient motion of rectangular blocks but this was on a bedrock

base and sliding was the main criterion for motion. There is research as to the effect of protrusion of a particle, but this is for particles of a similar size to the bed material. Conversely there is no research as to the extent that level of embedding would have on improving the stability of larger elements. Large elements (such as boulders) would logically have a significant fraction of their area exposed to the flow that would cause instability and thus embedding could potentially serve as a simple stability enhancement.

Embedding a boulder to improve its stability is not only achieved by artificial means. Natural embedding could occur if a boulder were resting on finer bed material and the finer material moved as a result of vortices around the boulder (similar to scour around piers). A scour hole could form downstream of the boulder and the boulder itself could move into the hole and thus embed itself.

The instability of a boulder exposed to flow is caused by the forces associated with water flowing around an object, namely drag and lift forces. Drag coefficients have been determined for blocks exposed to flow on bedrock material and they have also been determined for hemispheres exposed to free surface effects. There is no clear research on the drag coefficients for spherical boulders exposed to emergent conditions while also being embedded into the bed material.

1.1 Research Objectives

The aim of this research was to develop a tool for predicting whether or not a spherical boulder would be stable for a given set of flow conditions and correlating this with empirical data obtained through flume experiments.

Drag coefficients required for developing the model would be calibrated by measuring the drag forces on the boulders using special load cell apparatus.

The stability model can then be implemented in the design of channels that make use of boulders.

The scope of the research was limited to testing boulders under uniform flow conditions on an idealized coarse bed material where the bed material will not be entrained before a boulder is dislodged. Although the relative size of the boulders was a design consideration, the variation in the size came from the boulder being tested as changing the bed material would prove to be too costly, both financially and time wise.

2 REVIEW OF LITERATURE

There is an important distinction to make between river restoration and river rehabilitation. River restoration is the action of returning a river to its natural state as if there were no artificial development whereas river rehabilitation only aims to repair and recover ecosystem services lost as a result of development. The difficulty in attempting river restoration is determining the exact historic or natural conditions a river and even if those conditions are determined, it is not always physically possible to restore said conditions (Hamuy-Blanco 2013). As such, river rehabilitation is an acceptable approach.

Rehabilitation can either be active or passive. Active rehabilitation involves physically installing features or measures to repair damage already accrued, while passive rehabilitation could involve the removal of activities or features that degrade the river, either physically or by a degradation of the ecosystem (Bernard and Tuttle 1998).

2.1 Practical Use of Boulders

A common technique used in improving degraded aquatic habitats and waterways is the use of rocks or boulders. It is known that flow around a boulder results in a flow separation which creates vortices in the wake region of the boulder. There is also an increased variability in depth of flow and flow velocity which is beneficial to habitat diversity. In the wake region, sunlight is diffused which creates overhead cover for fish (Dermisis and Papanicolaou 2008). The scour created by the vortices creates habitat used by both juvenile and adult fish (Fischenich and Seal 1999).

Specific placement of boulders can modify the hydraulic resistance of a channel by changing the channel geometry. This can have a stabilizing effect on the channel as a whole (Pagliara and Chiavaccini 2006).

Dermisis and Papanicolaou (2008) studied the effect that clasts (rocks or boulders) have on sand movement over gravel beds for low relative submergence conditions and found that sand ridges were formed upstream of the clast array while small depositional sand patches formed in the “stoss” region of individual clasts. The sand ridge had implications on the amount of sand entering the array region and thus the impact of the clast array was a reduced exiting bedload rate. This has a beneficial aspect for fish abundance as it is known that gravel substrates are used by fish to deposit their eggs in, forming so-called “spawning gravels” or “redds”, and a limitation of sand entering a clast array preserves the habitat for the fish (Dermisis and Papanicolaou 2008).

2.2 Flow Resistance

There are several important distinctions between mountain rivers and lowland rivers. The slopes of mountain rivers are generally 1-5% steeper than lowland rivers, the bed material comprises cobbles and boulders rather than sand and gravel, and relative roughness is larger with boulders often protruding through the free surface (Thorne and Zevenbergen 1985). Free surface distortions, form drag of boulders, and hydraulic jumps associated with locally accelerated flow all contribute significantly to flow resistance, and all are more likely to be evident in mountain rivers, thus, flow resistance equations for lowland rivers don’t explicitly account for them.

Flow resistance, as referred to above, is an indication of how the shape and bed roughness of a channel control the depth, width, and mean velocity of the flow in the channel. These aspects are typically accounted for by a flow resistance coefficient, being used in conjunction with a flow velocity equation, with the most common of these being one of Manning or Chézy coefficient, or the Darcy-Weisbach friction factor.

The use of these coefficients in flow resistance formulae needs to be done with the understanding of the principles and assumptions used to develop them. As stated

above, the presence of boulders would affect the determination of these coefficients.

Research by Thorne and Zevenbergen (1985) found that, based on the results of a flume study, the shape of a boulder is not an important parameter in the determination of resistance for calculating the mean velocity in mountain rivers, while Pagliara and Chiavaccini (2006) have stated that simply the presence of boulders on a rock chute will increase flow resistance (this is not to be confused with shape being an important parameter in the stability of the boulder itself). Pagliara and Chiavaccini (2006) stated that the concentration of boulders, the boulder roughness, and the slope of the ramp affect the degree of resistance where increases in flow resistance are directly proportional to the concentration of boulders. Dermisis and Papanicolaou (2008) found that in the presence of clasts, the resistance of a gravel bed increased as much as 6 times, which they attribute to added form roughness.

A schematic of the chute that Pagliara and Chiavaccini (2006) used for their experiments is shown in Figure 2-1. They conducted tests for slopes up to 0.4 and relative submergence of up to 8, but identified that they could only achieve such values by anchoring their rocks as loose rocks were unstable under the desired flow conditions. While their experiment was concerned with flow resistance and not boulder stability, identifying the stability of a boulder is necessary if the boulder is needed in order to maintain certain flow conditions.

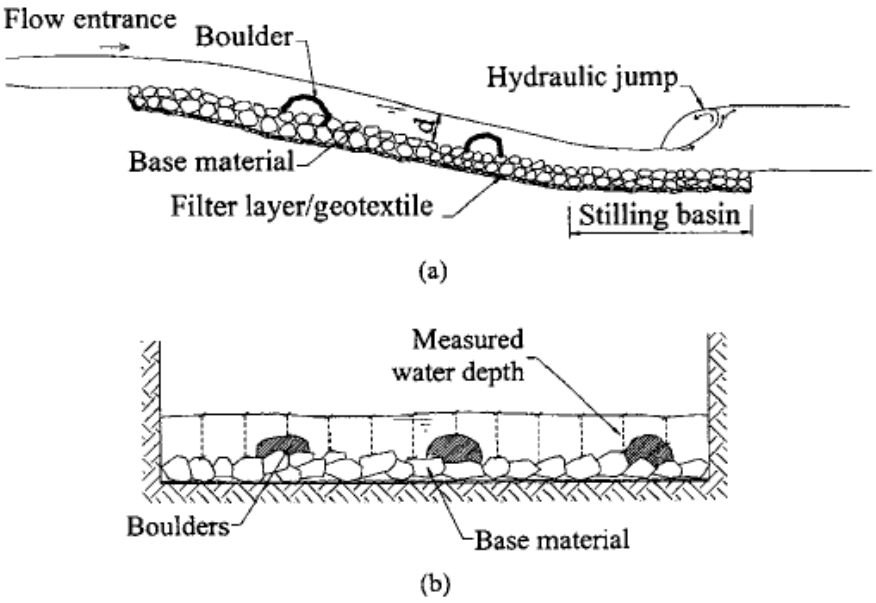


Figure 2-1: (a) Typical cross section of rock chute with protruding boulders and (b) criteria used for water depth measurements (Pagliara and Chiavaccini 2006).

2.3 Incipient Motion

2.3.1 Earliest work

Hoffmans (2010) summarized that Brahms (1767) introduced one the earliest known stability equations for incipient motion of loose materials. Being a hydraulic engineer and superintendent of dikes, Brahms proposed that, at the point of incipient motion, the weight of a bed particle is proportional to the sixth power of the flow velocity. Hjulström (1935) confirmed Brahms' results with respect to flow velocities and size of particles for loose materials and extended Brahms' diagram to include cohesive sediments

2.3.2 Shields

A major contributor to the work of incipient motion has been Shields (1936). Shields is credited as being the first person to express the critical shear stress for initiation of sediment motion in a dimensionless form (Ling 1995):

$$\frac{\tau_0}{(\gamma_s - \gamma)d} = F(\frac{u_* d}{\nu}) \quad (2\text{-}1)$$

in which τ_o = critical shear stress; γ_s = specific weight of the sediment; γ = specific weight of the fluid; d = diameter of the sediment; u_* = shear or friction velocity, being equal to sqrt(τ_o / ρ), where ρ = density of the fluid; ν = kinematic viscosity; and F = some function (Ling 1995). The first term is often referred to as the Shields parameter while the second term is referred to as the shear Reynolds number (Re_*). The shear Reynolds number refers to the degree to which the grains project through the viscous sublayer (James 2015). The Shields number is a ratio of the shear stress to the submerged weight, per unit area of bed, per layer of grains and thus it is a ratio of disturbing to stabilizing forces on a bed of particles (James 2015).

Shields took empirical data to create a threshold and plotted what is known as Shields Diagram (Figure 2-2) which is one of the most widely used curves when working with incipient motion. If a combination of flow and sediment characteristics, represented by Equation 2-1, plots below the curve, then no movement of sediment is expected.

Over the years there have been numerous studies that are aimed at furthering the knowledge of incipient motion and expanding Shields's work to overcome some of the limitations of his work.

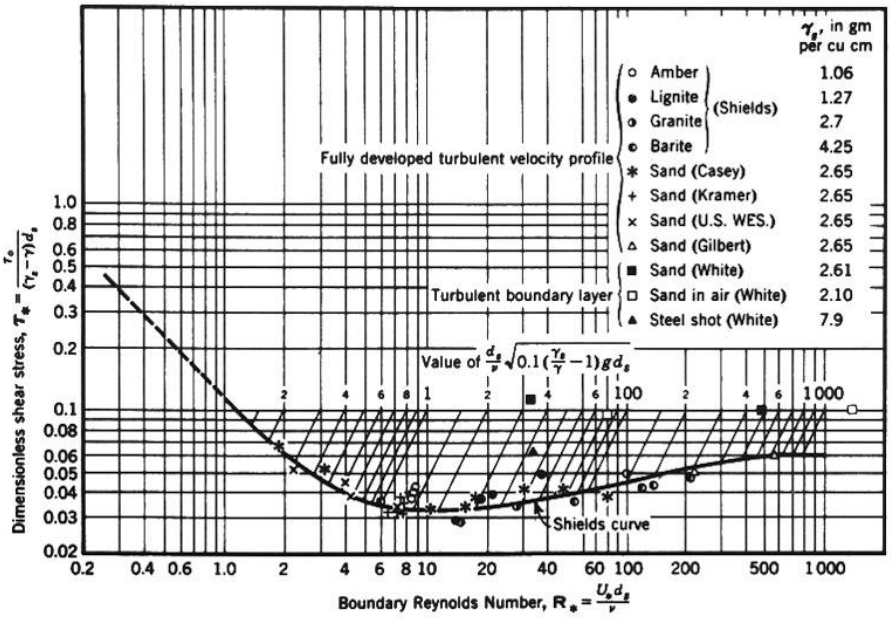


Figure 2-2: Shields Diagram for Incipient Motion (Vanoni 1975).

2.3.3 Shape

Gögüs and Defne (2005) studied the threshold motion of single particles under subcritical, uniform flow and suggested that the shape of a particle has a significant effect on its incipient motion. They suggest the inclusion of a dimensionless shape factor in incipient motion analysis

$$SF = f\left(\frac{L_1 + L_2}{2L_3}, \frac{\forall}{L_1 L_2 L_3}\right) \tag{2-2}$$

where L_1 is the maximum width of a grain perpendicular to flow and parallel to the channel bed, L_2 is the height of a grain resting on a channel bed, and L_3 is the maximum length of grain in flow direction and parallel to channel bed, as shown in Figure 2-3. $\forall$ represents a particle's relative volume with respect to a rectangular prism containing it. The inclusion of the second term means that cubic particles will have different shape factors compared to spherical ones that have a diameter equal to the cube's characteristic length.

Hoffmans (2010) commented that the geometry of the particle was also important as angular particles are less likely to roll than spherical ones.

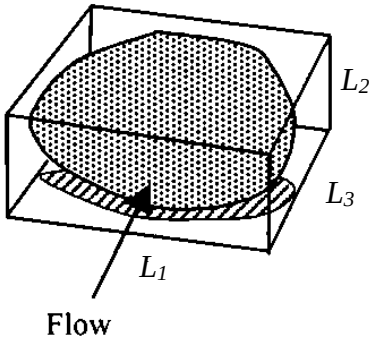


Figure 2-3: Parameters related to condition of incipient motion (symbols changed from Gögüs and Defne 2005).

2.3.4 Size Effect

Shvidchenko and Pender (2000) showed that critical flow conditions for uniform sediment motion are dependent not only on the grain size but also on the ratio of flow depth to grain diameter.

Shvidchenko et al. (2001) noted that it is generally accepted that in sediment mixtures, smaller particles are shielded by coarser grains and need a higher shear stress for mobilization compared with uniform sediment of the same size. Conversely, larger particles in mixtures are entrained at lower shear stress than in a bed of uniform sediment because of increased exposure and instability. They demonstrated that the relative variation of the critical value of Shields parameter for different grain sizes d_i within a mixture is largely controlled by their relative size with respect to a central value of the grain-size distribution, commonly the median sized d_{50}: (Shvidchenko et al. 2001)

$$\frac{\tau_{ci}^*}{\tau_{c50}^*} = f(\frac{d_i}{d_{50}}) \qquad (2\text{-}3)$$

where τ^*_{ci} and τ^*_{c50} are critical values of the Shields dimensionless shear stress for particle sizes d_i and d_{50}, respectively.

Gögüs and Defne (2005) obtained similar findings to Shvidchenko and Pender (2000) but related the critical entrainment function (τ_*), for a given particle size and bed slope, to the shape as well, which can be determined directly from Figure 2-4. The trends tend to decrease with increasing dimensionless grain size (d_*) given by:

$$d_* = d_n \left(\frac{\frac{(\rho_s - \rho)}{\rho} \cdot g}{\nu^2} \right)^{1/3} \qquad (2\text{-}4)$$

where d_n is nominal diameter of a sediment particle based on its volume. The shape factor (SF) described in Figure 2-4 is the same as represented by Equation 2-2.

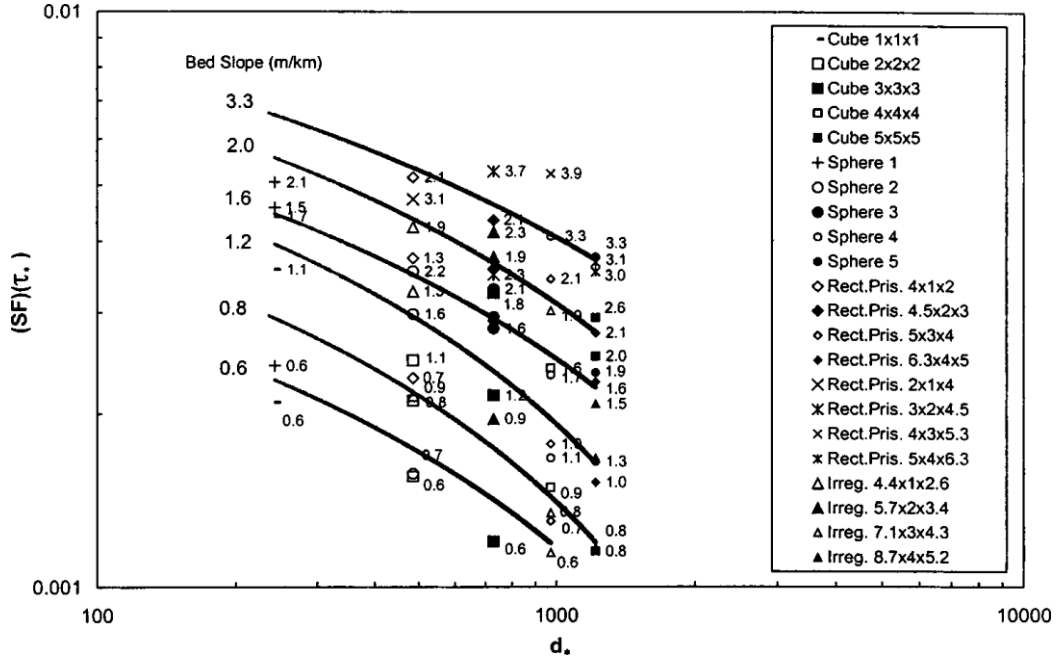


Figure 2-4: Shape Factor Correction for τ_* versus d_* for different slopes (Gögüs and Defne 2005).

2.3.5 Relative Depth

Shvidchenko and Pender (2000) also analysed the effect that relative depth (ratio of water depth to grain size R_b/d) has on incipient motion for coarse uniform sediments. The data revealed that, for their definition of incipient motion, the lower the relative depth for steeper slopes the higher the value of critical shear stress for a given grain size (see Figure 2-5). Incipient motion in this case refers to a threshold sediment transport rate related to the Einstein bed load parameter, q_{s*}, for the sediment under consideration.

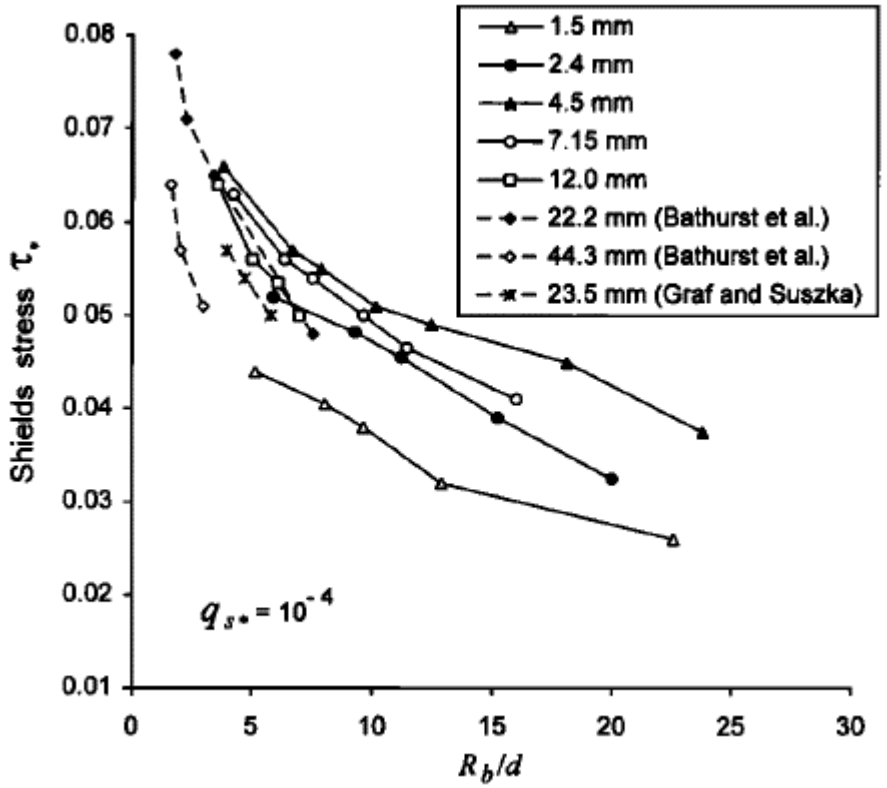


Figure 2-5: Shields stress as a function of R_b/d for different grain sizes (where R_b is the Hydraulic radius) (Shvidchenko and Pender 2000).

2.3.6 Slope

Motamedi et al. (2010) reviewed Shvidchenko and Pender (2000) and summarized that critical Shields stress for sediment motion depends not only on the sediment size, but also on the bed slope. Shvidchenko and Pender (2000) also showed in their experimental study that τ^*_c is not constant for rough turbulent flow, as it is usually assumed.

There is greater resistance of grains in steeper, shallower flows due to the increased effect of relative flow depth. As a result, the steeper the slope, the higher is the value of τ^*_c for a given grain size (Shvidchenko et al. 2001).

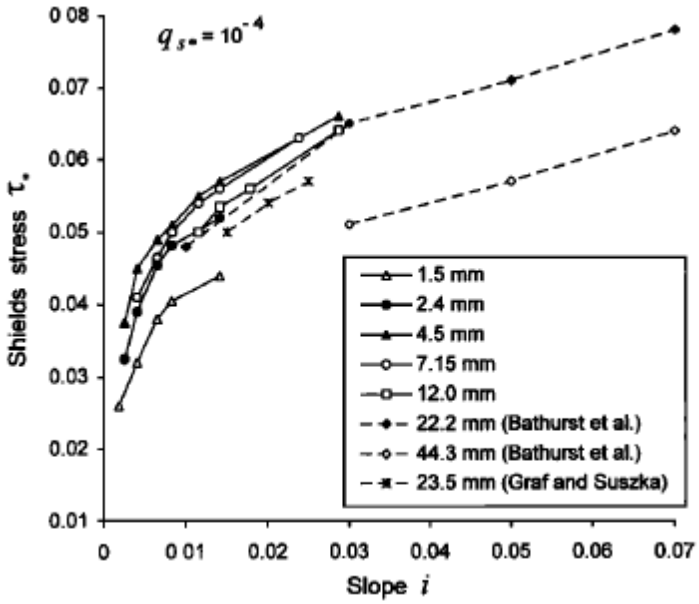


Figure 2-6: Shields stress as a function of slope corresponding to a $q_{s*} = 10^{-4}$ (Shvidchenko and Pender 2000).

2.3.7 Effect of Relative Protrusion

In channels and sediment beds, the grain size distribution is not uniform and thus beds can never be planar. As a result, most particles in motion are likely to move as over-riding particles and hence, the conventional Shields curve is not applicable for such cases because the over-riding particle will offer far less resistance compared to particles below the bed level. The Shields parameter would be lower for over-riding particles because of the particle's direct exposure to the main flow (Rao 2004).

Fenton and Abbott (1977) researched what impact a higher protrusion than the rest of a stream bed would have on the stability of a grain. They postulated that the grain would be subjected to more of the fluid flow and thus would experience greater disturbing forces while resisting forces are less. Difficulty was

encountered in protruding several grains and thus they resorted to testing a single grain at a given test position. They concluded that their sampling technique was deficient, but it did allow them to obtain consistent results which did highlight the effect of protrusion

2.3.8 Theoretical Approach- Pivoting Analysis

In a stream bed with turbulent flow, every grain experiences fluctuating instantaneous lift and drag forces. Entrainment of a single grain occurs when the local instantaneous destabilizing forces exceed the forces acting to stabilize it (Shvidchenko and Pender 2000). As with any analysis of motion, the forces acting on the elements in motion can be analyzed. James (1990) presented a general model for predicting entrainment conditions for non-uniform, non-cohesive sediments.

His model is based on an analysis of the moments of forces acting on a particle at the condition of incipient motion. Particle geometry and packing arrangement are accounted for as well as variations of near bed flow velocity and drag and lift coefficients for a wide range of flow conditions.

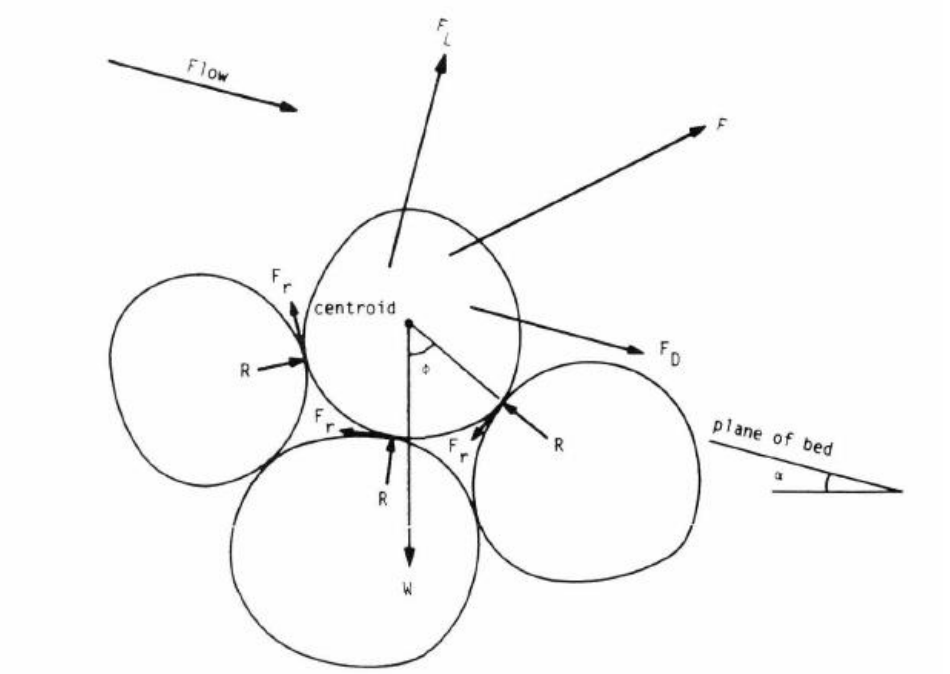


Figure 2-7: Forces acting on a particle (James 1990).

A general entrainment model must be based on consideration of the forces acting on a particle that rests on a bed angle α. These forces are illustrated in Figure 2-7 and include a) the submerged weight of the particle (W) acting at an angle ϕ to the pivot point, b) reaction forces (R), c) friction forces (F_r) at points of contact with adjacent particles, and (d) a net hydrodynamic force (F). At the condition of incipient motion, the reaction and friction forces through all but one or two contact points will reduce to zero and the particle will move by either sliding or pivoting over the remaining contact point/s.

When considering the stability of a particle the net hydrodynamic force may be specified in terms of magnitude and direction or in terms of the drag (F_D) and lift (F_L) components (as in most other analyses). In many other cases, the analysis has been simplified by assuming one or other of these components to be negligibly small.

James (1990) states that the occurrence of drag is now generally accepted but the importance of lift is not fully appreciated. He found that one of the earliest investigations of lift was by Jeffreys (1929), who used ideal flow theory to quantify lift forces on bed particles. Subsequent experimental work has shown lift force to be strongly dependent on particle Reynolds number ($Re^* = u_* D/\nu$), where u_*, is the shear velocity, D the particle size and ν the fluid kinematic viscosity.

In the following model, James (1990) presents an extension of previous pivoting analysis models but makes fewer initial assumptions for a more general formula.

Pivoting analysis:

The forces acting on a bed particle are identified in Figure 2-7. The basis for this analysis is the assumption that initial movement will be rolling rather than sliding. Li and Komar (1986) suggest that rolling is the more frequent mode of incipient movement for spherical particles and that the flow conditions for incipient motion by sliding are similar to the conditions for rolling.

The analysis by James (1990) resulted in Equation 2-5 which is presented such that it can be compared with Shields parameter:

$$\frac{u_{*c}^2}{gD(S_s-1)} = \frac{k_1 k_2 \sin(\phi-\alpha)}{16.531 \log_{10}^2(30.2 k_9 Dx/k_{10}K)(C_D k_5 k_6(k_2 \cos\phi + k_3) + C_L k_7 k_8(k_2 \sin\phi + k_4))} \quad (2\text{-}5)$$

in which S_s is the relative density, and u_{*c} is the shear velocity at incipient motion. D and K represent the particle and bed material sizes respectively, as shown in Figure 2-8. The variables k_1 through k_9 represent various proportionality constants specific to the shape of the particle being analysed and the variable k_{10} represents a multiple for roughness of the bed material.

Because of the velocity profile correction factor, x, Equation 2-5 cannot be solved explicitly and requires an iterative solution. Where the conditions are hydraulically rough, x becomes constant in which case the equation can be solved explicitly.

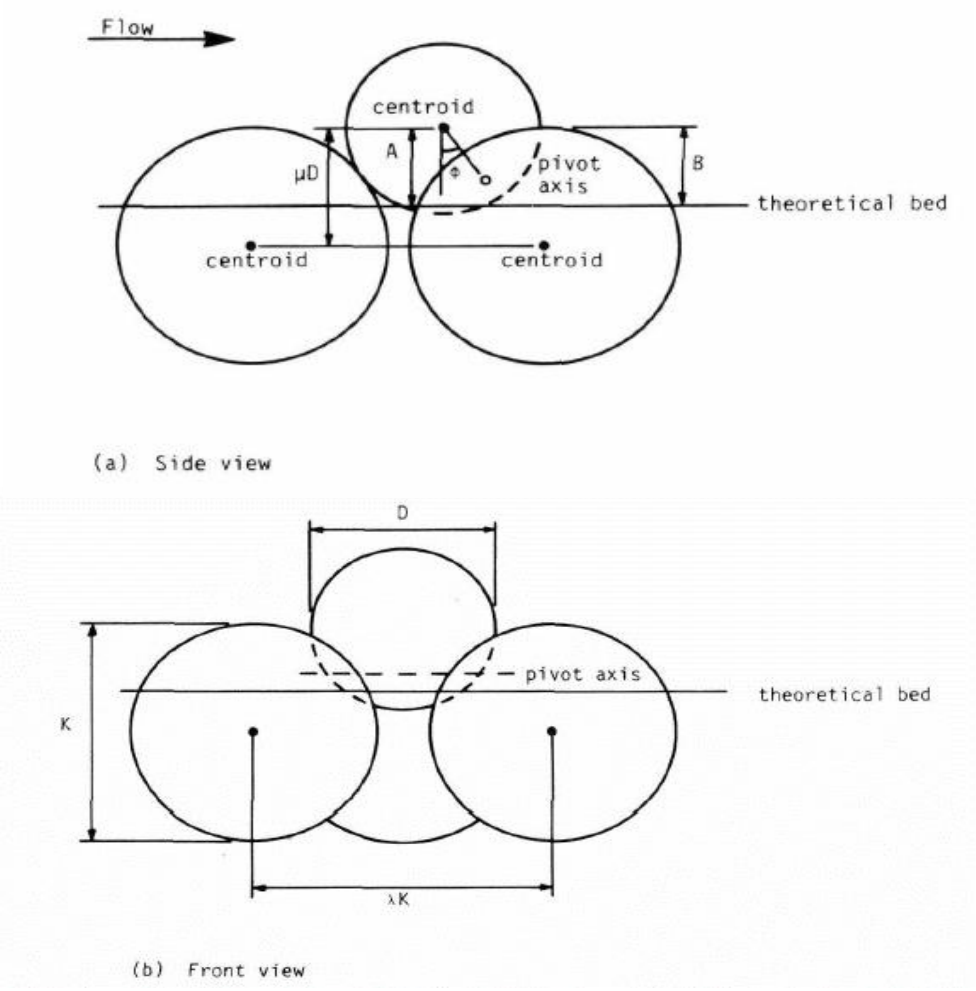


Figure 2-8: Pivoting Geometry (James 1990).

In Figure 2-8, the height of the particle centroid above the theoretical bed is given by *A*, the distance of the theoretical bed below the tops of the bed particles is given by *B*, λ is a proportionality constant for the spacing of the supporting bed particles, and μ is a proportionality constant for the particle centroid elevation above the bed material centroid.

2.3.9 Drag Coefficient

The exposure to a discharge is different for boulders and the bed material. The bed material is most likely to be submerged and thus the determination of the drag coefficient, C_D, is significantly easier. Boulders, however, are potentially exposed to flow conditions that are emergent, near emergent, or emerged. Boulders

introduce local flow distortions that complicate an exact solution for drag forces, especially for shallow flows and emergent boulders (Carling et al. 2002a).

Flammer et al. (1970) studied free surface effects of flow over hemispheres under a range of conditions. The focus of their experiments was to present data for the general drag problem with free surface effects (finite, nonuniform flow field). They exposed the individual hemispheres to various flow conditions, from infinite uniform flow (deep flow where the relative depth has no effect on the drag) to finite nonuniform flow (shallower depths where drag is affected as the relative depth decreases) with free surface effects, each time changing a single flow characteristic in order to accurately establish the effects of such a change. Using hemispheres fixed to a flat disk which was then attached to a strain-gauge, the forces were calculated and the drag results were summarized into three categories: pronounced free surface effects, moderate free surface effects, and negligible free surface effects.

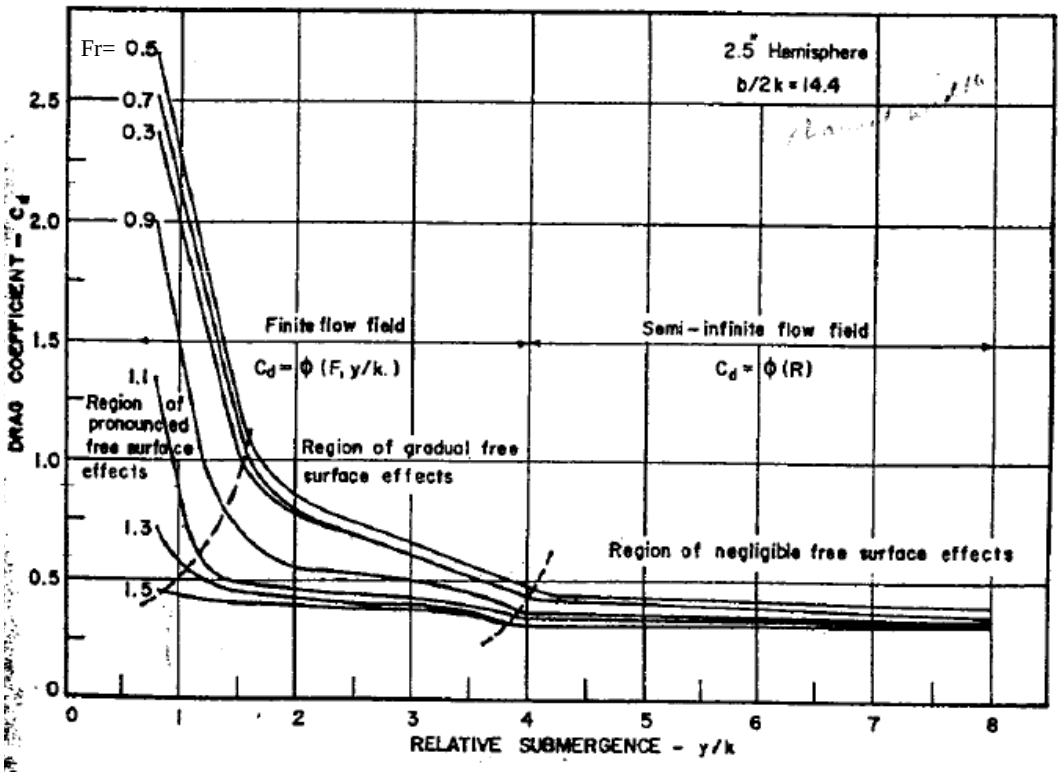


Figure 2-9: Relationship for relative submergence and drag coefficient for hemispheres. (Flammer et al, 1970).

Pronounced free surface effects are seen when the relative depth is less than 1.6. with the drag coefficient increasing up to 10-fold when compared to flow having negligible free surface effects (Flammer et al. 1970). The increase in drag coefficient for moderate free surface effects is less than two-fold. This condition is evident for relative flow depths less than 4 but greater than 1.6. Negligible free surface effects exist for relative depths greater than 4.

Carling et al. (2002a) found that the literature relating drag and lift coefficients (C_L) for immersed or emergent boulders was poorly quantified. They studied drag specifically for rectangular blocks in turbulent flows to determine more accurate drag coefficients for entrainment conditions. Their results focused on the sliding mechanism of entrainment and did not determine drag coefficients for pivoting because the area of the boulder exposed to flow is variable during the pivoting process for rectangular blocks and thus the drag coefficient is also variable. They do however state that, for the rectangular blocks tested, when pivoting was the mechanism for initial motion, the pivoting was induced under emergent flow conditions.

The results of their experiments showed that, for conditions of incipient motion by sliding, the drag coefficient is strongly related to relative water depth. When the blocks were fully submerged, they obtained drag coefficients of 0.95, but under near emergent and emergent flow conditions the drag coefficient increased rapidly as the relative depth reduced. The submerged case related to relative depths greater than 2 for their experiments.

2.3.10 Lift Force

Marsh et al. (2004) reviewed the work of several authors and found that several experiments were conducted where the lift force was measured at different distances from the channel boundary. The results of these studies showed that the maximum magnitude in lift force for particles occurred at the channel boundary with a rapid decrease in the force as the particle was moved away from the boundary to the point where the lift force is negligible for suspended particles.

James (1990) proposed Equation 2-6 to calculate the lift coefficient for naturally packed sediments:

$$C_L/C_D=0.5 \qquad \text{for } Re_*\geq 150 \qquad (2\text{-}6a)$$

$$C_L/C_D=-0.560+0.212 \ln Re_* \qquad \text{for } Re_*\leq 150 \qquad (2\text{-}6b)$$

To test the suitability of Equation 2-6, Marsh et al. (2004) extracted data from studies where there was an appreciable protrusion of the test particle from the test bed and lift coefficients were computed. They studied nine different experiments and found the data forms to vary between experiments. Despite the scatter, there is a clear decrease in the lift coefficient for low particle Reynolds numbers. They concluded that Equation 2-6 provided a reasonable fit for the data but suggested a lower limit of -0.3 for C_L and a constant C_L of 0.2 for Re_* values greater than 100.

Carling et al. (2002a) stated that under emergent conditions the lift coefficient is zero. When rectangular blocks were submerged, the greater the relative submergence the lift coefficient tends to a constant value in the order of ten percent of the drag coefficient. They measured two data points where relative submergence was less than unity yet the block still experienced lift forces. They put this down to shallow flows inducing a standing wave above the block that could result in there being a weak negative lift.

2.3.11 Velocity vs Shear

When determining the incipient motion condition, it can be defined in terms of average flow velocity or average shear stress. Shear stress is a computed quantity whereas average velocity can be directly and easily measured. Thus, it is felt that average velocity is preferable to average shear when incipient motion condition is to be defined (Prakash 2010).

Flammer et al. (1970) used the mean velocity over the flow depth by introducing a velocity profile parameter. They established that the drag coefficients they

calculated were independent of the velocity profile shape for the range between uniform and logarithmic. Carling et al. (2002a) stated that the velocity integrated over the height of an obstacle will give a larger drag coefficient than using one velocity measured above, or integrated over, the height of the boundary layer. They used both approaches but found no statistically significant difference in their results. The incipient motion condition for this study will be expressed in terms of average velocity over flow depth.

2.4 Data Scatter

Shvidchenko and Pender (2000) states that an obvious source of data scatter across the various experiments they studied was the subjectivity in identifying the incipient condition for sediment transport. They suggest that sediment entrainment is not a sudden event but rather a gradual process that is characterized by increasing frequency of particle displacement as flow strength rises.

Hoffmans (2010) suggests that the difficulty is defining incipient motion, as particle movement occurs suddenly where, usually, only a few particles may be moved by the flow near the incipient motion for turbulent flow.

Prakash (2010) summarized that incipient motion has been defined, in past research, as a) Single particle moving, b) A few particles moving, c) General motion of the bed material or d) Limiting condition when the rate of sediment transport tends to zero. Shvidchenko and Pender (2000) suggest that Shields (1936) determined critical shear stress corresponding to "zero sediment transport" by extrapolating backward measured transport rating curves, but Motamedi et al. (2010) state that experiments by Taylor and Vanoni (1972) showed that the Shields diagram corresponds not to zero transport but to a small observable transport rate. This statement of “small observable transport rate” reaffirms the subjectivity in defining incipient motion. Motamedi et al. (2010) suggest [via Church (1978)] that scatter in emperical threshold diagrams could also be affected by variable particle packing.

Paintal (1971) and Lavelle and Mofjeld (1987) surmised that even at very low flows, there is always some probability that some grains could be displaced by turbulent pulsations and thus it is difficult to establish a flow condition below which there would be no movement of sediments.

The nature of incipient motion for sediments is inherently stochastic and therefore needs an appropriate probabilistic description. Due to the variability stated, there is a considerable range of critical Shields stress values found in literature, with values for τ_{*c} ranging from 0.01-0.12 for particle Reynolds numbers higher than 500 (Motamedi et al. 2010).

The difficulty with determing the incipient flow conditions is simplified significantly for boulders as they are a singular entity with which movement is being observed.

3 EXPERIMENTAL INVESTIGATION

3.1 Introduction

The experimental investigation consisted of two experiments that were run in two separate flumes in the hydraulics laboratory of the School of Civil and Environmental Engineering, University of the Witwatersrand.



Figure 3-1: Tilting flume in the School of Civil and Environmental Engineering Hydraulics Laboratory.

The first set of experiments was run in a tilting flume (Figure 3-1) with the objective of determining the flow conditions under which various boulders would pivot over a controlled axis. The experiments were idealized for repeatability and limited to uniform flow conditions. Boulders of different sizes and different densities were rested individually on a base of three identical spheres (Figure 3-5) and subjected to flow that was increased until the boulder was displaced. The flow was kept uniform by means of an adjustable weir downstream of the boulders.

The experiment was run for several bed slopes and then the boulders were placed at various levels of embedding into the bed material for a single bed slope.

The second set of experiments was run to calibrate the drag coefficients used in the model developed to determine the stability of the boulders. The experimental setup was based on work by Jackson (2016) and the experiments were run in a separate zero-slope flume (Figure 3-2). The experiments involved suspending boulders a negligible distance from the bed material and measuring the forces exerted on the boulder under various discharges. The boulders were subjected to various flow depths and velocities for each discharge by adjusting the downstream weir.



Figure 3-2: Zero-slope flume in the School of Civil and Environmental Engineering Hydraulics Laboratory (Jackson 2016).

3.2 Boulder Incipient Motion Experiments

3.2.1 Apparatus

- 0.9m width within a 2.0m wide horizontal tilting laboratory flume with downstream V-notch weir and in-line flow meter
- Adjustable weir on downstream end of flume
- "Water Flume" Software to control flume slope and water flow rates
- Standard face bricks
- Lego bricks
- Pebbles of 2.5cm mean diameter
- 2.5cm concrete spheres and hemispheres
- 7 boulders (50mm, 3x 80mm, 100mm, 120mm, 150mm diameters)- hollow steel balls filled with grains to create boulders with densities ranging from 1591kg/m^3 to 2240kg/m^3. The 80mm boulders were filled with grain, sand, and plastic pellets for densities of 1877kg/m^3, 2335kg/m^3, and 1645kg/m^3 respectively. Hollow steel balls were chosen for the boulders because they were easily available and their densities could be manipulated by their fill material.
- Measuring tape fixed to the wall of the flume

3.2.2 Flume and boulder setup

Flume C, in the hydraulics laboratory, was used for this experiment. It is a 2.0m wide flume that was narrowed to 0.90m so that sufficient depths of flow could be achieved for a range of discharges. This width was chosen as Flume A, used in the drag calibration experiments, is 0.90m wide which makes applying the drag calibrations simpler.

Discharge into the flume is controlled by a computer operated valve leading from a constant head tank. The discharge was measured by an inline flow meter with digital display and verified with a downstream V-notch weir and calibrated rating equation. Flow depths and flow velocities in the flume were set by adjusting the discharge valve, the downstream weir, or a combination of both.

A 10m length of the flume wall is made of clear Perspex panels on which sections of measuring tape were glued so that flow depth could be measured (see Figure 3-3).



Figure 3-3: Section of Flume C with clear Perspex and measuring tape for measuring flow depths.



Figure 3-4: Flume C lined with bricks and pebbles to create artificially raised bed.

The objective with embedding the boulders is to determine how much the stability of the boulder is increased. This requires the bed of the flume to be raised such that the boulders can be embedded in a controlled manner which is achieved by lining the flume with face bricks and smooth pebbles (Figure 3-4). Half way down the length of the flume, two face bricks were removed and a block of Lego was placed in the gap (Figure 3-5). This allowed the boulders to be embedded by removing layers of Lego while keeping the rest of the bed material unchanged.

For the tests where the boulders were not embedded, the boulders were placed on a base of three 2.5cm spheres that were glued to the top of the Lego block (Figure 3-5). This enables the pivot axis to be calculated mathematically and keeps it controlled for each boulder size. The base was orientated so that a flat side of the triangle was downstream and perpendicular to the flow.



Figure 3-5: Lego brick used to alter the depth of the boulder; Triangular base of 3 spheres for boulders to rest on.

Figure 3-6 a and b show how the boulder was placed for conditions of no embedding and embedding, respectively. When embedding was required, 2.5cm spheres were placed on bricks in front of the boulder to control the pivot point of the boulder. The spheres in Figure 3-6 b that the boulder pivots over were separated by 31.3mm centre to centre (5.8mm free space between the two spheres) to bring the pivot location closer to the boulder centroid. This was done to make sure that the boulders could still pivot out of place within the discharge range of the flume system. The model presented in Chapter 4 accounts for this.

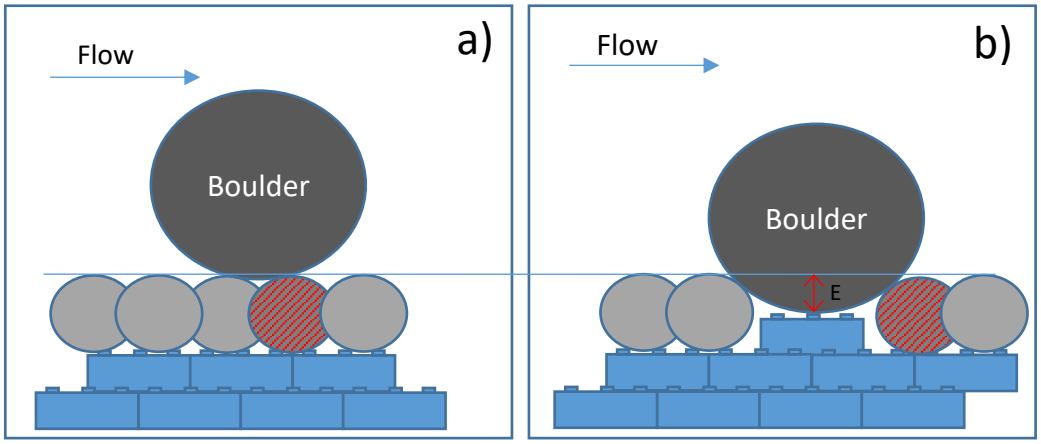


Figure 3-6: Schematic of boulder setup with hatched spheres representing the pivot spheres (a: no embedding, b: embedded a distance E).

3.2.3 Test conditions

The aim of the experiments was to test the stability of a variety of boulders under different conditions. To do this, a control experiment was identified and various parameters were independently changed so that the effect of the change could be analysed.

The general control experiment (Experiment 3):

- 80mm diameter boulder
- Boulder filled with grain
- Boulder not embedded
- Slope of flume set to 0.00646

The variations in the experiments:

1) The size of the boulder was varied and there was no embedding.
2) The slope of the flume was varied for two boulders to analyse the incipient motion conditions for different relative depths.
3) The relative density of the 80mm boulder was changed

4) The level of embedding was increased for each of the boulders on a single slope

Although experiment 3 is used as the general control, the slope and embedded variations were performed on the other boulder sizes as well and thus the "Control Experiment" in Table 3-1 refers to the appropriate boulder size when the variation is the slope or the embedment.

Round elements were used to keep the experiments as ideal as possible. The flow was also kept uniform throughout the experiments to simplify the calculation of the average velocity.

Table 3-1: Experimental conditions with comparison to a control experiment for each incipient motion experiment.

Exp.	Boulder ID (mm)	Boulder Size (mm)	Density (kg/m^3)	Embed (mm)	Pivot Separation (mm, c to c)	Slope	Control Experiment	Variation	Change	Unit
1	50	50	2,240	0.00	0	0.00645	3	Boulder Size	-30	mm
2	50	50	2,240	0.00	0	0.00645	3	Boulder Size	-30	mm
3	80A	80	1,877	0.00	0	0.00646	3	Boulder Size	0	mm
4	100	100	1,591	0.00	0	0.00646	3	Boulder Size	20	mm
5	120	120	1,682	0.00	0	0.00646	3	Boulder Size	40	mm
6	150	150	1,558	0.00	0	0.00646	3	Boulder Size	70	mm
7	80A	80	1,877	0.00	0	0.00518	3	Slope	-0.00128	
8	100	100	1,591	0.00	0	0.00518	4	Slope	-0.00128	
9	80A	80	1,877	0.00	0	0.00261	3	Slope	-0.00385	
10	100	100	1,591	0.00	0	0.00261	4	Slope	-0.00385	
11	80A	80	1,877	0.00	0	0.00134	3	Slope	-0.00511	
12	100	100	1,591	0.00	0	0.00134	4	Slope	-0.00511	
13	80A	80	1,877	0.00	0	0.00390	3	Slope	-0.00256	
14	100	100	1,591	0.00	0	0.00390	4	Slope	-0.00256	
15	80A	80	1,877	0.00	0	0.00582	3	Slope	-0.00064	
16	100	100	1,591	0.00	0	0.00582	4	Slope	-0.00064	
17	80A	80	1,877	0.00	0	0.00710	3	Slope	0.00064	
18	100	100	1,591	0.00	0	0.00710	4	Slope	0.00064	
19	80A	80	1,877	0.00	0	0.00646	3	Embed	0.00	mm
20	100	100	1,591	0.00	0	0.00646	4	Embed	0.00	mm
21	50	50	2,240	6.34	31.3	0.00648	2	Embed	6.34	mm

22	80A	80	1,877	6.34	31.3	0.00648	3	Embed	6.34	mm
23	100	100	1,591	6.34	31.3	0.00648	4	Embed	6.34	mm
24	120	120	1,682	6.34	31.3	0.00648	5	Embed	6.34	mm
25	150	150	1,558	6.34	31.3	0.00648	6	Embed	6.34	mm
26	80B	80	1,645	6.34	31.3	0.00646	36	Embed	6.34	mm
27	80A	80	1,877	6.34	31.3	0.00646	3	Embed	6.34	mm
28	80C	80	2,335	6.34	31.3	0.00646	38	Embed	6.34	mm
29	80B	80	1,645	7.94	31.3	0.00647	36	Embed	7.94	mm
30	80A	80	1,877	7.94	31.3	0.00647	3	Embed	7.94	mm
31	100	100	1,591	7.94	31.3	0.00647	4	Embed	7.94	mm
32	120	120	1,682	7.94	31.3	0.00647	5	Embed	7.94	mm
33	80B	80	1,645	9.53	31.3	0.00647	36	Embed	9.53	mm
34	80B	80	1,645	11.13	31.3	0.00647	36	Embed	11.13	mm
35	50	50	2,240	0.00	0	0.00645	3	Boulder Size	-30	mm
36	80B	80	1,645	0.00	0	0.00647	3	Density	-232	kg/m^3
37	80A	80	1,877	0.00	0	0.00647	3	Density	0	kg/m^3
38	80C	80	2,335	0.00	0	0.00647	3	Density	458	kg/m^3
39	100	100	1,591	0.00	0	0.00647	3	Boulder Size	20	mm
40	120	120	1,682	0.00	0	0.00647	3	Boulder Size	40	mm
41	150	150	1,558	0.00	0	0.00647	3	Boulder Size	70	mm
42	80B	80	1,645	0.00	0	0.00519	43	Density	-232	kg/m^3
43	80A	80	1,877	0.00	0	0.00519	7	Density	0	kg/m^3
44	80C	80	2,335	0.00	0	0.00519	43	Density	458	kg/m^3
45	80B	80	1,645	0.00	0	0.00391	46	Density	-232	kg/m^3
46	80A	80	1,877	0.00	0	0.00391	13	Density	0	kg/m^3
47	80C	80	2,335	0.00	0	0.00391	46	Density	458	kg/m^3

3.2.4 Research methodology

In the controlled environment of a laboratory flume, incipient motion studies approach the problem by slowly increasing flow velocity until the initial motion of bed materials is observed. This control is not possible in field studies and conditions are generally monitored over a range of flow conditions and the incipient conditions are then extrapolated (Motamedi et al. 2010).

The procedure followed in this study was the same as described above, the main difference being that the incipient motion was for a single boulder and thus it is

much easier to identify when the boulder moved. The movement could be a teeter but for these experiments incipient motion was defined as the boulder being dislodged completely from the base of spheres it was sitting on.

The following procedure was followed when carrying out the non-embedded experiments:

1. The triangular sphere base was placed on the Lego block and the pebbles were levelled around it to make a uniform bed profile.
2. The slope of the flume was set using the "Water Flume" software required to operate the flume's hydraulic jacks.
3. A boulder was placed on the triangular base.
4. The inline flow meter was turned on.
5. The valves from the head tank were opened.
6. The "Water Flume" software was used to set the flow in the flume.
7. Wait for flow rate to stabilize.
8. If the boulder didn't move after waiting 5 minutes, increase the flow rate using the software.
9. Steps 7 and 8 were repeated until the boulder moved.
10. Once the boulder had dislodged, it was removed from the flume and the flow depth was measured at 3 locations along the length of the flume.
11. The slope of the flume was confirmed by measuring the drop of the hydraulic jacks using a dial gauge.
12. If the flow was uniform, steps 13 and 14 were skipped and step 15 was followed.
13. If the flow wasn't uniform, the weir at the end of the flume was adjusted and the process was repeated from step 10 (at this point the boulder was not placed back onto the triangular base as the weir was being adjusted for the flow that already dislodged the boulder).
14. Once uniform flow was achieved, all the valves were closed and the water drained from the flume. The boulder was placed back in position on the pivot spheres and the process went back to step 5 to confirm the flow conditions required to dislodge the boulder.

15. The inline flow rate was recorded and confirmed using the V-notch weir.
16. All the valves were closed and the water drained out of the flume.
17. A different boulder was selected and the process was repeated from step 2.

The procedure was followed for conditions 1, 2, and 3 in section 3.2.3 above. For condition 4, the embedded condition, the same procedure was followed for steps 2 through 15 but step 1 was altered.

For the embedded experiments, instead of placing the boulder on the triangular base, the boulder was placed upstream of 2 pivot spheres (as shown in Figure 3-7). There was difficulty in ensuring that the boulder was sitting flush with the two spheres downstream of it while still sitting on smaller spheres. It was thus necessary to remove the spheres below the boulder and raise the level of the Lego the boulder was sitting on. This allowed for accurate measurement of the level of embedding. By removing the spheres below the boulder and raising the Lego, the bed upstream of the boulder was affected. Lego bricks were placed directly upstream of the boulder to the same level as the bed material so that the effect of embedding was maintained (Figure 3-7).

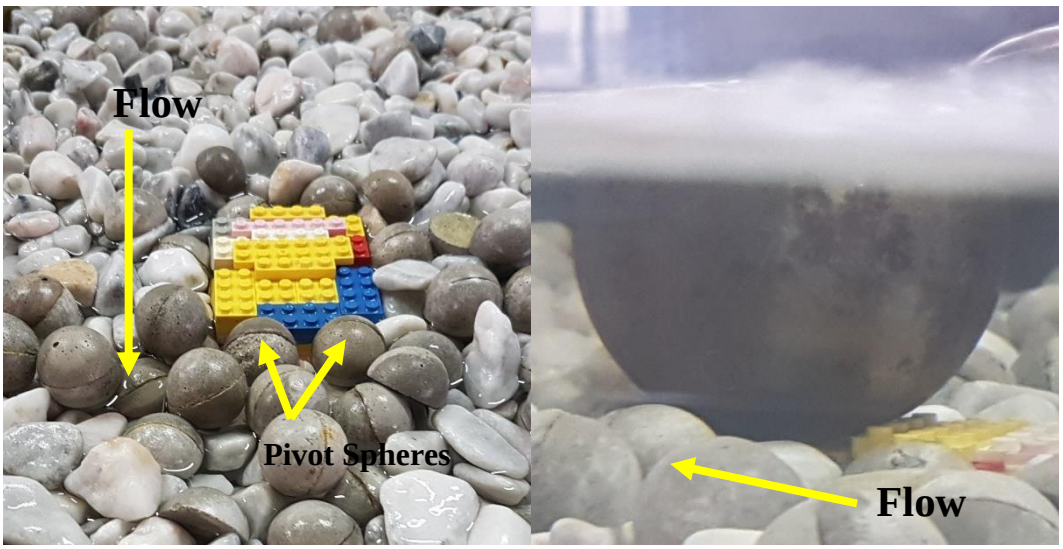


Figure 3-7: Lego configuration for boulder being embedded.

On the first attempt at embedding the boulders, the spheres over which the boulders needed to pivot were in direct contact with each other. This geometry gives the longest pivot length for the boulders to overcome and given the maximum possible flow possible in the flume, none of the boulders moved. It was

necessary to separate the pivot spheres, to reduce the pivot length, so that data could still be collected for the embedded condition. This separation is accounted for in the model.

3.3 Drag Coefficient Calibration Experiments

3.3.1 Apparatus

- 0.9m wide horizontal flume
- Weir on downstream end of flume
- Specially constructed load measurement apparatus
- Lorenz Messtechnik K1107 load cell with data cable
- Laptop with installed load cell drivers and software
- Standard face bricks
- Lego bricks
- Pebbles of 2.5cm mean diameter
- 2.5cm concrete spheres and hemispheres
- Digital point gauge
- Stop watch

3.3.2 Flume and boulder setup

To measure the forces on the boulder so that drag coefficients could be determined, a special load cell apparatus was needed. This experiment used the same equipment and a similar setup as described in Configuration 3 of Jackson (2016). A hole was drilled and tapped into each of the boulders so that they could

be attached to a rod that would then be attached to a support box suspended above the flume (Figure 3-8).



Figure 3-8: Apparatus for drag coefficient experiments.

The flow exerted a force on the boulder which created a moment about a pin (see Figure 3-9), with the apparatus setup such that the flow was perpendicular to the pivot axis. A vertical lever arm that extended from the boulder beyond the pin was attached to the load cell/tension sensor and the resolution of moments about the pin allowed the force on the boulder to be calculated, with the load cell set up in such a way that the force applied to the tension sensor is always applied through the plate that the rod is attached to (see Figure 3-9 and Figure 3-10). The rod is fixed to the plate by tightening a bolt on either side of the plate and because of the plate resting on bearings, the force always acts a fixed distance from the point

about which the moment is calculated. This statement is only strictly true if the rod does not move relative to the plate; in this case the movement is considered too small to measure and a correction factor, taken from Jackson (2016), is applied. This allows the force on the boulder to be calculated by simply multiplying force measured on the tension sensor by the ratio of the lever arms. Again, this theory is only strictly true if the lever arm distance doesn't change. Because the plate remains horizontal throughout the experiments, when a force is applied the plate is displaced, as indicated in Figure 3-10. This displacement was not measured and a correction factor, taken from Jackson (2016), was applied (see Chapter 3.3.5).

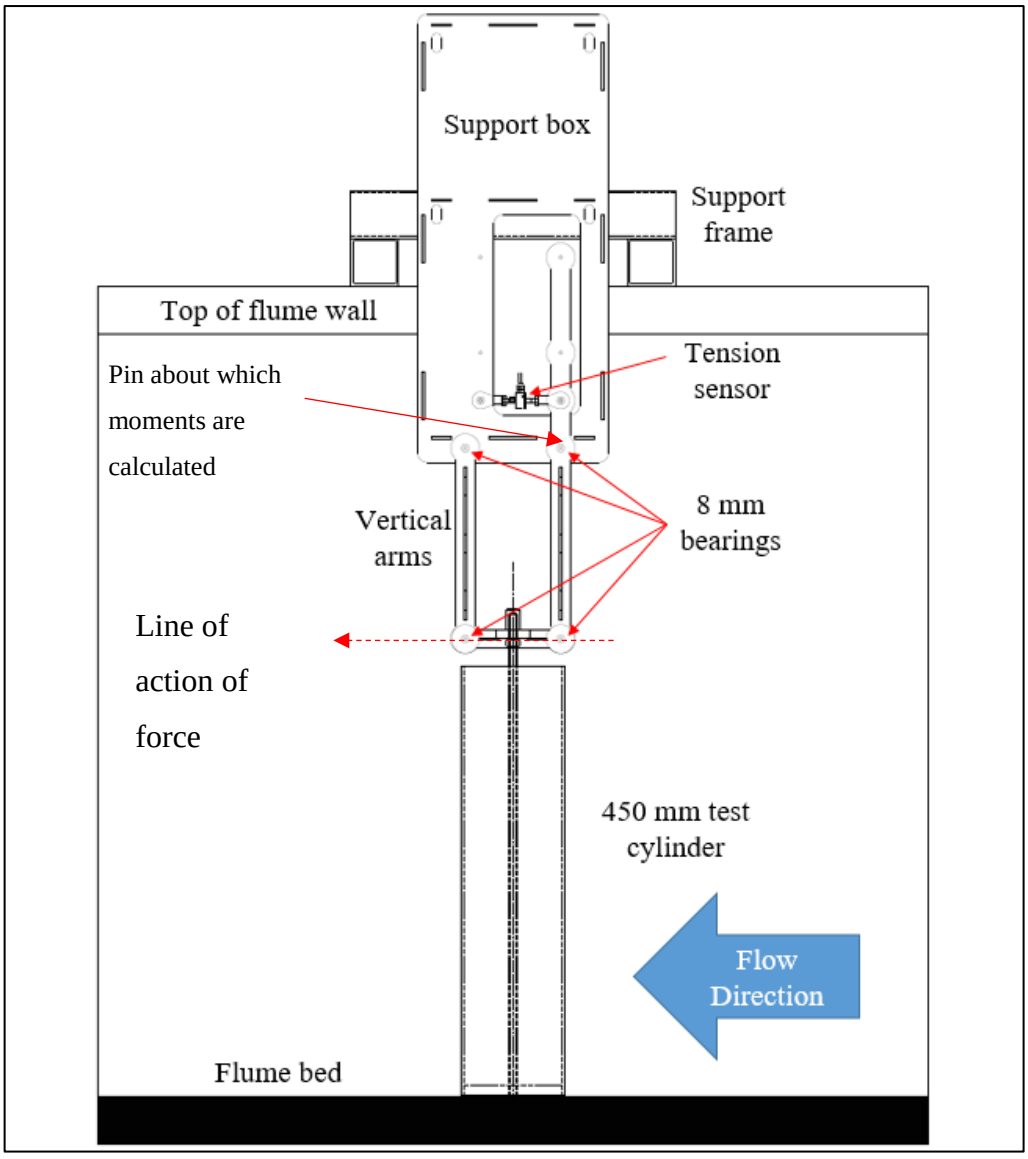


Figure 3-9: Schematic of set up taken from Jackson (2016).

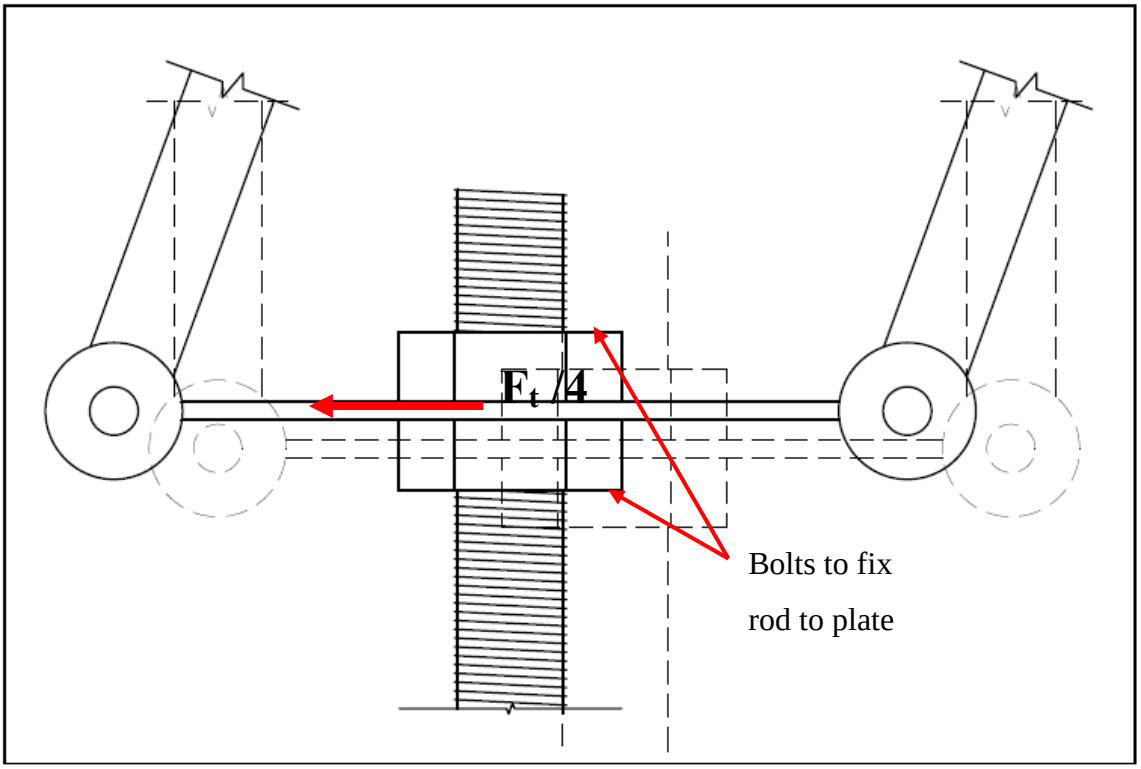


Figure 3-10: Schematic of rod fixed to load cell where $F_t/4$ is the force acting through the plate. Dashed lines indicate plate in rest position and solid lines represent plate after a force is applied.

As with the incipient motion experiments, the zero-slope flume was lined with bricks and pebbles. Once again, two bricks were replaced with the block of Lego to allow for the boulders to be embedded. With the incipient motion experiments, the boulders rested on a base of smaller spheres whereas this experiment required the boulder to be suspended a negligible distance from the bed material. The reason for this was so that when the boulder was exposed to flow it did not have resisting forces from the bed material. This way the only force resisting the boulder's movement was the load cell and the force exerted on the boulder from the flow could be measured to calculate the drag coefficient. When embedding the boulder, the bed material downstream of the boulder was manipulated to make sure that there was no contact with the bed when the boulder moved. This is a deficiency in the testing method and the consequence of this is discussed in section 5.1.

A digital point gauge was attached to the support frame that the load cell was suspended from to measure the flow depths.

3.3.3 Test conditions

The experiments were run in a zero-slope flume and thus the combination of flow rate and flow depth required for movement, as described in section 3.2.3, were not repeatable. It was also not possible to achieve uniform flow for these experiments.

Like Flammer et al. (1970), the drag coefficients for different relative depths needed to be determined. Thus, if the flow rate was known and the force could be measured, the flow depth only needed to be measured at the same point in the flume as the boulder.

The aim of this research was not to provide a thorough investigation of drag coefficients for spheres on a smaller substrate or an embedded sphere and thus the experiments weren't as rigorous. The Reynolds number for the boulder experiments in Chapter 3.2 ranged from 7.27×10^4 to 1.86×10^5 while the Reynolds number for the drag coefficient calibration experiments in this chapter ranged from 9.20×10^4 to 1.65×10^5.

The software used to record the force readings allows the frequency of the readings to be chosen. The more readings per second, the less time available to run the flume before there are too many readings for the load cell to save to the output file. Because of the sensitivity of the sensor, any surges, caused by adjusting the flow, could skew the data. In order to determine if a particular set of data was valid, the sensor was zeroed before any flow was discharged in the flume and readings were taken until there was no longer any water flowing around the boulder. If the readings were the same before and after the flow was introduced and stopped, the data set was saved and the next run of the experiment could proceed. Flow had to be increased gradually to limit the surge from adjusting the flow, each flow depth had to stabilize before an average reading could be calculated for a particular flow, and once the valves were closed to have no flow,

it took some time for the head to drop such that there was no water flowing around the boulder.

For these reasons, the tests for each boulder were limited to recording the forces for only 4 or 5 flow depths:

1. The relative depth was greater than 1.5
2. The relative depth was greater than 1.2 but less than 1.5
3. The relative depth was as close to 1.0 as possible
4. The relative depth was between 0.5 and 1.0

The majority of incipient motion experiments were run using the 80mm boulder and thus this boulder size was used for the majority of the drag calibration experiments. The incipient motion experiments had flow rates varying from $65m^3$/hr to $127m^3$/hr that dislodged the various boulders for no embedding and flow rates up to $180m^3$/hr for the embedded condition. For this experiment it was decided that only a few flow rates would be tested between the range of $98m^3$/hr and 156 m^3/hr as this incorporated the majority of flow rates identified for incipient motion (Table 3-2).

The 120mm boulder was also used in this experiment to show the influence of size on the drag coefficient, although this was only tested for a higher flow rate.

The 80mm boulder was embedded just once (E/D = 0.1) at a higher flow rate for various relative depths.

Table 3-2: Experimental conditions with comparison to a control condition for each drag coefficient experiment.

Exp.	Boulder Size	Embed	Flow Rate	Flow Depth	y/D	Control Condition	Variation	Change	
	mm	mm	m^3/hr	mm					
1	80	-	147	78	0.98	6	Flow Rate	48	m^3/hr
2	80	-	119	67	0.84	3	y/D	-0.13	
3	80	-	119	78	0.97	6	Flow Rate	20	m^3/hr
4	80	-	99	60	0.75	6	y/D	-0.22	
5	80	-	99	66	0.82	6	y/D	-0.15	
6	80	-	99	77	0.97	6	Flow Rate	0	m^3/hr
7	80	-	99	108	1.35	6	y/D	0.38	
8	80	-	99	147	1.83	6	y/D	0.87	
9	80	8.00	151	79	1.10	1	Embed	8	mm
10	80	8.00	151	110	1.52	7	Embed	8	mm
11	120	-	157	78	0.65	12	y/D	-0.25	
12	120	-	157	108	0.90	6	Boulder Size	40	mm

3.3.4 Research methodology

3.3.4.1 Flow Measurement

The flume used for this experiment has a manual supply valve to control the discharge. To be able to adjust the flow rate with some degree of certainty as to what the discharge would be, the flume was run for various discharges (measured with the inline flow meter as there is no V-notch downstream of this flume) and the number of valve revolutions was recorded.

After the supply valve was successfully calibrated, an error was encountered with the inline flow meter. The flow meter was inspected for damage and to see if something was preventing the vanes from moving freely, but no damage or debris was found. This meant that the inline flow meter could not be used as a reliable measure, and that some other method for flow measurement was needed.

There are two return pipes in the sump at the end of the flume that allow the water to be pumped back to the head tank. If the valves for these pipes were closed, the sump would fill and the flow rate could be determined by measuring the time taken for the water level to pass two markers. The dimensions of the sump were measured and the plan area was calculated.

The supply valve was opened to allow the maximum flow to run through the flume. The return valves were left fully open and once the flow had stabilized, the water level in the sump for this condition was identified. A marker for timing to begin was placed some distance above this normal water level such that the valves could be closed fully before the water level reached the marker while the sump began to fill, otherwise water would be leaving the system while the timer was running.

To achieve the best possible accuracy for measuring the flow rate, the sump needed to fill as much as possible so that a longer time measurement was taken. The water level marker to stop the timer was therefore placed as close to the crest of the sump as possible but low enough so that the return valves could be reopened before the sump overtopped. The distance between markers was measured and the volume to be filled was calculated using the plan area.

The routine of closing the return valves and measuring the time taken to fill between the markers was repeated several times for different flow rates so that the supply valve could be recalibrated. Because the flow rate was a direct measurement of volume divided by time, the flow rates used were deemed to be as accurate as possible.

3.3.4.2 Force Measurement

For each run of the experiments, the support box had to be orientated and levelled to make sure that the pivot axis of the pin was perpendicular to the flow. The levelling was done using a magnetic spirit level that was placed on the side of the box, while the orientation was measured and the support rig the box was screwed into was clamped in place to prevent the box from moving.

Special care had to be taken so as not to overload the tension sensor before the measurements needed to be recorded. For this reason, the procedure to run the experiments was very important (before each experiment was run, the supply valve was fully closed and the flume was drained):

1. The weir at the end of the flume was raised so that the flow reading measurements would start with the boulder being submerged.
2. The boulder being tested was screwed onto the rod to be suspended from the rig. The rod was then inserted into the hole in the middle of the horizontal plate (see Figure 3-10).
3. The boulder was suspended just above the bed material (or to the embedded depth) by adjusting the two nuts on either side of the horizontal plate that held the rod in.
4. The tension sensor was then fastened to the support box and the load cell was connected to the computer. From this stage, it was crucial not to disturb the boulder, suspended rod, or the support box otherwise the tension sensor could be overloaded.
5. The tension sensor software was launched, which detects the tension sensor and displays a digital output (Figure 3-11).
6. The tension sensor is extremely sensitive and needs to be zeroed to make sure that the force readings are indicative of the flow only. This was achieved by starting and stopping the measurements a few times until the sensor remained stable at zero.
7. The digital point gauge was set on the bed and then zeroed. It was then set at a target water depth to ensure consistent relative flow depths were being measured.
8. The measurements were started from the zeroed position and the supply valve was opened slowly so that the flow could build up without creating a surge wave that could either overload the tension sensor or alter the baseline measurement.
9. Once the flow had stabilized, the weir at the end of the flume was adjusted until the flow depth was at the level of the point gauge.

10. When the graph on the sensor software had levelled out, it meant the flow had stabilized. The time at which it levelled out was recorded and the flow depth was measured with the point gauge. The flow was left for 5 minutes to give an average reading over that time.
11. The point gauge was then lowered to the next target depth and the weir was also lowered until the flow depth matched the point gauge.
12. Steps 10 and 11 were repeated until all the target depths had been measured or when the weir was at its lowest position.
13. The return valves at the sump were then closed as quickly as possible. When the rising water level reached the first marker, the stop watch was started. When it reached the second marker, the stop watch was stopped and the return valves were opened. The time taken to fill the sump was recorded to calculate the flow rate.
14. The supply valve was closed and the water was drained out of the flume. Once the water no longer made contact with the boulder, the tension sensor measurements were stopped. At this stage, the readings needed to be zero, otherwise it meant that the sensor had been knocked out of balance and the experiment needed to be rerun.
15. The drag forces for the different flow depths were exported from the software into a CSV file and an image of the graph was exported to JPEG.
16. The CSV file was then imported into Excel where the times recorded in step 10 were used to determine the drag force on the boulder for the different flow depths.

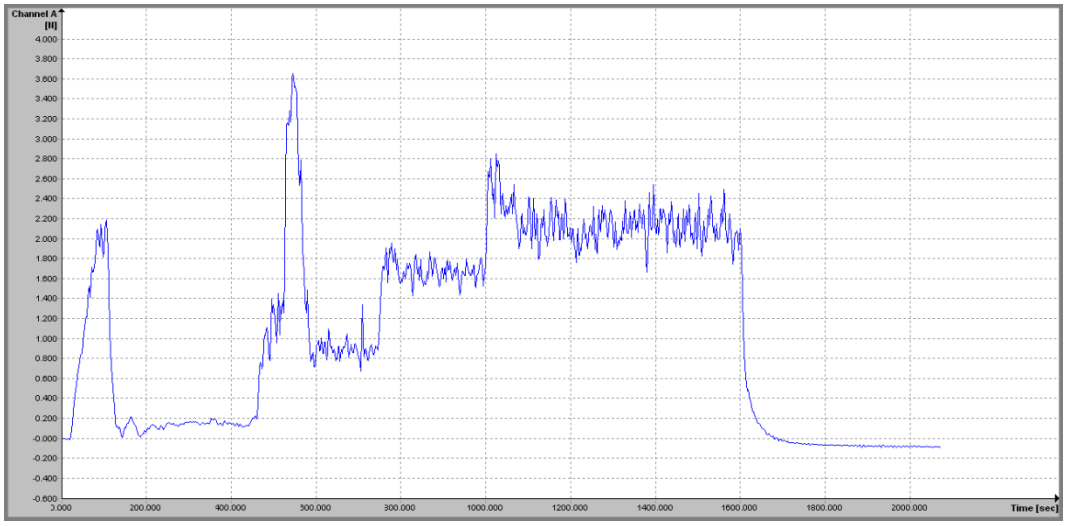


Figure 3-11: Screenshot of software used to record force measurements.

The above procedure was followed for the two sizes of boulders tested and for the embedded experiment. Figure 3-11 is a screenshot of the software used to record readings from the tension sensor and gives clarity on steps 8-12. The readings show a clear spike in the force as the flow was building up and once the boulder was submerged, the force readings levelled out (~200-400 seconds). The next spike was a result of the downstream weir being lowered which lowered the flow depth and thus increased the force on the boulder. The flow was allowed to stabilize (~600 - 750 seconds) before the weir was lowered again. The rate at which the gate was lowered affected how quickly the flow depth dropped and it was clear from the first change in level of the weir (~550 seconds) that a sudden change causes a spike in the force readings; the second weir adjustment (~750 seconds) was more gradual and thus the force reading did not spike as noticeably. After the flow had stabilized and the flow rate had been measured, the supply valve was closed and the force readings were recorded until the head in the tank had fully discharged so that the boulder was no longer subjected to any flow.

3.3.5 Calculating the Drag Coefficient

Equation 3-1 was used as the basis to calculate the drag coefficient for each boulder based on the average force recorded for each flow condition.

$$C_D = \frac{2F_D}{A_n \rho_w V^2} \quad (3\text{-}1)$$

where

$$F_D = \frac{F_t}{4 \times CF} \quad (3\text{-}2)$$

As explained in Chapter 3.3.2, the force in the tension sensor (F_t) is divided by 4 because of the resolution of moments about a pin. The calibration factor, CF=0.7827, is taken from Jackson (2016). The velocity used for the calculation was the average velocity as calculated by dividing the flow depth by the flow depth and the flume width. The area of the boulder exposed to flow (A_n) is calculated from Equation 4-16.

4 MODEL ANALYSIS

4.1 Introduction

Table 3-1 shows that there were 47 iterations of the boulder incipient motion experiments but the data from these experiments is insufficient to produce an empirical model for predicting the incipient condition for a boulder. The data can, however, be used to verify a theoretical model.

4.2 Developing the Model

4.2.1 Basis of model

James (1990) developed a comprehensive model for predicting the entrainment conditions of non-uniform, non-cohesive sediments. That model was derived making as few assumptions as possible so that it could be applied to a wide range of problems, but because it was derived for sediments there needed to be some manipulation to make it applicable to boulders that may or may not be submerged.

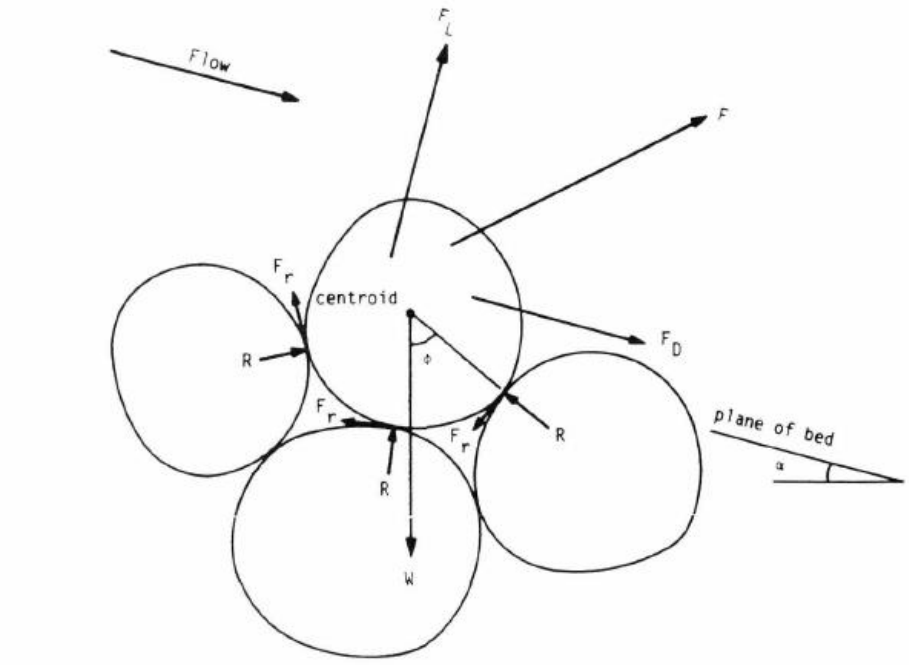


Figure 4-1: Forces acting on a particle (James 1990).

This model is derived on the assumption that the boulders being analyzed will pivot out of position. This means that the forces acting on the boulder can be resolved around a pivot axis and the resolution of moments about this pivot axis determines whether the boulder is stable or not. If the destabilizing moments are greater than the stabilizing moments, the boulder will pivot over said axis and move downstream. The model is limited to determining the stability of the boulder in its initial condition before pivoting out of place and ignores the conditions required for the boulder to stop moving.

Figure 4-1 and Figure 4-2 are used as the basis of the moment equilibrium equation. The forces are applied a perpendicular distance away from the pivot axis and thus the moments about this axis can be resolved to give:

$$(Wcos\alpha) \times (a\ sin(\alpha + \phi)) = (Wsin\alpha) \times (acos(\alpha + \phi)) + F_D b + F_L c \quad (4\text{-}1)$$

W represents the submerged weight of the boulder acting through the centroid of the boulder which is a distance, *a*, from the pivot axis. F_D and F_L represent the drag and lift forces, while *b*, and *c* represent the lever arms from the pivot axis for each of these forces respectively. The angles α and ϕ represent the bed slope angle and the pivot angle.

The friction and normal reaction forces in Figure 4-1 are reduced to zero when the boulder is at the point of incipient motion and are therefore not included in the equation. The left side of Equation 4-1 represents the stabilizing moment acting on the boulder while the right side represents the destabilizing moments.

4.2.2 Geometry of the model

The pivot angle is the angle between the line of action of the weight of the boulder, acting through its centroid, and the imaginary line between the boulder centroid and the pivot axis which is dependent on the composition of the bed material that the boulder is resting on and the slope of the bed material. Equation 4-2a applies for non-embedded boulders (derived from Figure 4-2bii), while Equation 4-2b is used for embedded boulders (derived from Figure 4-2cii).

$$\Phi = arctan\frac{\left(\frac{\lambda K}{2\sqrt{3}}\right)}{A} - \alpha = arctan\frac{\frac{\lambda K}{2\sqrt{3}}}{\sqrt{\frac{(K+D)^2}{4} - \frac{(\lambda K)^2}{3}}} - \alpha \qquad (4\text{-}2a)$$

$$\Phi = arccos\frac{\mu D}{a'} - \alpha = arccos\frac{\mu D}{\sqrt{\frac{(K+D)^2}{4} - \frac{(\lambda K)^2}{4}}} - \alpha \qquad (4\text{-}2b)$$

Where λ is a proportionality constant for the spacing of the bed material, μD is the elevation of the boulder centroid above the centroid of the bed material, and *a'* is the distance between boulder and bed particle centroids.

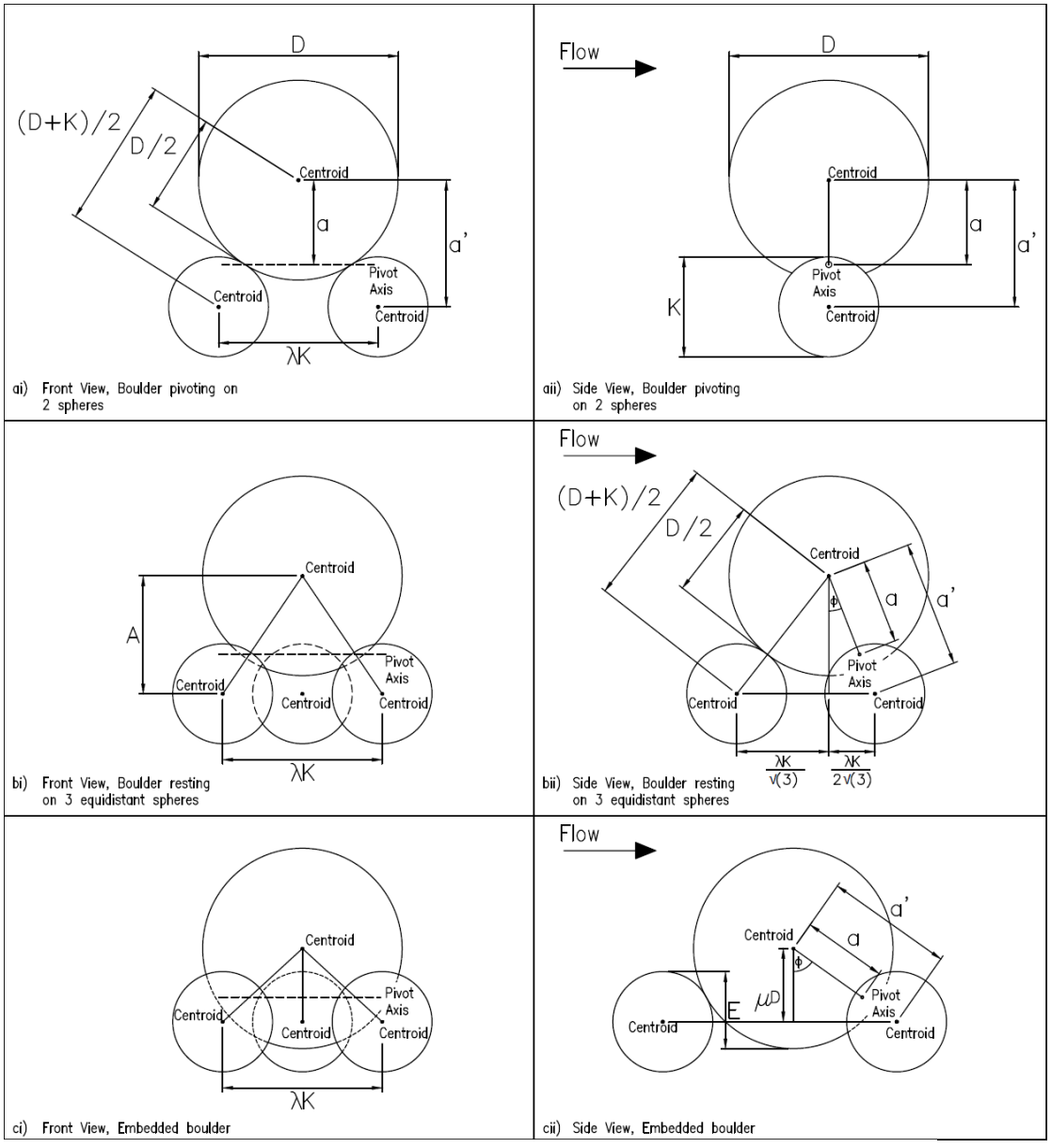


Figure 4-2: Pivoting geometry on bed material slope α=0°.

For the case where the boulder is sitting on 3 equidistant particles that are in contact with each other, λ=1.0. For the case accounting for protrusion effects (embedding), λK simply represents the distance between the bed particle centroids and for these experiments λK fixed and was thus a measurable value.

Before the value of μD can be determined, it is important to understand the assumption made regarding the position of the theoretical bed depicted in Figure 4-2. The theoretical bed for these calculations is assumed to run through the centroid of the bed material and thus the value of *B* is always *K/2*. This means that when the boulder is not embedded into the bed material, μD is equal to the distance between the boulder centroid and theoretical bed elevation, *A* in Figure 4-2bi, calculated from Pythagoras as:

$$A = \sqrt{\frac{(K+D)^2}{4} - \frac{(\lambda K)^2}{3}} \qquad (4\text{-}3)$$

For the case where the boulders are embedded, μD depends on how much the boulder is embedded where *E* is measured as a depth from the top of the bed particles:

$$\mu D = A \qquad for \quad E = 0 \qquad (4\text{-}4a)$$

$$\mu D = \frac{K}{2} + \frac{D}{2} - E \qquad for \quad \frac{K}{2} + \frac{D}{2} - E < A \qquad (4\text{-}4b)$$

The boulder centroid and the pivot axis are separated by a distance *a*, the boulder centroid and bed material centroid separated by *a'*, and using similar triangles:

$$a = \frac{a'D}{(D+K)} = k_2 D \qquad (4\text{-}5)$$

Where k_2 is a proportionality constant given by:

$$k_2 = \frac{1}{(D+K)} \sqrt{\frac{(K+D)^2}{4} - \frac{(\lambda K)^2}{4}} \qquad (4\text{-}6)$$

4.2.3 Submerged Weight of Boulder

In James' model, *W* refers to the submerged weight of the particle being analyzed. The bed particles and the pivoting particle being analyzed are of a similar size, and thus the particle is assumed to be fully submerged. The submerged weight was taken as $W = k_1 D^3 (\rho_s - \rho_w) g$ which is suitable for sediment but does not account for the possibility of a boulder being subjected to relative flow depths less than 1. The equation is thus modified to explicitly account for the volume of water displaced

$$W = g(k_1 D^3 \rho_s - V_{disp} \rho_w) \quad (4\text{-}7)$$

Where k_1 is a proportionality constant for volume, in this case $\pi/6$ for a sphere. V_{disp} is the volume of water displaced and is a function of the flow depth.

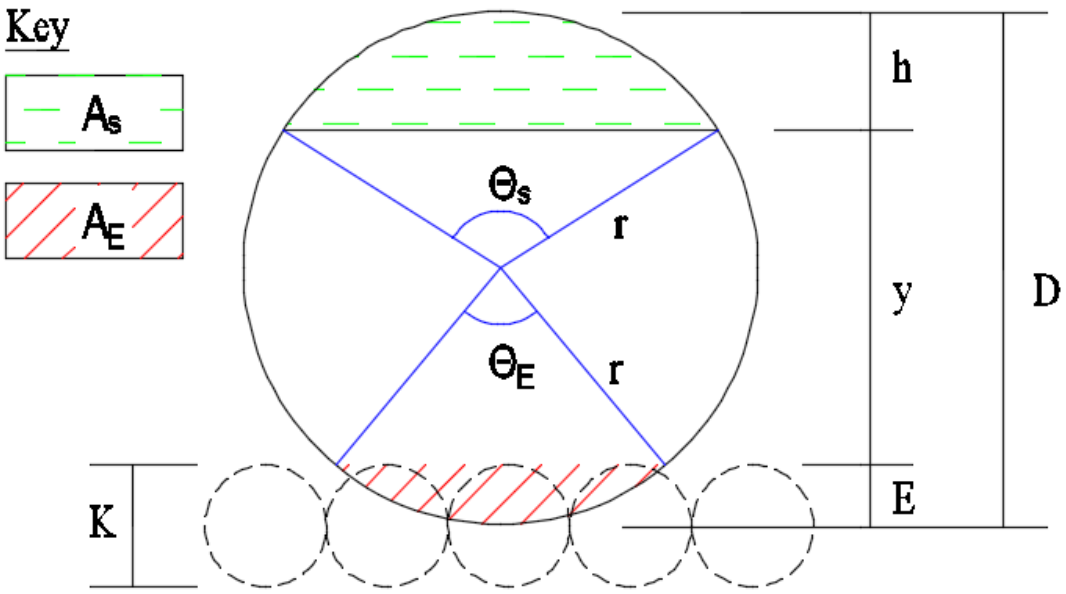


Figure 4-3: Schematic of boulder position for volume and area calculations.

Figure 4-3 shows the geometry of a spherical boulder resting on a bed of smaller particle. Here *y* is the flow depth above the top of the bed particles. When the boulder is fully submerged, $y > D\text{-}E$ and $h=0$ and the volume of water displaced is the same as the volume of the boulder. When the boulder is not fully submerged, the volume of water displaced is given by:

$$Vdisp = \frac{4\pi r^3}{3} - \frac{\pi h^2}{3}(3r - h)) \quad (4\text{-}8)$$

Where r is the boulder radius, and h is the height of the segment not exposed to flow given by:

$$h=D\text{-}E\text{-}y \quad (4\text{-}9)$$

4.2.4 Drag and Lift Forces

The drag and lift forces depicted in Figure 4-1 are calculated using Equations 4-10 and 4-11 respectively.

$$F_D = 0.5 C_D A_n \rho_w V^2 \quad (4\text{-}10)$$

$$F_L = 0.5 C_L A_p \rho_w V^2 \quad (4\text{-}11)$$

where C_D and C_L are the drag and lift coefficients respectively, A_n represents the area of the boulder exposed normal to flow, while A_p is the area exposed perpendicular to the flow, ρ_w is the density of water (in this case a constant at 1000kg/m^3), and V is the average velocity.

The drag coefficients used for the model were dependent on whether or not the boulder was embedded. For boulders that were not embedded, the results presented in Chapter 5.1 were incorporated into the model. For the boulders that were embedded, the drag coefficients were determined from Flammer et al. (1970).

When embedding the boulder, the effect is an object that is neither a full sphere nor a hemisphere. Flammer et al. (1970) presented results for drag coefficients compared to relative flow depths for hemispheres in a range of flow conditions (Figure 4-4). The Froude Number (Fr) for the experiments that involved embedded boulders ranged from 0.63-0.67 and appropriate drag coefficients are taken from Figure 4-4 and although these are only estimates, they do provide

better predictive results than the coefficients obtained in section 5.1 for embedded boulders.

The normal area exposed to flow, A_n, is a function of both the flow depth, y, and the level of embedment, E (see Figure 4-3). If the boulder is unsubmerged, the segment of the boulder that is above the water level, A_s, is calculated from Equation 4-12.

$$A_s = \frac{r^2}{2}(\theta_s - sin\,\theta_s) \tag{4-12}$$

$$\text{where } \theta_s = 2\,sin^{-1}\left(\frac{\sqrt{8h(r-0.5h)}}{2r}\right) \tag{4-13}$$

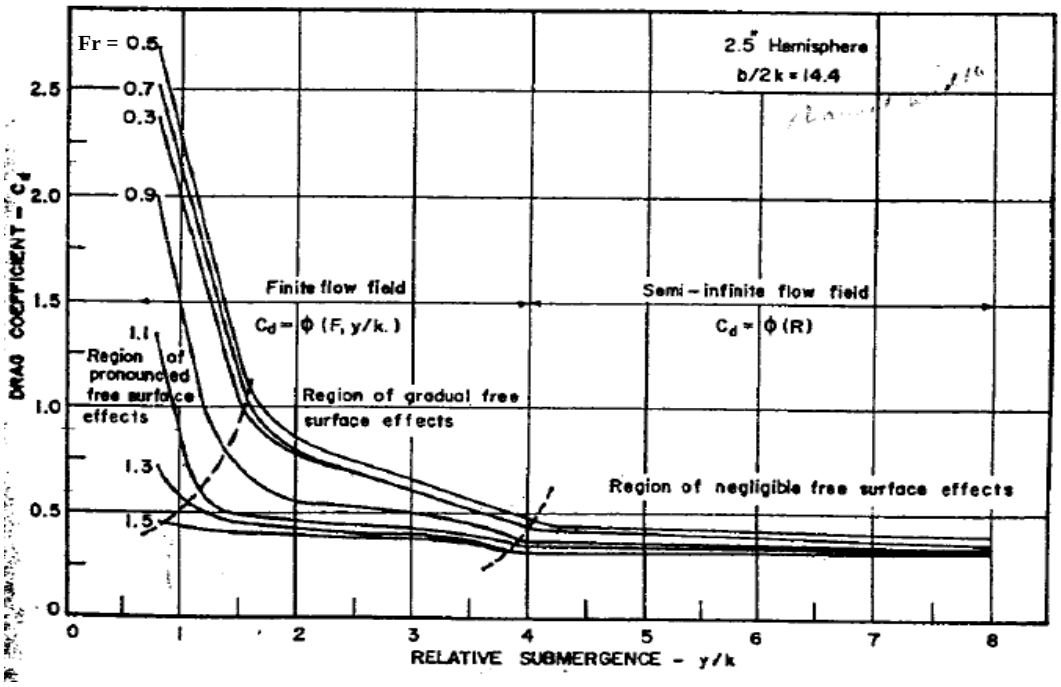


Figure 4-4: Relationship for relative submergence and drag coefficient for hemispheres (Flammer et al. 1970).

Note that relative submergence in Figure 4-4 is defined by y/K where K is the hemisphere diameter.

If the boulder is embedded, the area of the segment that is embedded, A_E, is calculated using Equation 4-14:

$$A_E = \frac{r^2}{2}(\theta_E - \sin\theta_E) \quad (4\text{-}14)$$

$$\text{where } \theta_E = 2\sin^{-1}\left(\frac{\sqrt{8E(r-0.5E)}}{2r}\right) \quad (4\text{-}15)$$

Equations 4-12 and 4-14 are identical in form but are distinguished from each other to prevent the wrong angle Θ from being used to calculate the areas of each segment. The normal area exposed to flow is then calculated as:

$$A_n = \frac{\pi D^2}{4} - A_s - A_E \quad (4\text{-}16)$$

Carling et al. (2002a) was used to determine the lift coefficient, bearing in mind that lift was only considered when the boulder was fully submerged.

$$C_L = 0.1\, C_D \quad for \frac{y}{D} > 1.0 \quad (4\text{-}17a)$$

$$C_L = 0 \quad for \frac{y}{D} < 1.0 \quad (4\text{-}17b)$$

Because the lift is only considered when the boulder is submerged, the perpendicular area exposed to flow is the full area of the boulder given by:

$$A_p = \frac{\pi D^2}{4} \quad (4\text{-}18)$$

4.2.5 Moment Lever Arm

The forces in Equation 4-1 are all applied some distance away from the pivot axis. These are given by *a*, *b*, and *c* for the weight, drag force, and lift force respectively (see Figure 4-5).

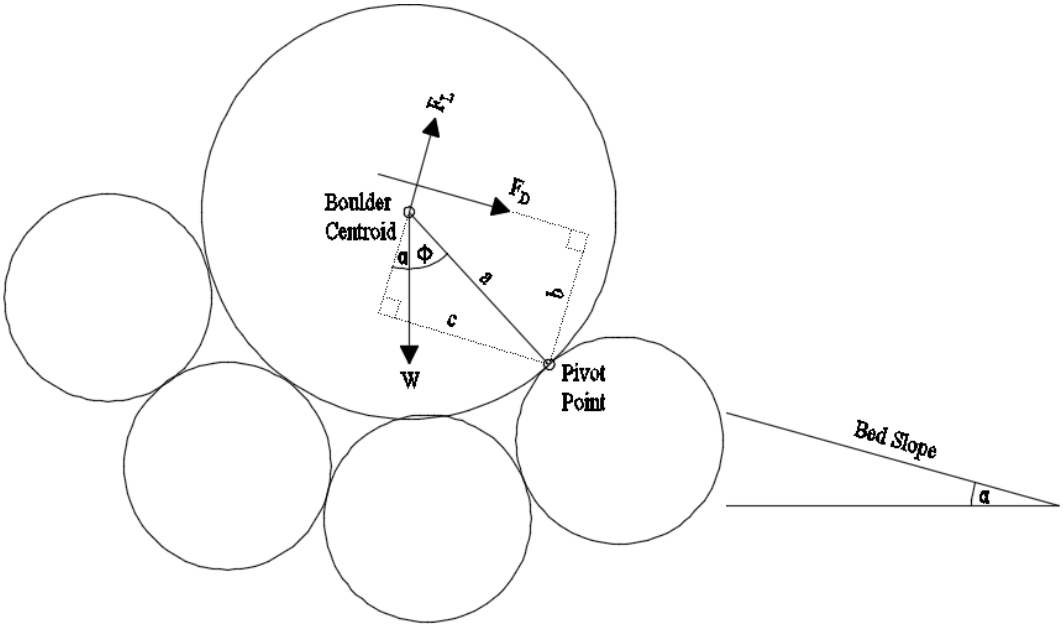


Figure 4-5: Moment lever arms a, b and c, about the pivot point.

Lever arm *a* is simply the distance between the boulder centroid and the pivot axis as calculated by Equations 4-5 and 4-6.

The drag force is assumed to act some distance above the boulder centroid but when applying this assumption, the flow depth needs careful consideration. This can only be true when the flow depth is greater than this assumed line of action for the drag force.

$$If\ y > k_3 D - E, then\ b = k_3 D \qquad (4\text{-}19a)$$

$$If\ y < k_3 D - E, then\ b = y \qquad (4\text{-}19b)$$

Where k_3 is a proportionality constant for the drag force lever arm given by James (1990):

$$k_3 = \frac{1}{D} \times \frac{\frac{D^4}{64} - \left(\frac{D^2}{8}A^2 - \frac{A^4}{4}\right)}{\frac{D^3}{12} - \left(\frac{D^2}{4}A - \frac{A^3}{3}\right)} \qquad (4\text{-}20)$$

For the case where the flow depth is below the theoretical line of action, the lever arm is assumed to be equal to the flow depth. This results in the line of action of the drag force assumed to be just below the surface of the water as the pivot point is below the top of the bed particles (see Figure 4-2) and the flow depth is measured from the top of the bed particles (see Figure 4-3). While this assumption is not strictly accurate, the case where this condition is applicable is for when the boulder is unsubmerged and the water level is approximately half of the boulder diameter. The free surface variability around the boulder at this point complicates the determination of the moment arm and needs further analysis in future research.

The lift force is assumed to act through the boulder centroid and therefore c is a function of a:

$$c = a(sin(\Phi + \alpha)) + k_4 D \qquad (4\text{-}21)$$

Where k_4 is a proportionality constant for the lift force lever arm, in this case $k_4 = 0$ as the lift force is assumed to act through the boulder centroid.

4.2.6 Subject of Manipulation

James (1990) needed some way to compare the results of his theoretical model with measured results from previous researchers. He decided to manipulate Equation 4-1 in such a way that he could compare his prediction to Shields parameter for naturally packed sediment, for which there are numerous experimental result. Aside from the results in Chapter 5, there are no other experiments involving spherical boulders that are larger than the bed material for which this model could be compared.

River hydraulics is a complex topic but in practice there are many simplifications that are made. The typical hydraulic characteristics that are used for design purposes are the flow rate, flow depth, and the average velocity. Drag and lift forces are both a function of velocity (Equations 4-10 and 4-11) and it is possible

to manipulate Equation 4-1 such that a dimensionless velocity is the subject of the formula.

4.2.7 Dimensionless Velocity Equation

Equation 4-1 can be manipulated to group the submerged weight of the boulder and the distance between the boulder centroid and pivot axis, resulting in:

$$Wa\ (cos(\alpha)\ \sin(\alpha+\phi) - sin(\alpha)\cos(\alpha+\phi) = F_D b + F_L c \quad (4\text{-}22)$$

The trigonometric term in the LHS of Equation 4-22 is a known trig relationship that can be reduced to:

$$Wa\ sin(\phi) = F_D b + F_L c \quad (4\text{-}23)$$

The drag and lift forces (Equation 4-10 and 4-11) are substituted in to give:

$$Wa\ sin(\phi) = 0.5 C_D A_n \rho_w V^2 b + 0.5 C_L A_p \rho_w V^2 c \quad (4\text{-}24)$$

The common terms are grouped resulting in:

$$Wa\ sin(\phi) = 0.5 \rho_w V^2 (C_D A_n b + C_L A_p c) \quad (4\text{-}25)$$

The velocity is then made the subject of the formula:

$$\rho_w V^2 = \frac{2Wa\ sin(\phi)}{(C_D A_n b + C_L A_p c)} \quad (4\text{-}26)$$

The submerged weight (Equation 4-7) and the boulder centroid pivot axis distance (Equation 4-5) are inserted to give:

$$\rho_w V^2 = \frac{2g(k_1 D^3 \rho_s - V_{disp}\rho_w) k_2 D\ sin(\phi)}{(C_D A_n b + C_L A_p c)} \quad (4\text{-}27)$$

Equation 4-27 is then rearranged to give Equation 4-28:

$$\frac{V^2}{\frac{D}{\rho_w}} = \frac{2g(k_1 D^3 \rho_s - V_{disp}\rho_w)k_2\ sin(\phi)}{\left(C_D A_n b + C_L A_p c\right)} \quad (4\text{-}28)$$

To reduce the velocity to a dimensionless form, the relative specific weight of the boulder needs to be introduced:

$$\frac{V^2}{\frac{D(\gamma_s - \gamma_w)}{\rho_w}} = \frac{2g(k_1 D^3 \rho_s - V_{disp}\rho_w)k_2\ sin(\phi)}{(\gamma_s - \gamma_w)\left(C_D A_n b + C_L A_p c\right)} \quad (4\text{-}29)$$

$$\frac{V^2}{\frac{D(\rho_s - \rho_w)g}{\rho_w}} = \frac{2(k_1 D^3 \rho_s - V_{disp}\rho_w)k_2\ sin(\phi)}{(\rho_s - \rho_w)\left(C_D A_n b + C_L A_p c\right)} \quad (4\text{-}30)$$

$$\frac{V^2}{D(S_s - 1)g} = \frac{2(k_1 D^3 \rho_s - V_{disp}\rho_w)k_2\ sin(\phi)}{(\rho_s - \rho_w)\left(C_D A_n b + C_L A_p c\right)} \quad (4\text{-}31)$$

The resulting equation is:

$$\frac{V}{\sqrt{D(S_s - 1)g}} = \sqrt{\frac{2(k_1 D^3 \rho_s - V_{disp}\rho_w)k_2\ sin(\phi)}{(\rho_s - \rho_w)\left(C_D A_n b + C_L A_p c\right)}} \quad (4\text{-}32)$$

For any boulder subjected to a flow of depth *y* and velocity *V*, if the LHS of Equation 4-32 equals the RHS, the boulder is at the incipient condition and the velocity, *V*, represents the critical velocity. If the LHS is less than the RHS, the boulder is under stable flow conditions, while if the LHS is greater than the RHS then the boulder is unstable for the given flow conditions.

4.3 Determining the Flow Depth and Appropriate Flow Velocity

When a boulder is placed in a channel, the physical variables (channel slope, bed particle size, depth of embedment, etc.) become fixed for the purpose of using Equation 4-32. The stability of the boulder is then affected by a given flow depth and flow velocity. In order for the model to be able to predict the critical flow depth and velocity for the experiments in Table 3-1, the relationship between the

flow depth and velocity needs to be consistent. This is accomplished by using the same roughness coefficient when calculating the velocity.

For each experimental run, a Manning's coefficient was calculated using Equation 4-33:

$$n = \frac{wy}{Q}\left(\frac{wy}{w+2y}\right)^{2/3}\sqrt{S_0} \qquad (4\text{-}33)$$

Where y is the flow depth, w is the flume width, Q is the flow rate, and S_0 is the flume slope.

The Manning's n for each experiment was then used to calculate a velocity for a user defined flow depth (Equation 4-34):

$$V = \frac{1}{n}\left(\frac{wy}{w+2y}\right)^{2/3}\sqrt{S} \qquad (4\text{-}34)$$

This process means that Equation 4-32 cannot be solved explicitly to find the critical flow conditions because the velocity is required in the drag and lift force calculations and the flow depth is required in the submerged weight and velocity calculation. An iterative solution is thus required to determine the critical flow depth such that the LHS and RHS of Equation 4-32 are equal.

5 RESULTS

For each of the experiments described in Chapter 3, a dimensionless relationship is presented and comparison against the model predictions is made. The stability of the boulders refers to the stabilizing moment about the pivot axis (LHS of Equation 4-1) where a higher stabilizing moment improves the stability. Conditions, be they flume (slope) or boulder (size, density, embedding) variations, that increase this stabilizing moment are said to improve the stability of the boulder.

5.1 Drag Coefficient Calibration

The drag coefficient experiments were aimed at providing indicative results for drag coefficients and results are less comprehensive than the incipient motion experiments.

5.1.1.1 Results

Table 5-1: Results of Drag Coefficient Experiments.

Exp.	Description	Embed	Flow Rate	Flow Depth	Drag Coefficient	Relative Depth	Adjusted Relative Depth	Reynolds Number
		mm	m^3/hr	mm	C_D	y/D	$y/(D-E)$	
1	80 - Q = 0.042m^3/s	0	147	78	0.81	0.98	0.98	1.54E+05
2	80 - Q = 0.033m^3/s	0	119	67	0.96	0.84	0.84	1.28E+05
3	80 - Q = 0.033m^3/s	0	119	78	0.82	0.97	0.97	1.25E+05
4	80 - Q = 0.027m^3/s	0	99	60	1.09	0.75	0.75	1.08E+05
5	80 - Q = 0.027m^3/s	0	99	66	0.97	0.82	0.82	1.06E+05
6	80 - Q = 0.027m^3/s	0	99	77	0.78	0.97	0.97	1.04E+05
7	80 - Q = 0.027m^3/s	0	99	108	0.64	1.35	1.35	9.84E+04
8	80 - Q = 0.027m^3/s	0	99	147	0.66	1.83	1.83	9.20E+04
9	80 embed - Q = 0.042m^3/s	8	151	79	0.53	0.99	1.10	1.59E+05
10	80 embed - Q = 0.042m^3/s	8	151	110	0.44	1.37	1.52	1.50E+05
11	120 - Q = 0.042m^3/s	0	157	78	1.11	0.65	0.65	1.65E+05
12	120 - Q = 0.042m^3/s	0	157	108	0.92	0.90	0.90	1.56E+05

5.1.1.2 Discussion

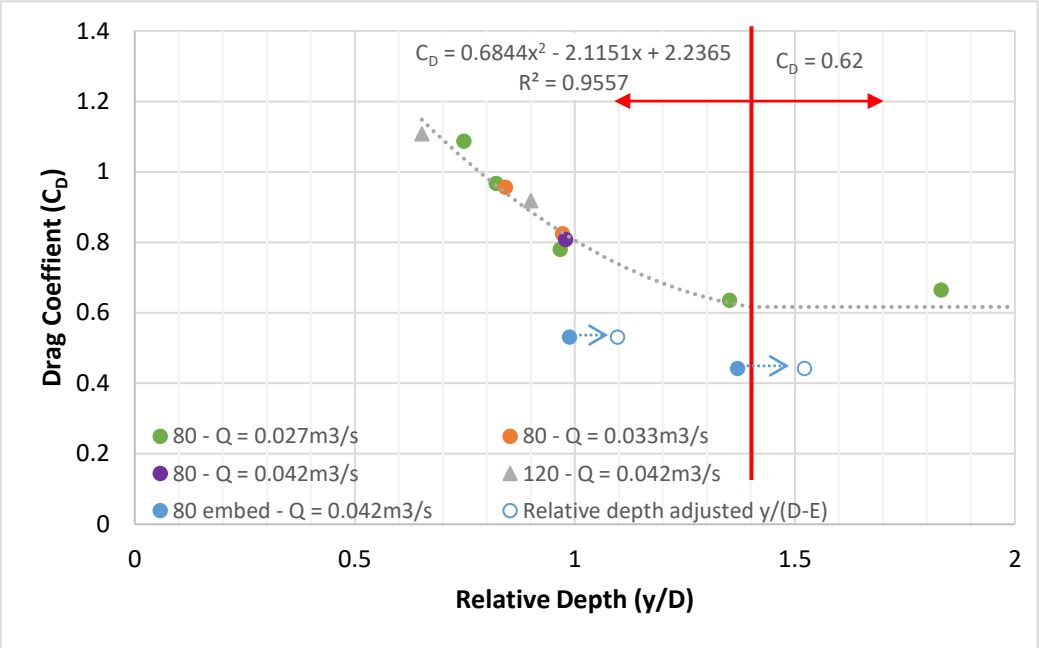


Figure 5-1: Relationship between relative flow depth and drag coefficient.

Figure 5-1 shows the results for all the drag coefficient experiments. The legend indicates the boulder size that was tested and the flow rate that the boulder was subject to.

For the non-embedded boulders, the drag coefficient decreases as relative depth increases which is expected as the boulder moves from an unsubmerged state to a submerged one where the free surface distortions begin to reduce and the ratio of the area of the boulder exposed to flow (A_n) to the flow area reduces. This is consistent with the trend identified by Flammer et al. (1970). The resulting drag coefficients are of an order of magnitude that is similar to that of spheres for Re=1x10^5, but also independent of Re for the range of flows tested.

The range of flow depths tested was limited by the flow rate and the slope of the flume being horizontal with the resulting Reynolds number for the drag coefficient calibration experiments ranging from 9.20x10^4 to 1.65x10^5 (see Figure 5-2). As such, the trend identified is only applicable for relative depths between 0.6 and 1.4 although the drag coefficient likely tends towards a constant for

greater relative depths. The regression line was only used to calculate the drag coefficients used in the model analysis for the non-embedded condition.

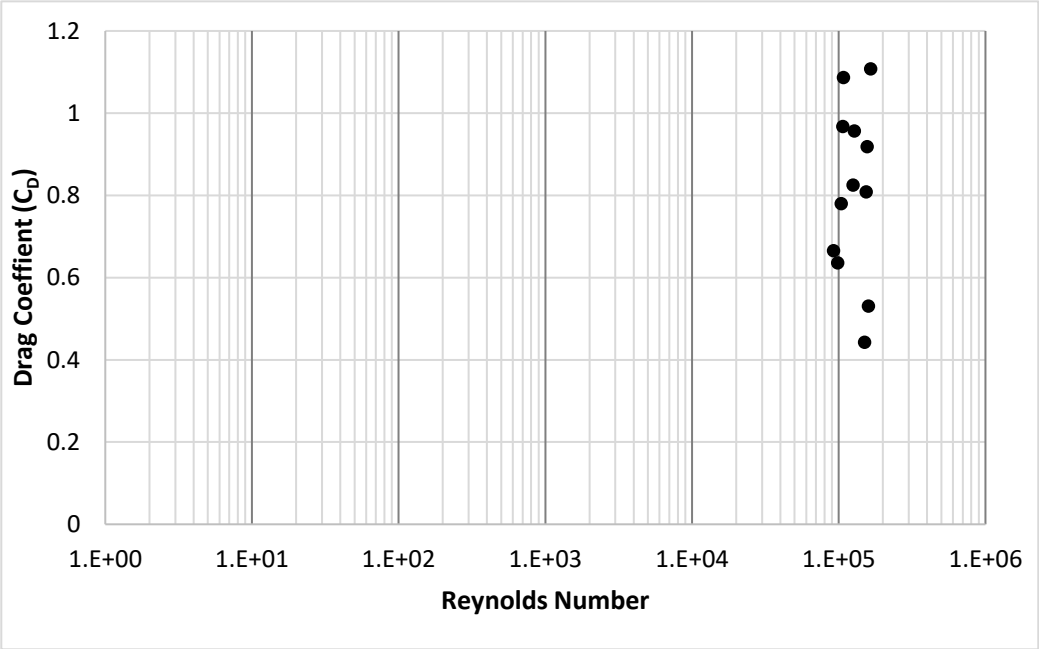


Figure 5-2: Reynolds Number versus Drag Coefficient.

The act of embedding a bolder exposed to a flow means that less of the boulder is exposed to the flow which theoretically means that the force acting on the boulder is reduced which is consistent with the results for the embedded boulder in Figure 5-1. Experiments 1 and 9 were used to compare the change in the drag coefficient for the embedded condition for a similar flow rate and flow depth. Because the same size boulder was used for each run, the relative depth (*y/D*) was the same when the depth of embedment is not accounted for. A relative embedment of 0.1 (8mm on an 80mm diameter boulder) reduced the drag coefficient from 0.81 to 0.53 (35% reduction). If the embedment were to be accounted for in the calculation of the relative flow depth, the result would be a translation of the data points, as shown in Figure 5-1.

When the drag coefficients for the embedded boulder were applied to the model the predictions for flow conditions were underestimates with errors in predicted dimensionless velocity ranging from 37% to 64%. Flammer et al. (1970) presented drag coefficients that were higher than the experimental results, ranging

between 1.83 and 2.34 for the range of relative depths. The Flammer et al. (1970) coefficients were applied to the model and gave a better correlation to the experimental results for incipient motion (see Figure 5-3 below) with predicted dimensionless velocity errors between 1%-14%.

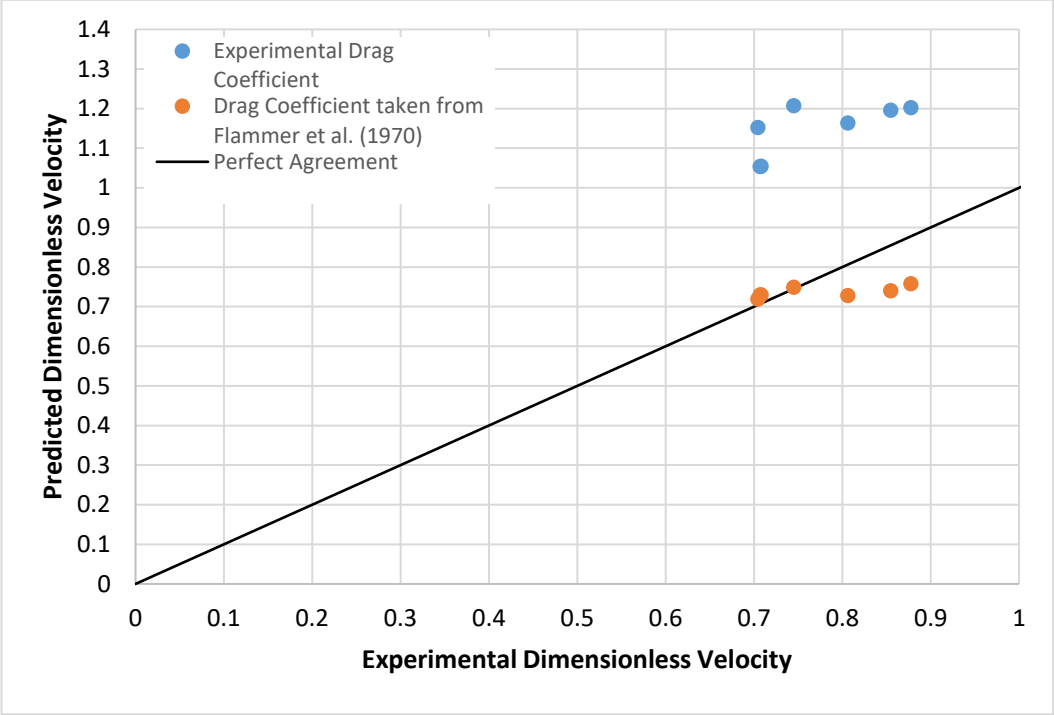


Figure 5-3: Comparison of predicted dimensionless velocity using experimental drag coefficients and drag coefficients taken from Flammer et al. (1970).

5.1.1.3 Conclusion

The drag experiments involving non-embedded boulders produced results that were incorporated into the model analysis. An increase in relative depth results in a reduction in the drag coefficient that likely tends towards a constant for relative depths larger than 2.

While the results of the non-embedded drag experiment produced good predictions when applied to the model, the embedded drag results did not. Flammer et al. (1970) drag coefficients were incorporated into the model as they gave better incipient motion predictions than the experimental drag results for embedded boulders.

5.2 Boulder Incipient Motion Experiments

A total of 47 experiments were carried out to investigate boulder stability (see Table 3-1), 41 of which yielded results that could be presented and modelled in chapter 4. The 6 that yielded no result (experiments 21, 25, 28, 30, 31, and 32) were each a different boulder that was embedded to a point where the maximum possible flume flow rate was not able to dislodge them. The 7th boulder was not tested to this point as the last level it was embedded at required a flow rate just below the maximum possible to dislodge it and embedding it any further would have yielded no result as well.

The relative depth of the experiments ranged from 0.47 to 1.14.

5.2.1 Effect of Relative Size

5.2.1.1 Note on Boulder Density

Ideally, the effect of size needs to be analyzed by testing boulders of different diameters that all have the same density. The easiest way to achieve this would be to test solid spheres made from the same material but in order to obtain results for these experiments, the boulders chosen needed to be suitable for the range of flow rates achievable in the flume.

The only solid spheres available in the range of diameters required were steel balls, which were too heavy. Hollow steel spheres were too light and floated in water but filling the hollow spheres with another material added the necessary weight without becoming too heavy. The material used to fill the spheres needed to be homogenous, so that the center of gravity of the boulder remained in the center, and light enough to keep the relative density low. Grain was used for 5 of the 7 boulders (boulders 80B and 80C were filled with plastic pellet and sand respectively to analyze the effect of density) as it allowed for bulk filling while keeping enough voids to keep the boulders less dense than the solid steel spheres but denser than water.

Hollow steel spheres were chosen because they were available in the 5 sizes required for the experiments. The consequence of choosing steel is that the uniform wall thickness for all the sizes complicated the goal of a uniform density. The ratio of volume of steel to total sphere volume is higher for the smaller spheres and thus when filled with the same material, the smaller spheres had a greater density (Table 5-2):

Table 5-2: Boulder Densities.

Boulder (mm)	Total mass (kg)	Density (kg/m^3)	Boulders with similar density
150	2.75	1,558	80B, 100, 120
120	1.52	1,682	80B, 100, 150
100	0.83	1,591	80B, 120, 150
80A	0.50	1,877	None
80B	0.44	1,645	100, 120, 150
80C	0.63	2,335	50
50	0.15	2,240	80C

5.2.1.2 Results

Table 5-3: Experimental and predicted results for relative size experiments.

Exp.	Boulder ID	*D/K*	Critical Dimensionless Velocity			Critical Average Velocity (m/s)			Critical Flow Depth (m)			Relative Flow Depth (*y/D*)	
			Exp.	Predicted	Absolute Error	Exp.	Predicted	Absolute Error	Exp.	Predicted	Absolute Error	Exp.	Predicted
1	50	2	0.603	0.508	16%	0.47	0.396	16%	0.057	0.043	25%	1.14	0.86
2	50	2	0.537	0.506	6%	0.419	0.395	6%	0.048	0.044	9%	0.96	0.87
35	50	2	0.537	0.506	6%	0.419	0.395	6%	0.048	0.044	9%	0.96	0.87
3	80A	3.2	0.544	0.529	3%	0.451	0.439	3%	0.052	0.05	4%	0.65	0.62
19	80A	3.2	0.523	0.516	1%	0.434	0.428	1%	0.053	0.052	2%	0.66	0.65
37	80A	3.2	0.512	0.510	0%	0.425	0.423	0%	0.053	0.053	0%	0.66	0.66
36	80B	3.2	0.568	0.557	2%	0.404	0.396	2%	0.051	0.049	3%	0.64	0.62
38	80C	3.2	0.431	0.451	5%	0.442	0.462	5%	0.059	0.064	8%	0.74	0.80
4	100	4	0.639	0.603	6%	0.487	0.460	6%	0.059	0.053	9%	0.59	0.53
20	100	4	0.629	0.593	6%	0.479	0.451	6%	0.060	0.054	10%	0.60	0.54
39	100	4	0.580	0.565	3%	0.442	0.43	3%	0.059	0.056	4%	0.59	0.56
5	120	4.8	0.590	0.565	4%	0.529	0.506	4%	0.067	0.062	7%	0.56	0.52
40	120	4.8	0.573	0.548	4%	0.514	0.491	4%	0.069	0.064	8%	0.58	0.53
6	150	6	0.610	0.607	1%	0.553	0.55	1%	0.071	0.07	1%	0.47	0.47
41	150	6	0.594	0.589	1%	0.538	0.534	1%	0.073	0.072	1%	0.49	0.48
				Max	16%		Max	16%		Max	25%	1.14	0.87
				Min	0%		Min	0%		Min	0%	0.47	0.47
				Average	4%		Average	4%		Average	7%		

5.2.1.3 Discussion

The constants for this experiment were the flume slope (0.00646) and the relative embedment (0). The variable was the size of the boulder being tested.

The 50mm boulder (*D/K*=2) was tested 3 times. The first two runs (Experiments 1 and 2) gave very different results and so it was repeated a third time (Experiment 35), with the third result identical to the second; the second and third tests required a lower velocity to dislodge the boulder. Figure 5-4 and Figure 5-5 show all three results for this boulder.

A similar situation occurred with the 100mm boulder and, again, all three results are shown, but for this case the first and second results (Experiments 4 and 20) required a higher velocity to dislodge the boulder and were almost identical. The data shown in the slope experiment (Figure 5-7) suggests that the results from the first and second run for this boulder are likely to be more accurate than the third result (Experiment 39).

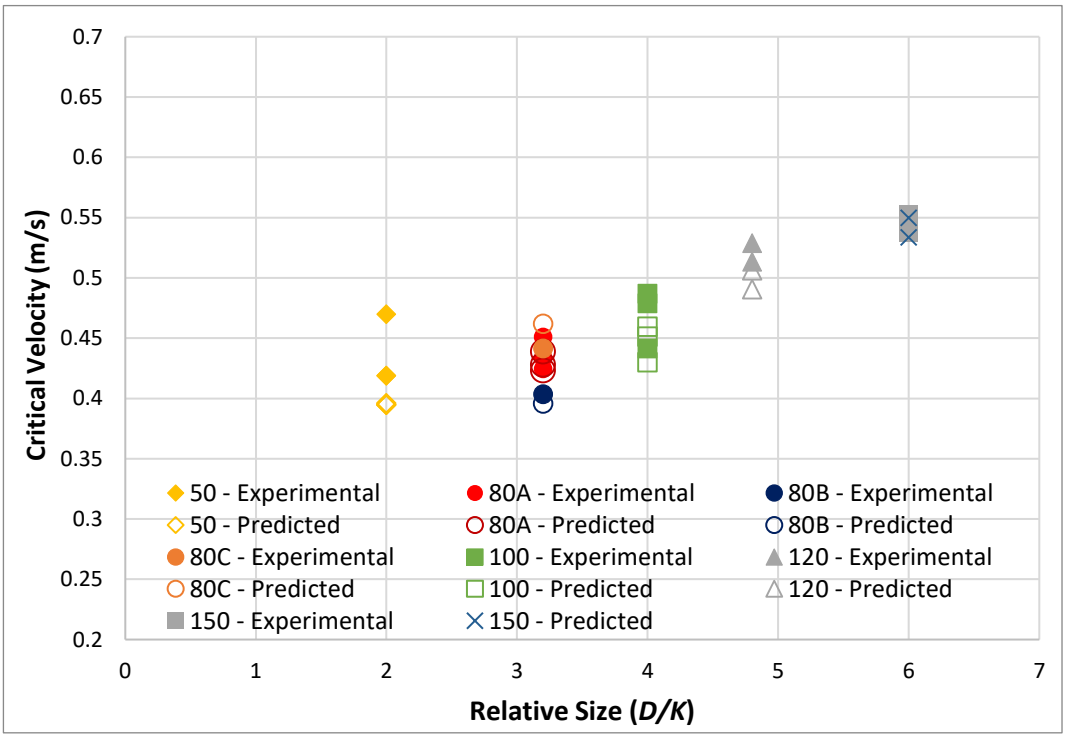


Figure 5-4:Relationship between relative size and critical average velocity.

Figure 5-4 shows that the average velocity required to induce motion tends to increase as the size of the boulder increases for the boulders of similar density

(*D/K* >3). This is expected because although the larger boulders have more area exposed to flow they also have a greater mass. For relative size *D/K* = 3.2, the denser the boulder the higher the required velocity to cause motion. The boulder for *D/K*=2, and boulder 80C for *D/K*=3.2 are of a similar density and show a similar trend for increasing *D/K*.

When the velocity is presented in dimensionless form (Figure 5-5), the trends are less pronounced than Figure 5-4. To determine the dimensionless velocity, the average velocity is divided by both the boulder size and the boulder's relative density. A bigger diameter suggests that the dimensionless velocity should get smaller for a constant relative density, but because the diameter is bigger, the weight of the boulder increases and thus the stabilizing moment also increases. A greater velocity is then required to induce incipient motion and this larger velocity is larger than the change in the diameter and thus the dimensionless velocity tends to increase with increasing boulder size.

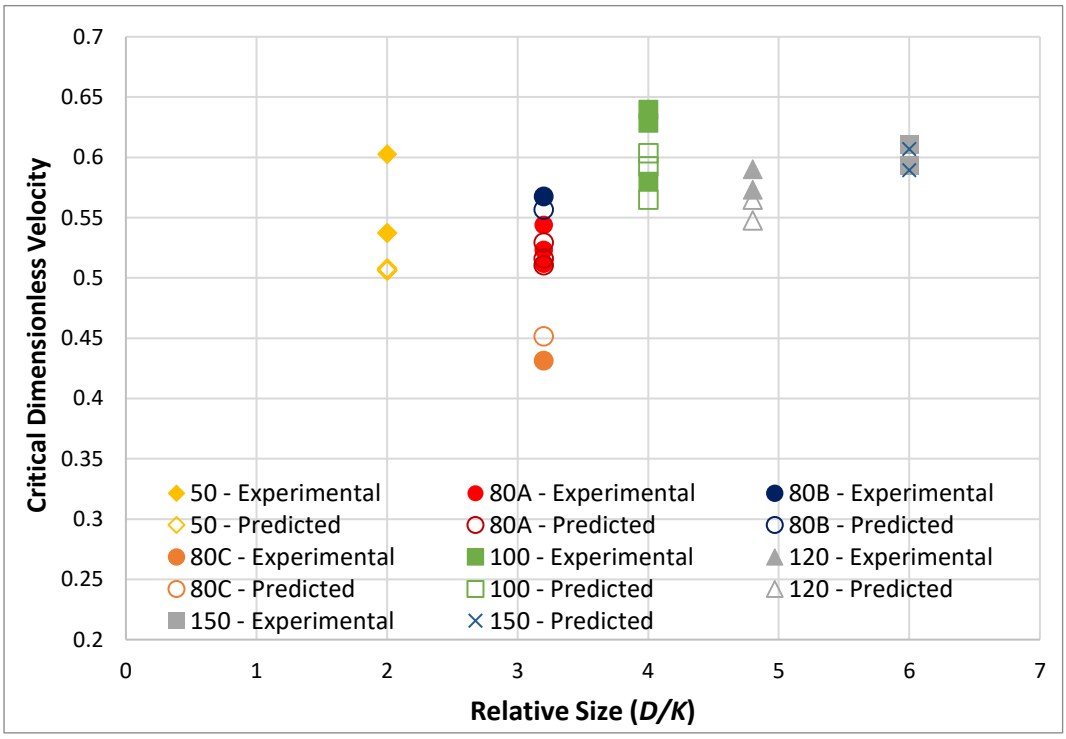


Figure 5-5: Relationship between relative size and critical dimensionless velocity.

If the dimensionless velocity for a theoretical set of conditions were to plot below the data in Figure 5-5, the boulder would be in a stable state while if the dimensionless velocity were to plot above the data then the boulder would be

unstable. Based on Figure 5-5, this indicates that the stability of a boulder increases with increasing relative size.

The relative flow depth tends to decrease (as shown in Figure 5-6) with increasing relative size, which is expected with the increase in velocity required as the size of the boulder increases.

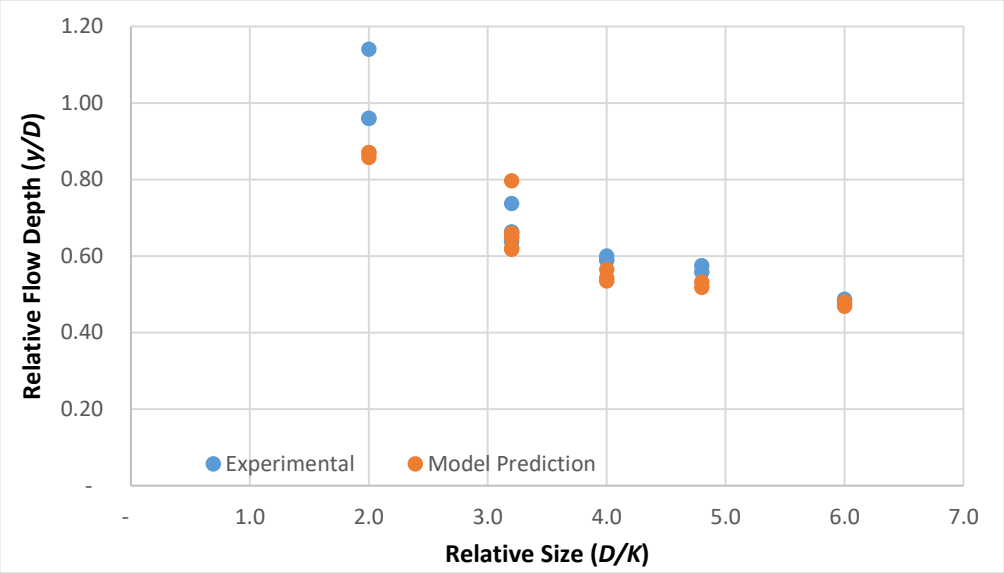


Figure 5-6: Relationship between relative boulder size and relative flow depth at incipient movement.

Table 5-3 shows the error between the experiments and the model predictions for the data shown in Figure 5-4 and Figure 5-5. It also provides the flow depth (y) and relative flow depth (y/D) comparison. The average absolute error in predicting the critical dimensionless velocity and the critical flow depth are 4% and 7% respectively.

5.2.1.4 Conclusion

The average experimental error shown in Table 5-3 and the identical trends between the experimental and model predicted velocities (Figure 5-4) suggest that the trends identified for relative boulder size and dimensionless velocity (Figure 5-5) are accurate and the model prediction is reasonable. There is a clear trend of critical velocity increasing for increasing boulder size and the increase in boulder size is associated with an increase in stability.

5.2.2 Effect of Slope

5.2.2.1 Results

Table 5-4: Experimental and predicted results for slope experiments.

Exp.	Boulder ID	Slope	Critical Dimensionless Velocity			Critical Average Velocity (m/s)			Critical Flow Depth (m)			Relative Flow Depth (y/D)	
			Exp.	Predicted	Absolute Error	Exp.	Predicted	Absolute Error	Exp.	Predicted	Absolute Error	Exp.	Predicted
12	100	0.0013	0.421	0.426	1%	0.321	0.325	1%	0.082	0.084	2%	0.82	0.84
10	100	0.0026	0.504	0.491	3%	0.384	0.374	3%	0.071	0.068	5%	0.71	0.68
14	100	0.0039	0.553	0.528	4%	0.421	0.402	4%	0.066	0.061	7%	0.66	0.61
8	100	0.0052	0.599	0.562	6%	0.456	0.428	6%	0.063	0.057	10%	0.63	0.57
16	100	0.0058	0.618	0.586	5%	0.471	0.446	5%	0.060	0.055	9%	0.60	0.55
4	100	0.0065	0.639	0.603	6%	0.487	0.460	6%	0.059	0.053	9%	0.59	0.53
20	100	0.0065	0.629	0.593	6%	0.479	0.451	6%	0.060	0.054	10%	0.60	0.54
39	100	0.0065	0.580	0.565	3%	0.442	0.430	3%	0.059	0.056	4%	0.59	0.56
18	100	0.0071	0.650	0.614	6%	0.495	0.468	6%	0.058	0.053	9%	0.58	0.53
11	80A	0.0013	0.419	0.439	5%	0.347	0.364	5%	0.070	0.076	9%	0.88	0.95
9	80A	0.0026	0.424	0.445	5%	0.352	0.369	5%	0.064	0.070	9%	0.80	0.87
13	80A	0.0039	0.470	0.474	1%	0.389	0.393	1%	0.059	0.060	2%	0.74	0.75
46	80A	0.0039	0.462	0.468	1%	0.383	0.388	1%	0.060	0.061	2%	0.75	0.77
7	80A	0.0052	0.495	0.494	0%	0.410	0.409	0%	0.056	0.056	0%	0.70	0.70
43	80A	0.0052	0.495	0.494	0%	0.410	0.409	0%	0.056	0.056	0%	0.70	0.70
15	80A	0.0058	0.504	0.501	1%	0.418	0.415	1%	0.055	0.054	1%	0.69	0.68
3	80A	0.0065	0.544	0.529	3%	0.451	0.439	3%	0.052	0.050	4%	0.65	0.62

Exp.	Boulder ID	Slope	Critical Dimensionless Velocity			Critical Average Velocity (m/s)			Critical Flow Depth (m)			Relative Flow Depth (y/D)	
			Exp.	Predicted	Absolute Error	Exp.	Predicted	Absolute Error	Exp.	Predicted	Absolute Error	Exp.	Predicted
19	80A	0.0065	0.523	0.516	1%	0.434	0.428	1%	0.053	0.052	2%	0.66	0.65
37	80A	0.0065	0.512	0.510	0%	0.425	0.423	0%	0.053	0.053	0%	0.66	0.66
17	80A	0.0071	0.543	0.532	2%	0.451	0.441	2%	0.051	0.049	3%	0.64	0.62
45	80B	0.0039	0.517	0.514	1%	0.368	0.365	1%	0.056	0.055	1%	0.70	0.69
42	80B	0.0052	0.546	0.538	1%	0.388	0.383	1%	0.053	0.052	2%	0.66	0.65
36	80B	0.0065	0.568	0.557	2%	0.404	0.396	2%	0.051	0.049	3%	0.64	0.62
47	80C	0.0039	0.410	0.439	7%	0.420	0.449	7%	0.065	0.073	12%	0.81	0.91
44	80C	0.0052	0.423	0.444	5%	0.433	0.455	5%	0.062	0.067	9%	0.78	0.84
38	80C	0.0065	0.431	0.451	5%	0.442	0.462	5%	0.059	0.064	8%	0.74	0.80
				Max	7%		Max	7%		Max	12%	0.88	0.95
				Min	0%		Min	0%		Min	0%	0.58	0.53
				Average	3%		Average	3%		Average	5%	0.69	0.69

5.2.2.2 Discussion

The constants for this experiment were the boulder size, density, and the boulders were not embedded, while the variable was the slope of the flume. The experiment was run for all three 80mm diameter boulders, although only boulder 80A was tested through the full range of slopes (0.0013 to 0.0071) while boulders 80B and 80C were tested for 3 slopes (0.0039, 0.0052, 0.0065). The 100mm boulder was also tested through the full range of slopes.

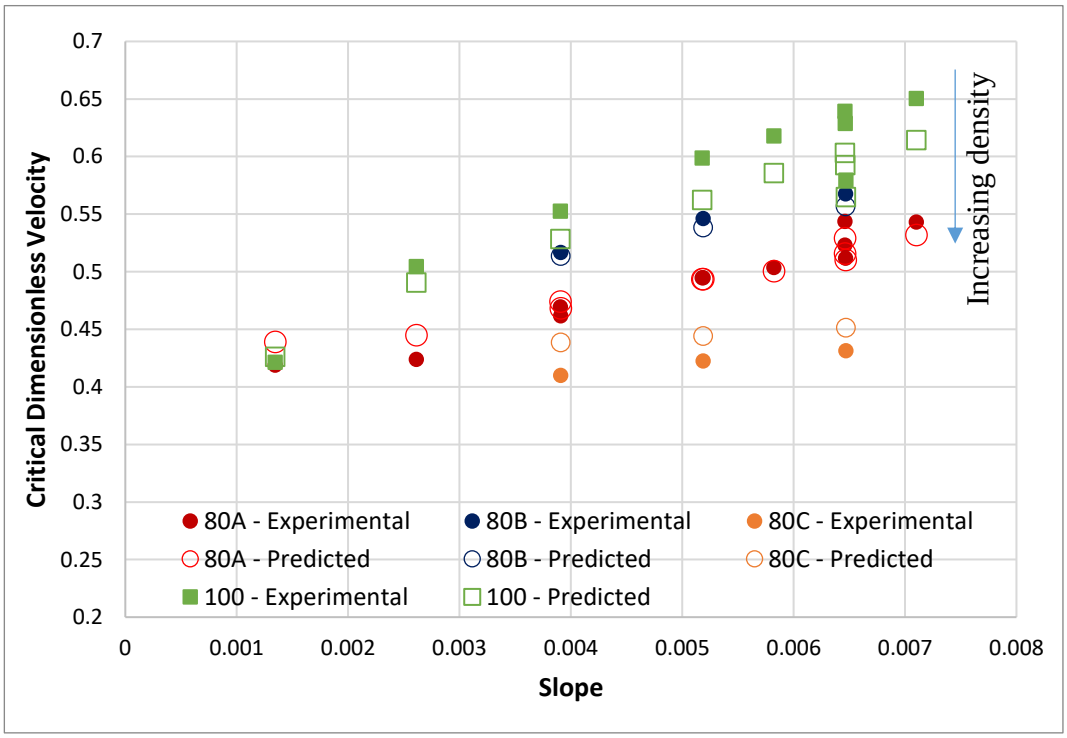


Figure 5-7: Relationship between slope and critical dimensionless velocity.

Figure 5-7 shows a clear trend where the critical dimensionless velocity increases with increasing slope. This is to be expected as the velocity is a function of the flow rate and the flow depth, where steeper slopes have lower flow depths compared to mild slopes with the same flow rate. The results for the different densities of the 80mm boulders are consistent with the results shown in Figure 5-11 where a greater relative density tends to a lower dimensionless velocity. The experimental result on the mildest slope (0.0013) for the 100mm boulder and boulder 80A are consistent with the results in Figure 5-5 in terms of the 100mm boulder having a higher dimensionless velocity than boulder 80A, but the model

prediction has this reversed. The data tends to converge for the milder slopes, suggesting closer inspection is required for milder slopes in future research.

Milder slopes with deeper flow depths, for a given flow, mean that more of a boulder will be submerged. This in turn means that the submerged weight of a boulder is reduced which reduces the stabilizing moment of the boulder about the pivot axis suggesting that the boulder is less stable for milder slopes. However, this is not the case as for a given flow the velocity is lower on milder slopes and thus the drag and lift forces are also reduced. The result of the higher velocity on steep slopes is that the dimensionless velocity increases but the stability decreases.

For a channel of fixed width and slope with an associated roughness, any change in flow rate results in a change in flow depth and flow velocity. If the flow rate and flow depth increase, the velocity will also increase and therefore the dimensionless velocity will also increase. If a dimensionless velocity were to plot above the data shown in Figure 5-7, a boulder would be unstable and the higher the flow rate for a given channel the more unstable it would be. Theoretically though, once a boulder is fully submerged the stabilizing moment ceases to decrease and the stabilizing moment therefore becomes constant. Carling et al. (2002a) theorize that lift only occurs after the boulder becomes fully submerged but the lift coefficient is in the order of 10% of the drag coefficient. This means that for a limited range of depths that are greater than the boulder diameter, the destabilizing moments will be at a maximum but thereafter the lift and drag forces will reduce with increasing depth and therefore any subsequent increase in flow depth should result in the boulder becoming more stable. This theory could not be tested because of the limitations of the flume and flow rate.

Figure 5-8 follows the same trends identified by Shvidchenko and Pender (2000) with the Shields parameter increasing for steeper slopes, while the trends obtained from the model predictions are also consistent with the experimental trends. The calculation is based on dividing the bed shear stress by the boulder diameter and not the bed particle diameter.

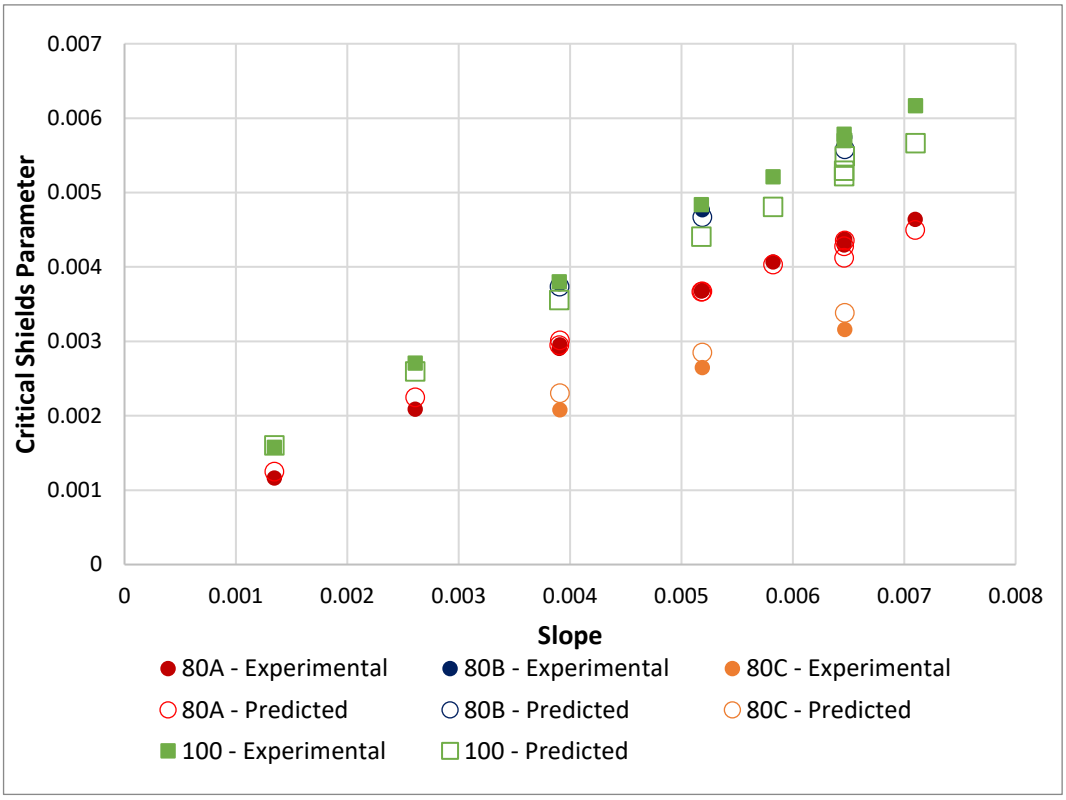


Figure 5-8: Relationship between slope and critical Shields parameter.

As expected, the relative flow depth at incipient motion tends to decrease with a steeper slope due to a higher velocity.

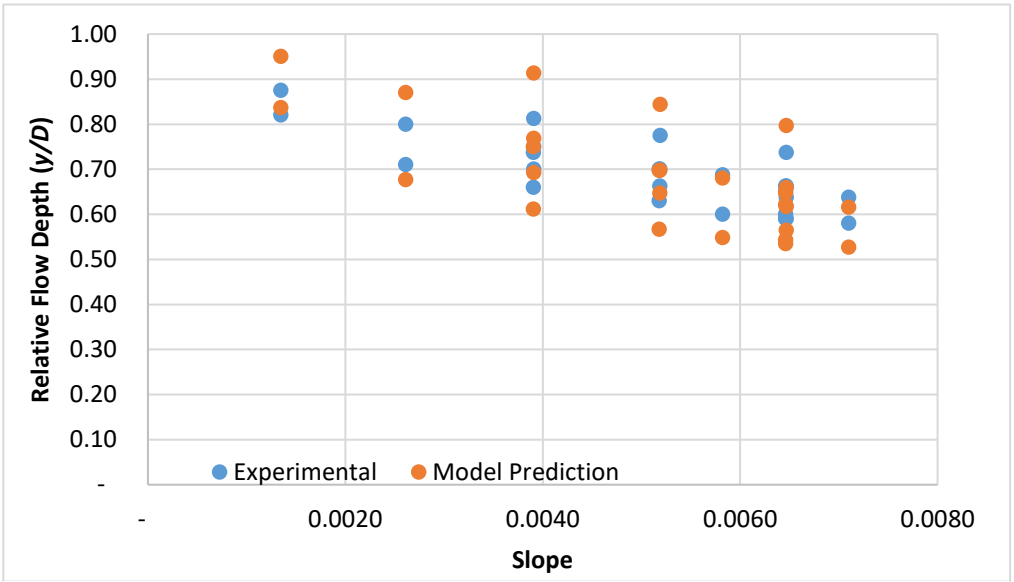


Figure 5-9: Relationship between slope and relative flow depth at incipient movement.

Table 5-4 shows that the average absolute errors between the experiments and the model predictions are 3% and 5% for the critical dimensionless velocity and the critical flow depth.

5.2.2.3 Conclusion

The experimental investigation yielded consistent results that are consistent with both the model and with theory for natural sediment where steeper slopes result in higher shear stress and dimensionless velocity but for a given flow rate, the steeper the slope the less stable the boulder.

5.2.3 Effect of Relative Density

5.2.3.1 Results

Table 5-5: Experimental and predicted results for relative density experiments.

Exp.	Boulder ID	Density (kg/m^3)	Slope	Critical Dimensionless Velocity			Critical Average Velocity (m/s)			Critical Flow Depth (m)			Relative Flow Depth (*y/D*)	
				Exp.	Predicted	Absolute Error	Exp.	Predicted	Absolute Error	Exp.	Predicted	Absolute Error	Exp.	Predicted
3	80A	1877	0.0065	0.544	0.529	3%	0.451	0.439	3%	0.052	0.050	4%	0.65	0.62
19	80A	1877	0.0065	0.523	0.516	1%	0.434	0.428	1%	0.053	0.052	2%	0.66	0.65
37	80A	1877	0.0065	0.512	0.510	0%	0.425	0.423	0%	0.053	0.053	0%	0.66	0.66
36	80B	1645	0.0065	0.568	0.557	2%	0.404	0.396	2%	0.051	0.049	3%	0.64	0.62
38	80C	2335	0.0065	0.431	0.451	5%	0.442	0.462	5%	0.059	0.064	8%	0.74	0.80
45	80B	1645	0.0039	0.517	0.514	1%	0.368	0.365	1%	0.056	0.055	1%	0.70	0.69
46	80A	1877	0.0039	0.462	0.468	1%	0.383	0.388	1%	0.060	0.061	2%	0.75	0.77
47	80C	2335	0.0039	0.410	0.439	7%	0.420	0.449	7%	0.065	0.073	12%	0.81	0.91
42	80B	1645	0.0052	0.546	0.538	1%	0.388	0.383	1%	0.053	0.052	2%	0.66	0.65
43	80A	1877	0.0052	0.495	0.494	0%	0.410	0.409	0%	0.056	0.056	0%	0.70	0.70
44	80C	2335	0.0052	0.423	0.444	5%	0.433	0.455	5%	0.062	0.067	9%	0.78	0.84
					Max	7%		Max	7%		Max	12%	0.81	0.91
					Min	0%		Min	0%		Min	0%	0.64	0.62
					Average	2%		Average	2%		Average	4%		

5.2.3.2 Discussion

For this experiment, the boulder size was kept constant (80mm diameter) and the boulders were not embedded. The slope was kept constant while testing each of the three 80mm boulders and then the experiment was run on another slope for each boulder. A total of 3 slopes were used to assess the effect of relative density (0.0039, 0.0052, and 0.0065)

The results in Figure 5-10 show that critical average velocity increases with increasing relative density with the same trend identified over a range of 3 slopes, while Figure 5-11 shows the opposite trend for dimensionless velocity. Both the relative density and the average velocity are used to calculate the dimensionless velocity with the average velocity being divided by the square root of the relative density (see Equation 4-32). Because of this, any change in relative density requires a proportional change in velocity for the dimensionless velocity to remain constant. Figure 5-10 suggests that increasing the relative density by approximately 40% results in an increase in the critical average velocity of only 10% which is less than the proportion required for a constant dimensionless velocity. As such, the results in Figure 5-11 are expected.

Unlike in Chapter 5.2.1, the change in density between boulders is desired. By keeping the boulder size the same, Figure 5-11 provides a clear linear relationship between density and dimensionless velocity. The higher the relative density the greater the weight of the boulder and thus the greater the stabilizing moment (Equation 4-1). This understanding, along with the trend in Figure 5-11, implies that when considering the relative density of the boulder, the lower the dimensionless velocity the greater the stability.

As with Figure 5-7, the steeper slopes have a higher critical dimensionless velocity.

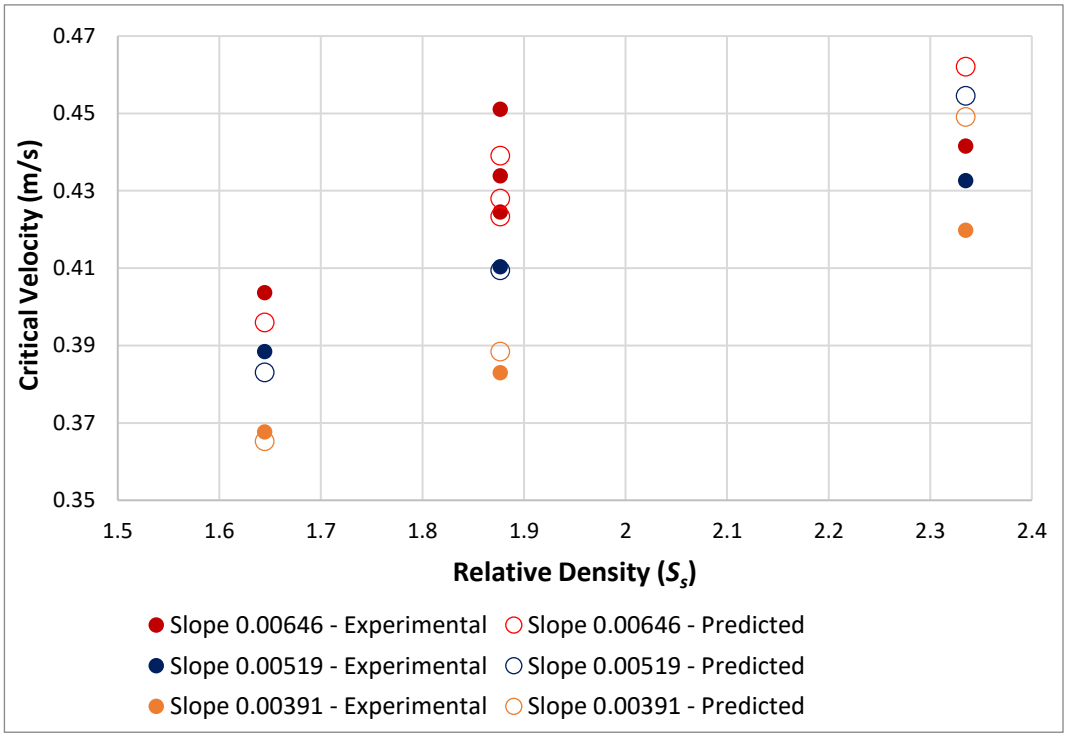


Figure 5-10: Relationship between relative density and critical average velocity.

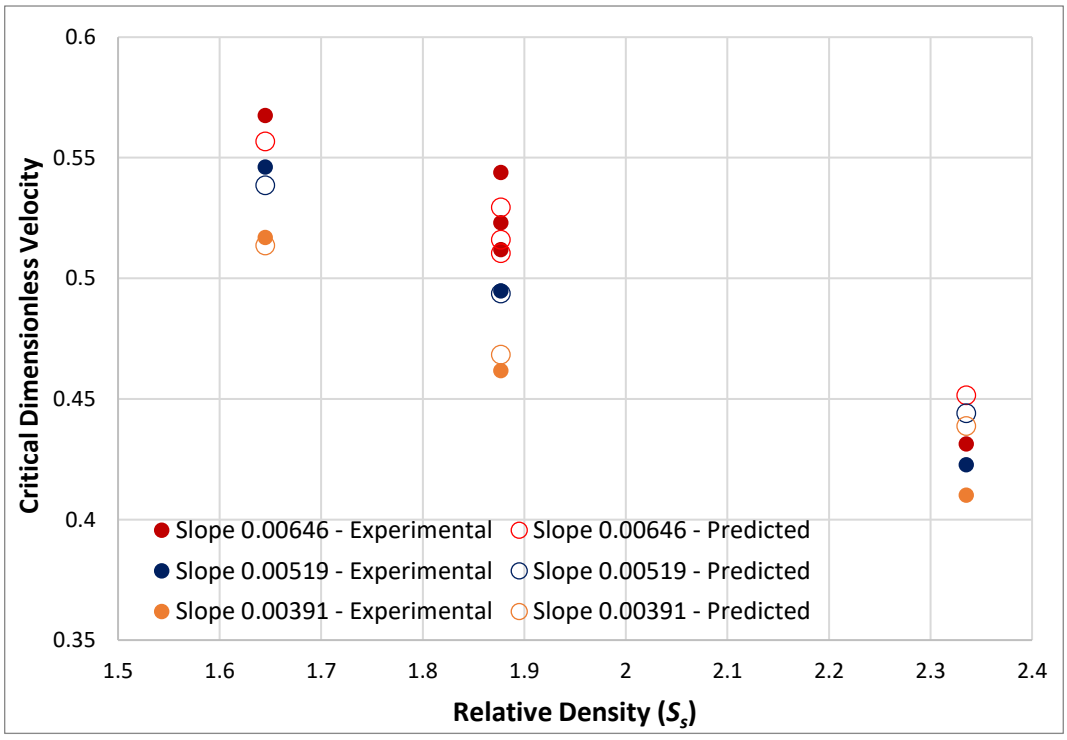


Figure 5-11: Relationship between relative density and critical dimensionless velocity.

Table 5-5 shows that the average absolute errors between the experiments and the model predictions are 2% and 4% for the critical dimensionless velocity and the critical flow depth.

5.2.3.3 Conclusion

The experiments produced consistent results that agreed with the model predictions. An increase in relative density increases the stability of the boulder when compared to a boulder of the same size but lower density, while the dimensionless velocity decreases.

5.2.4 Effect of Embedding

5.2.4.1 Results

Table 5-6: Experimental and predicted results for embedding experiments.

Exp.	Boulder ID	*E/D*	Critical Dimensionless Velocity			Critical Average Velocity (m/s)			Critical Flow Depth (m)			Relative Flow Depth (*y/(D-E)*)	
			Exp.	Predicted	Absolute Error	Exp.	Predicted	Absolute Error	Exp.	Predicted	Absolute Error	Exp.	Predicted
4	100	0.00	0.639	0.603	6%	0.487	0.460	6%	0.059	0.053	9%	0.59	0.53
23	100	0.06	0.745	0.750	1%	0.568	0.571	1%	0.077	0.078	1%	0.82	0.83
40	120	0.00	0.573	0.548	4%	0.514	0.491	4%	0.069	0.064	8%	0.58	0.53
24	120	0.05	0.678	0.732	8%	0.607	0.656	8%	0.086	0.099	15%	0.76	0.87
37	80A	0.00	0.512	0.510	0%	0.425	0.423	0%	0.053	0.053	0%	0.66	0.66
22	80A	0.08	0.708	0.703	1%	0.587	0.583	1%	0.081	0.080	1%	1.10	1.09
27	80A	0.08	0.707	0.702	1%	0.586	0.582	1%	0.081	0.080	1%	1.10	1.09
36	80B	0.00	0.568	0.557	2%	0.404	0.396	2%	0.051	0.049	3%	0.64	0.62
26	80B	0.08	0.704	0.720	2%	0.501	0.512	2%	0.065	0.068	4%	0.88	0.92
29	80B	0.10	0.806	0.726	10%	0.573	0.517	10%	0.081	0.068	17%	1.12	0.94
33	80B	0.12	0.855	0.749	12%	0.608	0.533	12%	0.085	0.068	21%	1.21	0.96
34	80B	0.14	0.878	0.753	14%	0.624	0.536	14%	0.089	0.068	24%	1.29	0.99
				Max	14%		Max	14%		Max	24%	1.29	1.09
				Min	1%		Min	1%		Min	1%	0.58	0.53
				Average	6%		Average	6%		Average	10%		

5.2.4.2 Discussion

The flume slope was kept constant (0.0065) and all seven boulders were tested for this experiment at various ratios of *E/D*. The flume bed material was manipulated so that the boulder could be embedded.

Figure 5-12 shows the relationship between embedding the particle and dimensionless velocity for four of the boulders used in the experiments. Boulders 50, 80C, and 150 could not be dislodged at the maximum flow rate, even for the smallest possible depth of embedding.

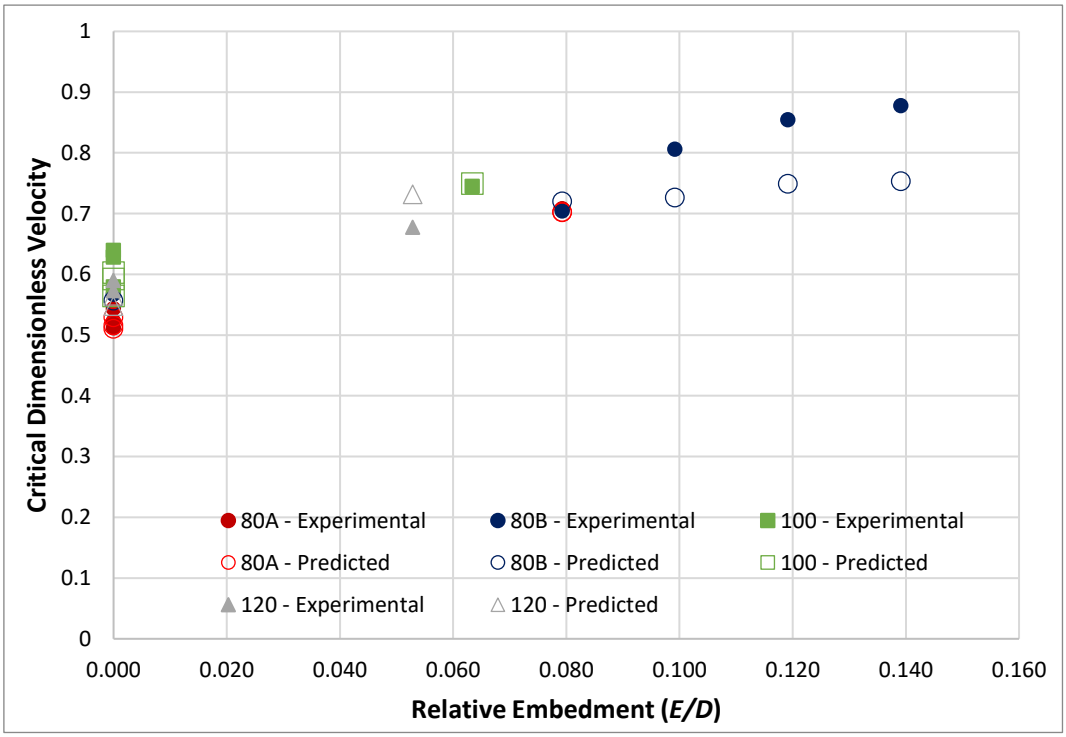


Figure 5-12: Relationship between relative embedment and critical dimensionless velocity.

The experimental results in Figure 5-12 and Figure 5-13 show an increase in the dimensionless velocity and average velocity required to cause incipient motion for increasing relative embedment. The model predictions for boulders 80A and 100 are similar while the experimental error increases for boulder 80B as the relative embedment increases (see Table 5-6).

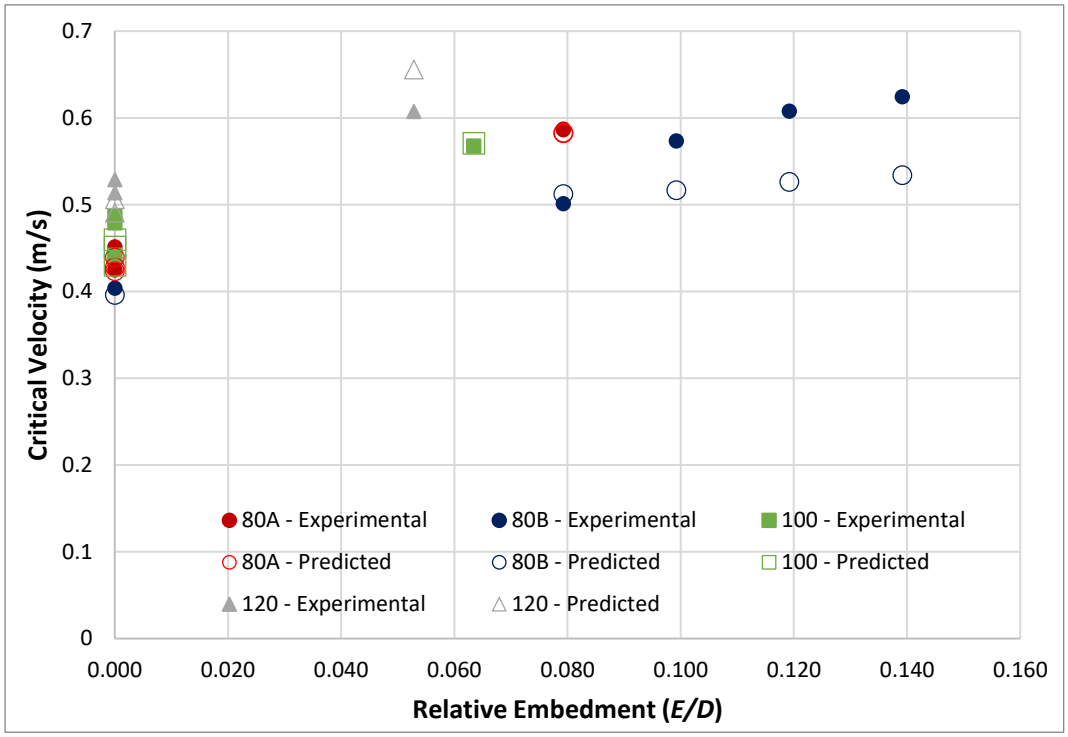


Figure 5-13: Relationship between relative embedment and critical average velocity.

In Figure 5-13, for a relative embedment of 0.08, the higher critical average velocity is expected for boulder 80A as it is denser than boulder 80B, however Figure 5-12 shows that the critical dimensionless velocity is almost the same. Comparing the data for these two boulders suggests that for the given change in densities and the embedment ratio, embedding the boulder is more effective in stabilizing the boulder than simply making it denser, but embedding the boulder and making it denser significantly improves the stability.

When embedding a boulder, the pivot angle is increased which means that the stabilizing moment for the boulder is increased, regardless of the flow rate. To dislodge the boulder from the embedded position, the submerged weight of the boulder needs to be reduced (i.e. increase the flow depth), and the destabilizing moments need to be increased (drag and lift forces).

In these experiments, the relative density and size of the boulder remain constant. This means that because the flow rate needs to increase to dislodge an embedded boulder, the dimensionless velocity also needs to increase which suggests that higher critical dimensionless velocities are more stable.

The depth of embedding was reduced a fixed distance for each embedding attempt meaning that, for example, although the depth of embedding may be the same for the 50mm boulder as the 120mm boulder, the relative embedment is greater for the 50mm boulder.

The combination of its total weight, relative density, and relative size compared to the bed material meant that boulder 80B was able to be embedded more than the other boulders. The trend displayed in Figure 5-12 for boulder 80B is only applicable to this boulder, although the shape of the trend would likely be similar for the other boulders. As incipient motion was only possible for one level of embedment for boulders 80A, 100, and 120, there is not enough information to form comprehensive relationships for them other than that their stability increases with increased embedment.

The model predictions identified similar trends to the experiments but because the drag coefficients were estimated from Flammer et al. (1970) for hemispheres, there is some intrinsic error. The model tends to provide more conservative estimations of the boulder stability.

The results are also consistent with the theory presented by Fenton and Abbott (1977) for protrusion, although their experiments were designed to show a decrease in stability as the bed particle was protruded more into the flow as opposed to this experiment showing an increase in boulder stability for effectively less protrusion.

Figure 5-14 shows that the relative depth (accounting for embedment) increases for increasing relative embedment.

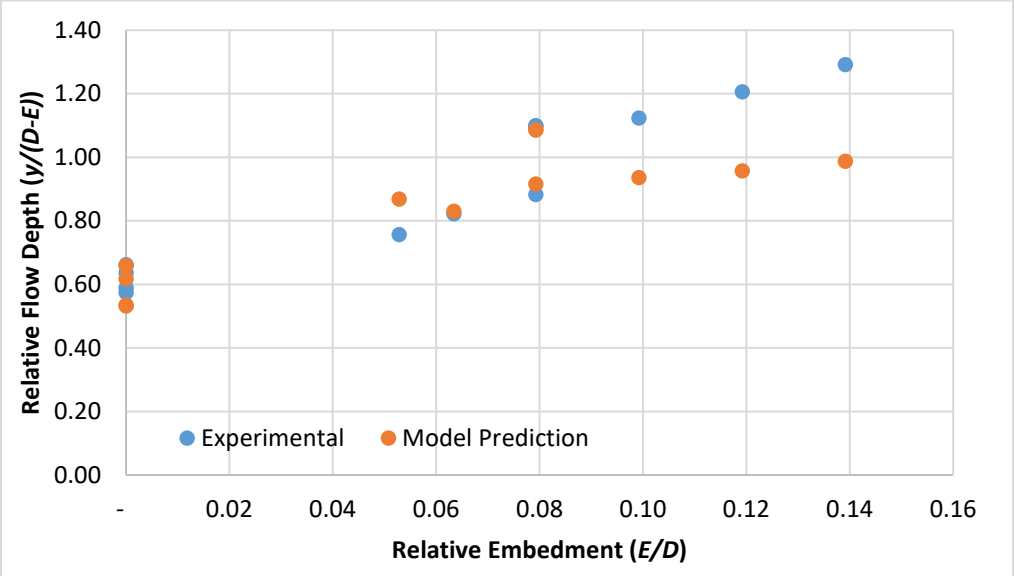


Figure 5-14: Relationship between relative embedment and relative flow depth at incipient movement.

The average absolute experimental error for the critical average velocity and the critical flow depth were 6% and 10% respectively but it should be noted that for boulder 80B the error tended to increase with increasing relative embedment.

5.2.4.3 Conclusion

The experimental investigation proved that embedding a boulder increases its stability. The relationship is such that the greater the relative embedment, the greater the dimensionless velocity and the greater the stability.

5.3 Application of Model

5.3.1 Moment Equilibrium- Equation 4-1

Because the incipient conditions for the boulders were recorded from physical experiments, the results (flow depth, average velocity) could be input into Equation 4-1 to verify that the basis of the model provides reasonable results. The LHS of Equation 4-1 represents the stabilizing moment while the RHS represents the destabilizing moment. The results in Figure 5-15 are distinguished between the embedded and non-embedded condition because of the different sources for drag coefficient.

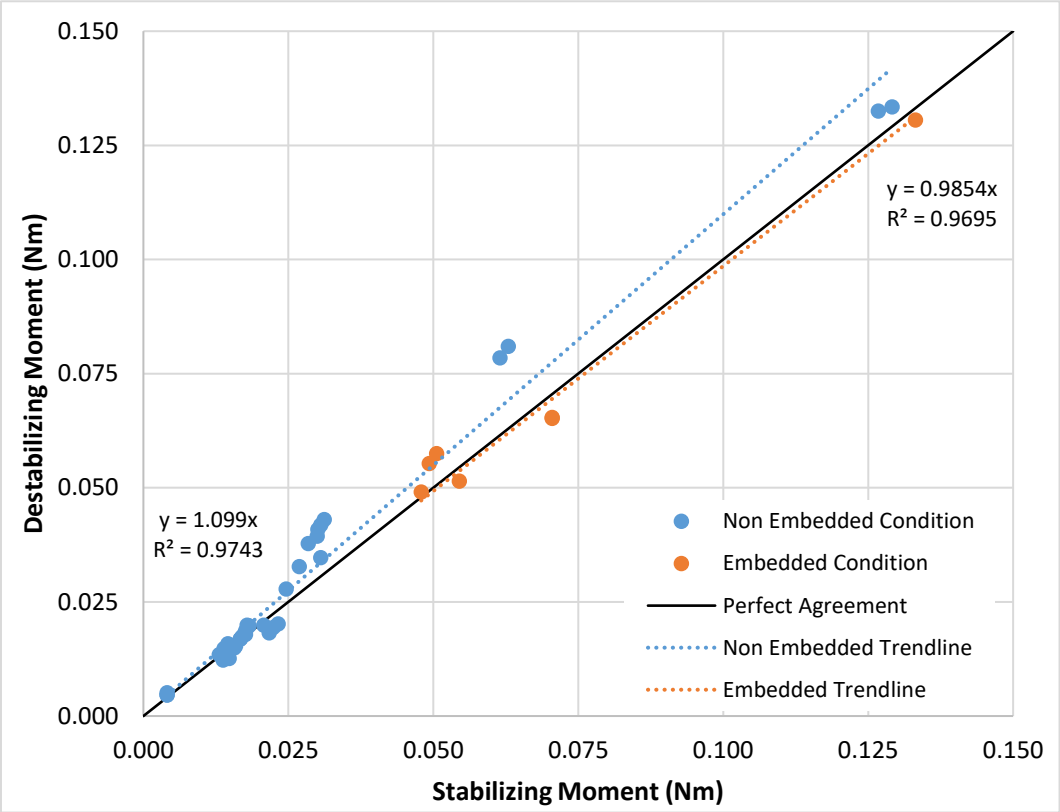


Figure 5-15: Relationship between stabilizing and destabilizing moments based on Equation (4-1) for boulder incipient motion experiments.

For the non-embedded condition, the stabilizing moments and destabilizing moments at incipient motion show a linear relationship with a gradient of 1.099, where a gradient of 1.0 relates to the moments balancing out perfectly. The higher gradient is expected as the flow conditions were recorded after the boulders had been dislodged and thus the destabilizing moments should be slightly greater than the stabilizing moments. The gradient of the trend line, suggests that the model is

accurate in predicting the stability of the boulders while the coefficient of determination ($R^2 = 0.9743$) implies that the model is consistent in its calculations.

The regression for the embedded condition indicates that the model is accurate ($R^2 = 0.9854$) but the gradient of the regression is less than 1.0 suggesting that the model is slightly over predicting the stability of the boulder. The drag coefficients are still not well established and there are also fewer data points to make the regression against and this needs to be considered when evaluating the results of any embedded boulder prediction.

Figure 5-15 shows that the stabilizing moments are generally higher for boulders that were embedded. The non-embedded boulder that had stabilizing forces greater than all, bar one, of the embedded boulders was the 150mm boulder which had the greatest mass (almost twice that of the 120mm boulder). The 120mm boulder had stabilizing forces in a similar magnitude to the embedded 80mm and 100mm boulders.

The review of the literature on the lift coefficient was consistent in suggesting that the lift was simply a fraction of the drag coefficient for shear Reynolds numbers higher than 150 but the fraction suggested ranged from 0.1 to 0.5. The shear Reynolds number for all of the experiments in this report ranged from 2260 to 9470 making this assumption for lift applicable. The ratio used was 0.1, as defined in Equation 4-17, but the lift was only considered when the boulder was submerged. This assumption on lift requires further research as the only boulder that was submerged was the 80B boulder when it was embedded and, as stated previously, the determination of the drag coefficient for the embedded boulder also needs further research.

5.3.2 Critical Dimensionless Velocity – Equation 4-32

Water flow conditions from the experiments were used to calculate an experimental dimensionless velocity which was then compared to the critical dimensionless velocity prediction for both the embedded and the non-embedded boulders shown Figure 5-16 and Table 5-7.

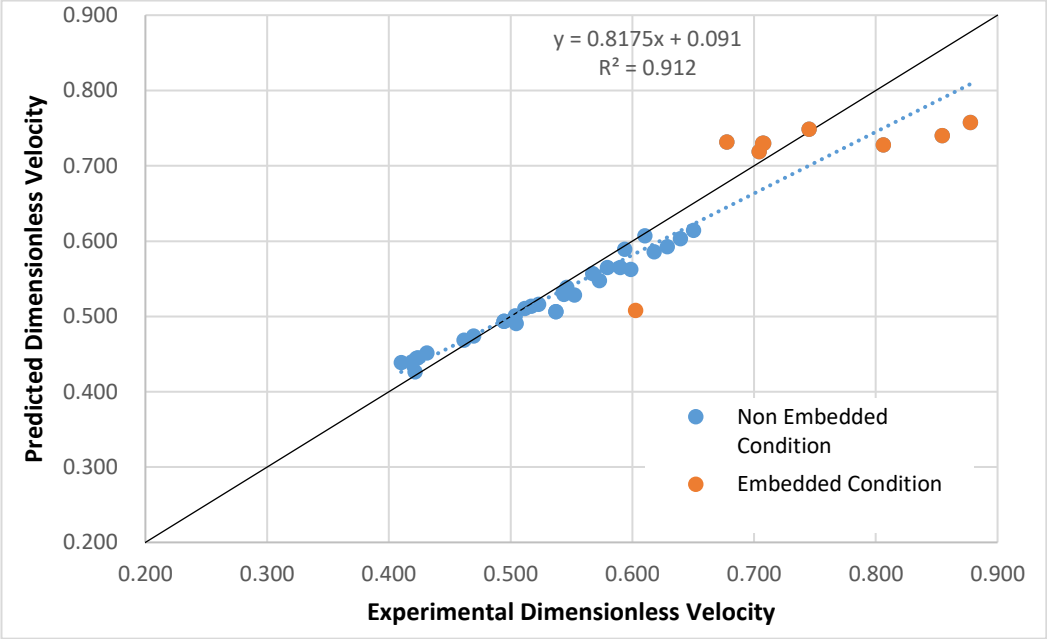


Figure 5-16: Comparison of experimental and predicted dimensionless velocities based on Equation 4-32.

The regression line presented in Figure 5-16 has a gradient less than 1 suggesting that for higher dimensionless velocities the model tends to predict conservative flow conditions for incipient motion and for lower dimensionless velocities the model tends to predict less conservative critical flow conditions.

The average absolute experimental error in predicting the critical dimensionless velocity for all the experiments was 4% and for the flow depth prediction the error was 7%.

Table 5-7: Experimental and predicted results for all boulders that pivoted out of position.

					Critical Dimensionless Velocity			Critical Average Velocity (m/s)			Critical Flow Depth (m)		
Exp.	Boulder ID	Density (kg/m^3)	Slope	Embed (m)	Exp.	Predicted	Absolute Error	Exp.	Predicted	Absolute Error	Exp.	Predicted	Absolute Error
1	50	2240	0.00645	0.000	0.603	0.508	16%	0.470	0.396	16%	0.057	0.043	25%
2	50	2240	0.00645	0.000	0.537	0.506	6%	0.419	0.395	6%	0.048	0.044	9%
3	80A	1877	0.00646	0.000	0.544	0.529	3%	0.451	0.439	3%	0.052	0.050	4%
4	100	1591	0.00646	0.000	0.639	0.603	6%	0.487	0.460	6%	0.059	0.053	9%
5	120	1682	0.00646	0.000	0.590	0.565	4%	0.529	0.506	4%	0.067	0.062	7%
6	150	1558	0.00646	0.000	0.610	0.607	1%	0.553	0.550	1%	0.071	0.070	1%
7	80A	1877	0.00518	0.000	0.495	0.494	0%	0.410	0.409	0%	0.056	0.056	0%
8	100	1591	0.00518	0.000	0.599	0.562	6%	0.456	0.428	6%	0.063	0.057	10%
9	80A	1877	0.00261	0.000	0.424	0.445	5%	0.352	0.369	5%	0.064	0.070	9%
10	100	1591	0.00261	0.000	0.504	0.491	3%	0.384	0.374	3%	0.071	0.068	5%
11	80A	1877	0.00134	0.000	0.419	0.439	5%	0.347	0.364	5%	0.070	0.076	9%
12	100	1591	0.00134	0.000	0.421	0.426	1%	0.321	0.325	1%	0.082	0.084	2%
13	80A	1877	0.00390	0.000	0.470	0.474	1%	0.389	0.393	1%	0.059	0.060	2%
14	100	1591	0.00390	0.000	0.553	0.528	4%	0.421	0.402	4%	0.066	0.061	7%
15	80A	1877	0.00582	0.000	0.504	0.501	1%	0.418	0.415	1%	0.055	0.054	1%
16	100	1591	0.00582	0.000	0.618	0.586	5%	0.471	0.446	5%	0.060	0.055	9%
17	80A	1877	0.00710	0.000	0.543	0.532	2%	0.451	0.441	2%	0.051	0.049	3%
18	100	1591	0.00710	0.000	0.650	0.614	6%	0.495	0.468	6%	0.058	0.053	9%
19	80A	1877	0.00646	0.000	0.523	0.516	1%	0.434	0.428	1%	0.053	0.052	2%
20	100	1591	0.00646	0.000	0.629	0.593	6%	0.479	0.451	6%	0.060	0.054	10%
22	80A	1877	0.00648	0.006	0.708	0.703	1%	0.587	0.583	1%	0.081	0.080	1%

					Critical Dimensionless Velocity			Critical Average Velocity (m/s)			Critical Flow Depth (m)		
Exp.	Boulder ID	Density (kg/m^3)	Slope	Embed (m)	Exp.	Predicted	Absolute Error	Exp.	Predicted	Absolute Error	Exp.	Predicted	Absolute Error
23	100	1591	0.00648	0.006	0.745	0.750	1%	0.568	0.571	1%	0.077	0.078	1%
24	120	1682	0.00648	0.006	0.678	0.732	8%	0.607	0.656	8%	0.086	0.099	15%
26	80B	1645	0.00646	0.006	0.704	0.720	2%	0.501	0.512	2%	0.065	0.068	4%
27	80A	1877	0.00646	0.006	0.707	0.702	1%	0.586	0.582	1%	0.081	0.080	1%
29	80B	1645	0.00647	0.008	0.806	0.726	10%	0.573	0.517	10%	0.081	0.068	17%
33	80B	1645	0.00647	0.010	0.855	0.749	12%	0.608	0.533	12%	0.085	0.068	21%
34	80B	1645	0.00647	0.011	0.878	0.753	14%	0.624	0.536	14%	0.089	0.068	24%
35	50	2240	0.00645	0.000	0.537	0.506	6%	0.419	0.395	6%	0.048	0.044	9%
36	80B	1645	0.00647	0.000	0.568	0.557	2%	0.404	0.396	2%	0.051	0.049	3%
37	80A	1877	0.00647	0.000	0.512	0.510	0%	0.425	0.423	0%	0.053	0.053	0%
38	80C	2335	0.00647	0.000	0.431	0.451	5%	0.442	0.462	5%	0.059	0.064	8%
39	100	1591	0.00647	0.000	0.580	0.565	3%	0.442	0.430	3%	0.059	0.056	4%
40	120	1682	0.00647	0.000	0.573	0.548	4%	0.514	0.491	4%	0.069	0.064	8%
41	150	1558	0.00647	0.000	0.594	0.589	1%	0.538	0.534	1%	0.073	0.072	1%
42	80B	1645	0.00519	0.000	0.546	0.538	1%	0.388	0.383	1%	0.053	0.052	2%
43	80A	1877	0.00519	0.000	0.495	0.494	0%	0.410	0.409	0%	0.056	0.056	0%
44	80C	2335	0.00519	0.000	0.423	0.444	5%	0.433	0.455	5%	0.062	0.067	9%
45	80B	1645	0.00391	0.000	0.517	0.514	1%	0.368	0.365	1%	0.056	0.055	1%
46	80A	1877	0.00391	0.000	0.462	0.468	1%	0.383	0.388	1%	0.060	0.061	2%
47	80C	2335	0.00391	0.000	0.410	0.439	7%	0.420	0.449	7%	0.065	0.073	12%
						Max	16%		Max	16%		Max	25%
						Min	0%		Min	0%		Min	0%
						Average	4%		Average	4%		Average	7%

6 CONCLUSIONS AND RECOMMENDATIONS

6.1 Drag Calibration Experiments

Figure 5-15 confirms that when the experimental drag coefficients are applied to Equation 4-1, the experimental data is at the incipient condition and thus the drag coefficient experiments for the non-embedded boulders are deemed suitable for use in the model.

The experimental procedure for measuring the drag force on the embedded boulders was flawed to the point that the data obtained was unusable, as shown in Figure 5-3. Another approach needs to be adopted in measuring the forces on an embedded boulder exposed to flow in future research but Flammer et al. (1970) produced results that were suitable for use in this model.

6.2 Boulder Incipient Motion Experiments

The experimental investigation for this report was not comprehensive enough to produce an empirical model for determining the stability of boulders in rivers but the results were used as a tool to verify the predictions of a theoretical model. While it was not possible to produce an empirical model, it was possible to identify trends from several factors affecting the stability of boulders:

- Although density was not kept constant when changing the size of the boulder being tested, the densities were similar enough for trends to be identified. Figure 5-4 and Figure 5-5 show that, as expected, the stability of a boulder increases with an increase in relative size. The results provided confirmation of the model predictions.
- The experimental results and the model predictions produced the same trends regarding slope and the stability of a boulder where the steeper the slope, the higher the critical dimensionless velocity but the lower the stability of a boulder.

- The denser a boulder is, the more stable it is under flow conditions, as indicated in Figure 5-10. The experimental results and the model predictions show the same trend where an increase in relative density results in a lower critical dimensionless velocity, as shown in Figure 5-11.
- Embedding a boulder into the bed material is the most effective way to improve the stability. Figure 5-13 shows that embedding boulder 80B was more effective in stabilizing the boulder than increasing the size to the 120mm boulder. The greater the boulder's relative embedment, the higher the dimensionless velocity, and the greater the stability.

6.3 Model Analysis

The model, based on a pivoting analysis, gives good predictions for incipient motion of boulders resting on a bed of smaller sized particles. The model provided consistent agreement with experimental results producing an average absolute experimental error of 4% when predicting the critical dimensionless velocity.

The determination of a drag coefficient is required for the model and a consistent relationship was found, experimentally, between C_D and relative depth for high Re for non-embedded boulders. For embedded boulders, the results from Flammer et al. (1970) gave good results

It needs to be remembered that the flow conditions (flow depth and average velocity) are dependent on the roughness of a water conveying structure and the model's predicted flow conditions need to be made with the same roughness in mind.

6.4 Recommendations for Further Research

- The experimental results and the stability model are limited to the conditions tested in an idealized laboratory setup. For wider application, experimental and actual data need to be collected and input into the model to assess any shortfalls.

- The boulders were placed on ideal bed material that did not get entrained before the boulder dislodged. Future research could involve testing the boulders on bed material that is significantly smaller to assess how the boulder reacts when the particles around it are moving.
- The experiments were limited by the flow rate for the flume. Further experiments could be run to assess the stability for deeper/submerged flows. The drag coefficient could be analyzed for a wider range of flow depths as well.
- The flows in this investigation were kept steady and uniform. Further research could be done to evaluate the stability of boulders for non-uniform conditions and whether the use of average velocity in the calculations makes the flow classification irrelevant. Exposing a boulder to surge waves could also be investigated.
- A revised approach needs to be made for measuring the drag forces on an embedded boulder.
- These experiments were run for boulders in isolation. Having a configuration of boulders could affect the effectiveness of this model and needs future consideration.

7 REFERENCES

Bathurst, J C, W H Graf, and H H Cao. 1987. "Bed load discharge equations for steep mountain rivers." In *Sediment Transport in Gravel-Bed Rivers*, edited by C R Thorne, J C Bathurst and R D Hey, 453-477. New York: John Wiley.

Bernard, J M, and R W Tuttle. 1998. "Stream Corridor Restoration: Principles, Processes, and Practices." *Engineering Approaches to Ecosystem Restoration.* 320-325.

Brahms, A. 1767. *Anfangsgründe der Deich und Wasserbaukunst.* Aurich Provincial Library Fryslan, Germany (in German): Herausgegeben vom Marschenrat bei Schuster in Leer.

Carling, PA, M Hoffmann, AS Blatter, and A Dittrich. 2002a. "Drag of emergent and submerged rectangular obstacles in turbulent flow above bedrock surface." In *Rock Scour due to Falling High-velocity Jets*, by AJ Schleiss and E Bollaert, 83-94. Lisse: Swets and Zeitlinger.

Carling, P A, M Hoffmann, and A S Blatter. 2002b. "Initial Motion of Boulders in Bedrock Channels." In *Ancient Floods, Modern Hazards: Principles and Applications of Paleoflood Hydrology, Volume 5*, edited by P. Kyle House, Robert H Webb, Victor R Baker and Daniel R Levish, 147-160. Washington, D. C.: American Geophysical Union.

Church, M. 1978. "Paleohydrological reconstruction from a Holocene valley fill." In *Fluvial Sedimentology, Canadian Society of Petroleum Geologists, Memoir 5*, edited by Andrew Miall, 743-772.

Dermisis, D C, and A N Papanicolaou. 2008. "Restoration of Gravel Bed Rivers via the Use of Stone Clasts (Rocks)." *World Environmental and Water Resources Congress.* Ahupua'a.

Fenton, J D, and J E Abbott. 1977. "Initial Movement of Grains on a Stream Bed: the Effect of Relative Protrusion." *Royal Society of London Ser A* 352: 523-537.

Fischenich, C, and R Seal. 1999. *Boulder Clusters.* EMRRP Technical Notes Collection (ERDC TN-EMRRP-SR-11), U S Army Engineer Research and Development Centre, Vicksburg, MS.

Flammer, G H, J P Tullis, and E S Mason. 1970. "Free Surface, Velocity Gradient Flow Past Hemisphere." *Journal of the Hydraulics Division* (ASCE 96(HY7)) 1485-1052.

Gögüs, M, and Z Defne. 2005. "Effect of Shape on Incipient Motion of Large Solitary Particles." *Journal of Hydraulic Engineering* 131 (1): 38-45.

Graf, W H, and L Suszka. 1987. "Sediment transport in steep channels." *Journal of Hydroscience and Hydraulic Engineering* (JSCE) 5 (1): 11-26.

Hamuy-Blanco, A. 2013. *Enhancement of habitat heterogeneity by placement of boulders in streams.* MSc Thesis, University of the Witwatersrand.

Helley, E J. 1969. *Field Measurement of the Initiation of Large Bed Particle Motion in Blue Creek Near Klamath, California.* United States Geological Survey.

Hendry, K, D Cragg-Hine, M O'Grady, and A Stephen. 2003. "Management of Habitat for Rehabilitation and Enhancement of Salmonid Stocks." *Fisheries Research* 62 (2): 171-192.

Hjulström, F. 1935. "The Morphological Activity of Rivers as Illustrated by River Fyris." *Bulletin of the Geological Institute of Uppsala* 25.

Hoffmans, G. 2010. "Stability of stones under uniform flow." *Journal of Hydraulic Engineering* 136 (2): 129-136.

Jackson, K S. 2016. "The determination of form drag coefficient for rigid, emergent objects in open channel flow." MSc Research Report, University of the Witwatersrand.

James, C S. 1990. "Prediction of entrainment conditions for nonuniform noncohesive sediments." *Journal of Hydraulic Research* 28 (1): 25-41.

James, C. 2015. "Scour Protection." *CIVN7016 Hydraulic Structures.* School of Civil and Environmental Engineering, University of the Witwatersrand.

Jeffreys, H. 1929. "Transportation of Sediment by Streams,." *Proceedings of the Cambridge Philosophical Society Vol 25.* Cambridge: Cambridge University Press. 272-276.

Lavelle, JW, and HO Mofjeld. 1987. "Do critical stresses for incipient motion and erosion really exist?" *Journal of Hydraulic Engineering* 113: 370-385.

Li, Z, and P D Komar. 1986. "Laboratory measurements of pivoting angles for applications to selective entrainment of gravel in a current." *Sedimentology* 33 (3): 413-423.

Ling, C. 1995. "Criteria for incipient motion of spherical particles." *Journal of Hydraulic Engineering* 121 (6): 472-478.

Marsh, N, A Western, and R Grayson. 2004. "Comparison of Methods for Predicting Incipient Motion for Sand Beds." *Journal of Hydraulic Engineering* 130 (7): 616-621.

Merz, J E. 2001. "Association of fall-run chinook salmon redds with woody debris in the Lower Mokelumne River, California." *California Fish and Game* 87 (2): 51-60.

Motamedi, A, H Afzalimehr, and V P Singh. 2010. "Evaluation of a novel approach to determine the critical shields stress." *Journal of Hydrologic Engineering* 15 (11): 892-900.

Pagliara, S, and P Chiavaccini. 2006. "Flow Resistance of Rock Chutes with Protruding Boulders." *Journal of Hydraulic Engineering* 132 (6): 545-552.

Paintal, AS. 1971. "Concept of critical shear stress in loose boundary open channels." *Journal of Hydraulic Research* 9: 91-113.

Prakash, H M. 2010. "Velocity approach for incipient motion." *ISH Journal of Hydraulic Engineering* 16 (2): 47-58.

Pretty, JL, SSC Harrison, DJ Shepherd, C Smith, AG Hildrew, and RD Hey. 2003. "River rehabilitation and fish populations: assessing the benefit of instream structures." *Journal of Applied Ecology* 40 (2): 251-265.

Rao, A R. 2004. "Incipient motion of hypothetical stream beds- Part 2_ Critical Shear Approach." *ISH Journal of Hydraulic Engineering* 10 (2): 94-105.

Shields, A. 1936. "Application of similarity principles and turbulence research to bed-load movement"." *Mitteilungen der Preußischen Versuchsanstalt für Wasserbau und Schiffbau* 26: 5-24.

Shvidchenko, AB, and G Pender. 2000. "Flume study of the effect of relative depth on the incipient motion of coarse uniform sediments." *Water Resources Research* 36 (2): 619-628.

Shvidchenko, A B, G Pender, and T B Hoey. 2001. "Critical shear stress for incipient motion of sand/gravel streambeds." *Water Resources Research* 37 (8): 2273-2283.

Taylor, BD, and VA Vanoni. 1972. "Temperature effects in low transport, flat bed flows." *Journal of Hydraulics Division* 98 (8): 1427-1445.

Thorne, C R, and L W Zevenbergen. 1985. "Estimating Mean Velocity in Mountain Rivers." *Journal of Hydraulic Engineering* 111 (4): 612-624.

Vanoni, V A. 1966. "Sediment transportation mechanics: Initiation of motion: Am. Soc. Civil Engineers Proc." *Hydraulics Division* 92 (HY2): 291-313.

Vanoni, V A, ed. 1975. *Sedimentation Engineering.* American Society of Civil Engineers.

Wheaton, J M, and G B Pasternack. 2004. "Use of habitat heterogeneity in salmonid spawning habitat rehabilitation design." *Fifth International Symposium on Ecohydraulics, Aquatic Habitats: Analysis & Restoration.* Madrid. 1-4.